Qubit Measurement and Coupling Strategies and their Applications

Dissertation

zur Erlangung des Grades

des Doktors der Naturwissenschaften

der Naturwissenschaftlich - Technischen Fakultät

der Universität des Saarlandes

von

Marius Schöndorf

Saarbrücken

2020

"Not only is the universe stranger than we think, it is stranger than we can think."

Werner Heisenberg

Abstract

A quantum computer can reduce the amount of computational effort for selected applications exponentially by taking advantage of quantum mechanical phenomena of nature. For the realization of a real-world quantum computer, among other things, optimized qubit measurements and qubit coupling schemes are indispensable. This dissertation uses theoretical tools to develop novel measurement and coupling strategies in different superconducting qubit architectures. In a first part of the thesis a protocol for multi-qubit parity measurements of Transmon qubit registers is presented, which takes advantage of the nonlinear energy level structure to strongly increase contrast, while at the same time achieving high fidelities and being quantum non-demolishing. The second part focuses on superconducting flux qubits, which are promising for adiabatic quantum computing. First a novel indirect flux qubit measurement protocol is introduced, which provides the ability to measure in a fixed basis, the persistent current basis, independent of the qubit energy eigenbasis. Second it is shown that the limitation of natural interactions to pairwise interactions can be overcome by using a nonlinear coupler and four flux qubits. The achieved four local interactions between the qubits are proven to be in the strong coupling regime and even exceed the two local ones for the right system parameters.

Zusammenfassung

Ein Quantencomputer besitzt das Potenzial den Rechenaufwand für bestimmte Aufgaben gegenüber einem klassischen Computer exponentiell zu reduzieren, indem er sich quantenmechanischer Phänomene der Natur bedient. Zur Realisierung eines echten Quantencomputers sind, neben anderen Bestandteilen, optimierte Mess- und Kopplungsschemata für Qubits unabdingbar. Diese Dissertation befasst sich damit theoretische Mittel zu nutzen, um neue Mess- und Kopplunsstrategien in verschiedenen supraleitenden Qubitarchitekturen zu entwickeln. In einem ersten Teil der Arbeit wird ein neues Protokol zur Paritätsmessung von Registern aus Transmon Qubits vorgestellt, welches die nichtlineare Energiestruktur ausnutzt, um den Kontrast der Messung stark zu erhöhen und zudem sowohl einen hohen Kontrast aufweist und QND ist. Der zweite Teil fokussiert sich auf supraleitende Flussqubits, die vor allem beim adiabatischen Quantencomputer genutzt werden. Zuerst wird ein neues, indirektes Messprotokol vorgestellt, welches die Möglichkeit bietet in einer festen Basis, der Dauerstrombasis, unabhängig von der jeweiligen Energieeigenbasis, zu messen. Danach wird gezeigt, dass die Einschränkung von natürlichen Wechselwirkungen auf paarweise Wechselwirkung überwunden werden kann, indem man vier Flussqubits mittels eines nichtlinearen Kopplers verknüpft. Die erreichten Viererwechselwirkungen zwischen den Qubits sind im Regime starker Kopplung und können für die richtigen Systemparameter die paarweisen Wechselwirkungen überschreiten.

Publication List

Published

- M. Schöndorf and F. K. Wilhelm
  Nonlinear Parity Readout with a Microwave Photodetector
  Phys Rev. A **97**, 043849 (2018)

- M. Schöndorf and F. K. Wilhelm
  Nonpairwise Interactions Induced by Virtual Transitions in Four Coupled Artificial Atoms
  Phys Rev. Applied **12**, 064026 (2019)

- M. Schöndorf, A. Lupaşcu and F. K. Wilhelm
  Flux-qubit readout in the persistent-current basis at arbitrary bias points
  Phys Rev. A **101**, 012305 (2020)

Previous Publications

- M. Schöndorf, L. C. G. Govia, M. Vavilov, R. McDermott and F. K. Wilhelm
  Optimizing microwave photodetection: Input-Output theory
  Quantum Science and Technology (2018)

Acknowledgements

First and foremost I would like to thank Frank Wilhelm-Mauch who has given me the opportunity to join his research group. He has always scientifically supported me during the research for this thesis and has given me the opportunity to work in collaboration with the other leading researchers in the field. For me, he is the example of an outstanding researcher and I am very grateful to be able to learn from him during the last years.

I would also like to thank all group members I worked with during the process of this thesis, especially Luke Govia who has been the perfect supervisor during my starting time. Also I would like to thank Adrian Lupascu who gave me the opportunity to work with him and understand the experimental aspects of the field. I am also grateful to Michael Kaicher and Simon Jäger who made studies much more enjoyable. Additionally

I would like to thank all my family and friends, it would not have been possible to achieve the completion of this thesis without your love and support.

Finally I thank all people who contributed to this thesis in some way and who supported me throughout the writing of this thesis, including Peter Schuhmacher, Raphael Schmit and Michael Kaicher who helped with proofreading.

Contents

xiv

List of Figures

To my parents

Chapter I

Introduction

In this part of the thesis we give a brief introduction into the theoretical backround needed to understand the other two parts, where we present our own results. After a short historical review of modern computation, we deliver the mathematical language used in the field of quantum computation and list the necessary ingredients for a universal quantum machine. Additionally it is shown how to realize quantum bits in superconducting circuits. In the last section we briefly introduce the field of open quantum system, which is used throughout the thesis to describe measurements of quantum systems as well as environmental effects.

1 History of Modern Computers

The aim to use physical constructions to solve computational problems started long before the first realization of what we would now call a classical computer. One of the first known mechanical tools which helped people to perform mathematical calculus was the so called abacus, invented around 2500 B.C. Being far away from solving complex problems like modern computers, the abacus is still used for basic calculations, especially in Asia. The abacus may be viewed as the trigger that caused an avalanche of inventions that finally resulted in modern classical computers.

Alan Turing started the journey of modern computing and the field of computer science in 1936 with his remarkable paper, in which he first presented an abstract version of a programmable computer, now called Turing machine [1]. Here he introduced the idea of universality and showed that any algorithm performed on some deterministic device can also be performed on the universal Turing machine.

Motivated by Turing's theoretical work, many scientists tried to build the optimal mechanical device which realizes such a universal Turing machine. In 1941 Konrad Zuse presented the Z3, which was the first functional, fully automatic, programmable device using binary floating point numbers, hence the first modern computer.

Besides Zuse's invention, there were a lot of other more or less successful efforts to build a universal Turing machine. However, in most cases the biggest downside of these devices was scalability. The physical constructions were huge and additionally often extremely vulnerable to errors. This all changed with the development of the transistor in 1947, which delivered a scalable and error-robust physical device to build universal binary computers. The further development of integrated circuits since then is a main research and engineering field, even honored with a Nobel price for Jack S. Kilby in 2010 [2]. As predicted by Moore in the 60s, the computer power doubles every year, a circumstance referred to as Moore's law [3]. However, Moore's law starts to saturate [4], mostly because quantum mechanical effects start to matter when scaling down more and more.

The breakdown of Moore's law shows that the computational power of modern computers will be limited, which motivated people to think about alternative ways to perform computation in a more effective way. In 1981 Richard Feynman was the first to noticed that it would make a lot more sense to use a machine which satisfies the laws of quantum mechanics to simulate quantum systems [5]. This was the birth of the field of quantum computing. Since quantum mechanical effects seem to limit Moore's law, a logical next step was to engineer quantum systems to be able to perform computations on an atomic scale.

2 Quantum Computing

2.1 General Concepts

As mentioned in the previous section, there is a need of inventing new technology to build more powerful computers including the laws of quantum mechanics. In this section the basic concepts of a quantum computer are explained and additionally it is shown how to build a Turing like machine, which is able to perform universal computing.

2.1.1   Qubits

In a classical computer every operation is performed in binary representation. The smallest piece of information which can be stored and processed here is a bit. A bit can adopt two values either "0" or "1". To build a quantum computer, first we need an analogous quantum version of the bit, which is called the "quantum bit" or short, "qubit". A qubit is quantum system, in which two distinguishable states can be isolated. To make a connection to classical computing these two states are usually referred to as $|0\rangle$ and $|1\rangle$. How to actually realize qubits in physical systems will be discussed in more detail in Sec. 2.4.

As mentioned before a classical bit has either the value 0 or 1, whereas in quantum mechanical systems, a state can also be in a linear superposition of the two states $|0\rangle$ and $|1\rangle$,

$$|\Psi\rangle = \alpha\,|0\rangle + \beta\,|1\rangle. \tag{1.1}$$

When a projective measurement (see Sec. 2.2.2) in the basis $\{|0\rangle, |1\rangle\}$ is performed, one observes the value 0 with probability $|\alpha|^2$ and the value 1 with probability $|\beta|^2$. Therefore α and β are called the probability amplitudes of the state and naturally $|\alpha|^2 + |\beta|^2 = 1$. After the measurement, the original superposition state is projected onto the logical state which corresponds to the respective measurement outcome. This probabilistic behavior, meaning the possibility to be in superposition states, makes a qubit more powerful than a classical bit. A classical bit can store one value whereas the Hilbert space of a qubit is two dimensional. The dimension of the Hilbert state scales exponentially as we will see in Sec. 2.1.2, such that one needs 2^n classical bits to simulate an n qubit register, highlighting the speedup potential of a quantum computer.

It is possible to rewrite (1.1) as

$$|\Psi\rangle = \mathrm{e}^{\mathrm{i}\gamma}\left(\cos\frac{\Theta}{2}\,|0\rangle + \mathrm{e}^{\mathrm{i}\varphi}\sin\frac{\Theta}{2}\,|1\rangle\right), \tag{1.2}$$

where γ, Θ and φ are real numbers. The global phase γ is insignificant, such that φ and Θ completely determine the qubit state. These two numbers can be interpreted as the polar and azimuthal angle of a vector, hence all qubit states lie on the surface of a unit sphere which is called the Bloch sphere (see Fig. 1.1). It follows that the state Ψ can also be expressed in Cartesian coordinates

$$|\Psi\rangle = \begin{pmatrix} \sin\Theta\cos\varphi \\ \sin\Theta\sin\varphi \\ \cos\Theta \end{pmatrix}.$$

The x, y and z contributions correspond to the expectation value of the respective Pauli spin matrix $\langle\hat{\sigma}_i\rangle = \langle\Psi|\hat{\sigma}_i|\Psi\rangle$, with $i = \{x, y, z\}$.

Every single qubit gate can be interpreted as a unitary rotation of the corresponding Bloch vector.

Another possibility is to represent qubit states in an operator formalism, in form of the so called density matrix. For a pure state $|\Psi\rangle$, meaning a state that is represented by one specific vector in the respective Hilbert space, the density operator is defined as

$$\hat{\rho} = |\Psi\rangle\langle\Psi|. \tag{1.3}$$
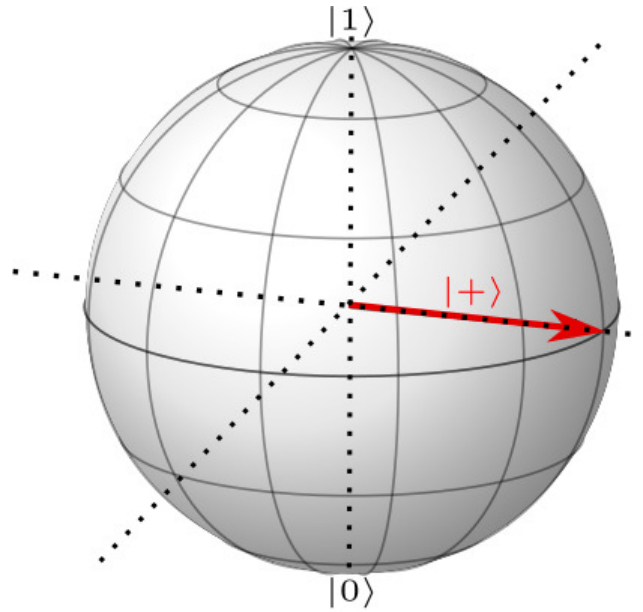
FIGURE 1.1: *Representation of the superposition state* $|+\rangle = 1/\sqrt{2}(|0\rangle + |1\rangle)$. *Since* $|+\rangle$ *is an eigenstate of the Pauli X matrix, it lies on the x-axis of the Bloch sphere.*

If $|\Psi\rangle$ is a single qubit state of the form (1.1), the density matrix has the form

$$\hat{\rho} = \begin{pmatrix} |\alpha|^2 & \alpha\beta^* \\ \alpha^*\beta & |\beta|^2 \end{pmatrix}. \tag{1.4}$$

However, a system is not always in a pure state, it can also exist in a mixed state, i.e. the quantum state itself is only known with some probability. In this case the density matrix is the sum of all the appearing states $|\Psi\rangle$ with corresponding weights p_i

$$\hat{\rho} = \sum_i p_i |\Psi_i\rangle \langle\Psi_i|. \tag{1.5}$$

(1.3) is just a special case of (1.5), where all weights except one are zero. Note that the density matrix can be explicitly time-dependent. The analogue to the Schrödinger equation in terms of density matrices describing the time evolution of the latter is the Liouville-Von Neumann equation

$$\dot{\hat{\rho}}(t) = -\frac{i}{\hbar}[\hat{H}(t), \hat{\rho}(t)], \tag{1.6}$$

where $\hat{H}(t)$ describe the, in general time dependent, Hamiltonian of the system.

2.1.2 Gates and multiple Qubits

As mentioned before, every single qubit gate can be represented by a unitary operator $\hat{U}$ rotating the initial state $|\Psi\rangle$ to the state $|\Psi'\rangle = \hat{U}|\Psi\rangle$ on the Bloch sphere. An example of such a rotation is the NOT gate, which corresponds to the classical version of the NOT gate. On the Bloch sphere this operation can be interpreted as a π rotation around the x-axis. Since we use $|0\rangle$ and $|1\rangle$ as the computational basis, the NOT gate

can be written as the unitary

$$\text{NOT} = \begin{pmatrix} 0 & 1 \\ 1 & 0 \end{pmatrix}, \tag{1.7}$$

where the two basis states $|0\rangle$ and $|1\rangle$ correspond to the canonical basis vectors $\begin{pmatrix} 1 \\ 0 \end{pmatrix}$ and $\begin{pmatrix} 0 \\ 1 \end{pmatrix}$, respectively. Note that in contrast to a classical computer, where the *NOT* operation is the only non trivial single qubit operation, for a qubit there are several non-trivial single qubit gates.

Certainly one does want to perform algorithms on larger systems than just one single qubit. Therefore it is convenient to write a system of n qubits as a qubit register. The corresponding state Hilbert space is the tensor product of the Hilbert spaces of the single qubits $\mathcal{H} = \otimes_{k=1}^{n} \mathcal{H}_k$ with dimension 2^n. E.g. for a two qubit register a natural basis choice is the compound logical basis $\{|00\rangle, |01\rangle, |10\rangle, |11\rangle\}$, where $|ij\rangle = |i\rangle \otimes |j\rangle$ is the tensor product between the respective two single qubit states. We can again connect an amplitude α_{ij} with every computational state,

$$|\Psi\rangle = \alpha_{00} |00\rangle + \alpha_{01} |01\rangle + \alpha_{10} |10\rangle + \alpha_{11} |11\rangle. \tag{1.8}$$

As in the one qubit case, a two qubit state can be written down as a four dimensional vector of the form $|\Psi\rangle = (\alpha_{00}, \alpha_{01}, \alpha_{10}, \alpha_{11})^T$ and two qubit gates as 4×4 unitary matrices.

The most important concept within quantum computing is entanglement. A two qubit state can not always be written in the product form of two single qubit states $|\Psi\rangle = |\Psi_1\rangle \otimes |\Psi_2\rangle$. If the two qubits are able to interact with each other, then they usually do not evolve independently, hence it is not possible to write them as a tensor product of two single qubit states. Multi-qubit gates that create entanglement between at least two states are called entangling gates and states that cannot be written as product states are called entangled states.

To build a quantum Turing machine we have to be able to perform any arbitrary unitary operation on a number of qubits equal to $\log_2$ of the unitary operators dimension. However, it can be shown that every such operation can be divided into single qubit rotations and an entangling 2 qubit gate. A possible choice for such a gate is the CNOT gate which flips the second qubit of the register if and only if the first qubit is in state $|1\rangle$. Assume e.g. the input state $|\Psi\rangle = 1/\sqrt{2}(|0\rangle + |1\rangle) |0\rangle$, which is clearly a product state, i.e. not entangled. Applying a CNOT on $|\Psi\rangle$ results in the output state $|\Psi'\rangle = 1/\sqrt{2}(|00\rangle + |11\rangle)$, which is maximally entangled. There are other choices than the CNOT but the main point here is that we only need to perform single qubit rotations and one specific 2 qubit gate to build a universal quantum computer, hence evade the necessity to implement arbitrary n qubit gates (Solovay-Kitaev theorem [6]). Another crucial point following from the unitarity of qubit operations is that in contrast to a classical computer the quantum version is reversible [6] (e.g. the NAND gate for classical computers is not invertible).

The model presented in this section is called the gate model and as mentioned has the property to be universal. There are other forms of quantum processors like adiabatic quantum computers (more details in Chapter III), which are not that closely related to classical binary computers. To show that these architectures also realize a universal quantum computer one usually tries to map them to the circuit model with reasonable overhead [7]. Therefore the circuit model basically is the definition

of universality in context of quantum computing.

2.1.3   Quantum Algorithms

In the previous sections we gave the main ingredients for building a quantum computer. Basically we need qubits, a universal set of gates and the possibility to read out the state of the qubit register at the end of the computation (for more details see DiVincenzo criteria in Sec. 2.3). However, it is necessary to find actual algorithms that can be run on a quantum computer and in the best case algorithms that are provable to be faster than every existing, or even every possible classical algorithm. The first known example of the latter type is Grover's algorithm, first presented in [8]. Here, the problem is that one has a large book of elements where one is marked and the goal is to find this marked element. In a more practical manner one could think about having a set of possible solutions to a specific problem and wants to find the right one with the minimum number of queries. We will not show how the quantum algorithm works in detail, here we refer the reader to one of the references [9] or [6]. However, it can be shown that Grover's algorithm has complexity $\mathcal{O}(\sqrt{m})$ whereas the best possible classical algorithm scales with $\mathcal{O}(m)$, where m denotes the number of elements. Therefore Grover's algorithm shows a provable quantum speedup. In Sec. 9.2 we present the adiabatic version of the Grover algorithm in some detail.

Another prominent candidate of quantum algorithms is Shor's algorithm. In [10] Shor showed that a quantum algorithm can be used to efficiently perform prime factoring. Since for classical computers this problem scales exponentially with currently known algorithms and Shor's quantum version only polynomially, this yields the first huge quantum speedup ever predicted. Note that here quantum speedup is not proven, since we do not know if the current classical algorithm is the most efficient one possible.

Since these more theoretically motivated quantum algorithms of the 90s were predicted, much more practically motivated suggestions on how to acutally use a real world has been proposed. Grover's and Shor's algorithm would need a huge number of qubits to actually beat a classical computer, whereas modern aspirations of quantum algorithms try to focus on specific, mostly scientific problems which can be solved by a quantum computer with a reasonable number of qubits. One prominent example is the nitrogen fixation which could be solved efficiently on a quantum computer with $\curvearrowright$ 100 logical qubits (several 100 qubit units running in parallel) [11, 12, 13].

2.2   Quantum Measurement

Measurements are an important concept in the field of quantum mechanics. As we have seen, the evolution of a closed quantum system can always be described by a unitary operator. However, to measure the state of a quantum system, an interaction with another system is required. In Sec. 3 we talk about open quantum systems, where theoretical tools are given to study the non-unitary time evolution of the system for such cases. To describe quantum measurements it is more convenient to use classical probability theory.

In the field of quantum computing, measurements are needed to perform actual quantum algorithms. After running an algorithm on a quantum computer one has to be able to extract the information provided, i.e. to read out the system. Despite this obvious application, quantum measurements are also needed for quantum error correction, or to reset the quantum states. For detailed information about the theory of quantum measurements we refer the reader to [14] and [6], here we will only discuss the basic concepts needed for a thorough understanding of the following chapters.

2.2.1   The Measurement Postulate

To simplify calculations and use classical probability theory, the founders of quantum mechanics stated the measurement postulate which describes an arbitrary quantum measurement [14]. Here every measurement is described by a collection of measurement operators $\{\hat{M}_m\}$. These measurement operators are projective and act on the system being measured. The outcomes are represented by the index m. The probability to get the result m is given by [6]

$$p(m) = \langle\Psi|\hat{M}_m^\dagger\hat{M}_m|\Psi\rangle, \tag{1.9}$$

where $|\Psi\rangle$ denotes the state of the system before the measurement. The state after the measurement is given by

$$\frac{M_m\,|\Psi\rangle}{\sqrt{\langle\Psi|\hat{M}_m^\dagger\hat{M}_m|\Psi\rangle}} \tag{1.10}$$

and the measurement operators must fulfill the completeness relation

$$\sum_m \hat{M}_m^\dagger\hat{M}_m = \mathbb{1}. \tag{1.11}$$

As can be seen by (1.10), the map between the pre- and post-measured state is in general not unitary. The measurement postulate therefore gives a simplification of the more complicated process which happens during a measurement. Since the measurement device itself behaves quantum mechanically and there needs to be an interaction between the system to be measured and the readout device, only the dynamics of the compound system can be described by a unitary operator. Often it is extremely difficult or even impossible to include all degrees of freedom needed into the mathematical description, such that the measurement postulate delivers a recipe to calculate the post measurement state without knowing the full dynamics of the measurement process. To study the time evolution of the state during the whole measurement process, one needs the theory of open quantum systems which is discussed in Sec. 3.

2.2.2   Projective Measurements

A special case of the general quantum measurement described in the last section is the so called Von-Neumann projective measurement. Here, the measurement operators introduced in the measurement postulate must additionally be orthogonal projectors

$$\hat{M}_m\hat{M}_{m'} = \delta_{mm'}\hat{M}_m. \tag{1.12}$$

Despite the fact that projective measurements have some nice properties, such as delivering an easy way to calculate expectation values, they are the most frequently appearing measurements in quantum theory. For example, readout in the logical qubit basis with the measurement operators $M_0 = |0\rangle\langle0|$ and $M_1 = |1\rangle\langle1|$ describes a projective measurement.

   Another prominent example which is especially important for the second part of this thesis are parity measurements in the computational basis. For an N qubit register, a parity measurement determines if an even or odd number of qubits are in their excited $|1\rangle$ state. For a two qubit register for example, a possible set of measurement operators for even and odd parity reads $\hat{M}_{\text{odd}} = |01\rangle\langle01| + |10\rangle\langle10|$ and $M_{\text{even}} = |00\rangle\langle00| + |11\rangle\langle11|$. In quantum information parity measurements are

important especially for syndrome readout in error correction codes [15, 16, 17], but can also be used for entanglement generation [18]. In Part II of this thesis we present a protocol to measure the parity of an N qubit register in a circuit QED setup.

2.2.3 Quantum Non-Demolition Measurement

As mentioned in Sec. 2.2.1, a quantum measurement inevitably includes an interaction between the quantum system to be measured and the readout apparatus. Due to this interaction, the state of the measured system gets disturbed, leading to the fact that a successive measurement would yield another result. E.g. if one wants to measure the position of an electron, the measurement itself kicks the electron with an in general unpredictable force that changes the electrons position.

There are strategies to overcome this disturbance for a specific observable. The main idea here is to design the interaction such that the measurement disturbs the canonically conjugated variable but not the measurement observable itself. First investigated for the measurement of gravitational waves [19], these so called quantum non-demolition (QND) measurements are also a of particular interest within the field of quantum information. Since the measured observable itself is not disturbed by the measurement, a successive sequence of measurements will always yield the same result [14]. In a more mathematical language, the measured observable is an integral of motion within the measurement dynamics. A sufficient condition for a QND measurement is met if the Hamiltonian which describes the interaction during the measurement commutes with the system Hamiltonian.

In practice QND measurements are hard to realize, since a measurement result in experiment always includes the interaction with a macroscopic system, which destroys the quantum character of the measured system. To overcome this problem one commonly uses indirect measurement methods. Here, the quantum system interacts with a quantum probe, where only the conjugated variable of the measured observable is influenced by this interaction. The measured system affects the probe, making it possible to keep track of the quantum state in so called pointer states of the probe subsystem. After this interaction the quantum system and the probe get effectively decoupled, before the actual macroscopic measurement of the quantum probe is performed. With these two steps, one is able to extract information about the quantum system of interest, without disturbing the measured observable. A prominent example of such indirect QND measurements in the field of quantum computing are dispersive measurements [20, 21]. Here a cavity realizes the quantum probe and the qubit state is encoded in the phase or the photon number of the cavity field. The following macroscopic readout usually destroys the cavity field but conserves the state of the measured qubit. In Chapter II of of this thesis, we present a highly nonlinear QND parity readout scheme for Transmon qubits and in Chapter III a novel indirect flux qubit measurement which also satisfies the QND criterion.

2.3 DiVincenzo Criteria

In the last sections the different ingredients needed for the realization of a quantum computer were presented. Up to this point, we treated the qubits and gates as completely theoretical constructions and did not talk about actual experimental realizations. In the next section we will shortly introduce one specific platform for qubit realization, but first it makes sense to summarize which conditions an actual experimental setup must satisfy to construct a quantum computer. In his paper "The Physical Implementation of Quantum Computation" [22], David DiVincenzo

presented five criteria in order to successfully implement quantum algorithms on an experimental platform:

1. *A scalable physical system with well characterized qubits*: For the realization of a qubit one needs a physical system with energy levels well separated by an energy gap. These two states must be uniquely addressable, to actually perform single and multiple gates. During the whole quantum algorithm the system should not leak out of the two-level subspace. Furthermore, a well-defined qubit must be one which can be isolate from the rest of the qubit register to perform control and measurement on it. One big experimental challenge is to realize a scalable register where at the same time every single qubit can be well isolated.

2. *The ability to initialize the state of the qubits to a simple fiducial state*: Quantum algorithms start with some initial state, which has to be prepared. A typical choice here is to start with every qubit of the register being in the $|0\rangle$ state. There are different methods to realize qubit initialization. An intuitive way is to choose temperature of the system close to zero and wait until every qubit relaxes to the ground state (annealing). However, since cooling requires waiting for a time on the order of the relaxation time T_1, alternative ways to actively initialize the qubits were presented, e.g. projective measurements.

3. *Long relevant coherence times*: Interaction of the qubit with an environment induces decoherence transferring the quantum state into a classical one. The timescale describing the loss of quantum behavior of the qubit register, i.e. the coherence time, is especially important for quantum computation, since it sets a limit for gate and measurement times. There are two main decoherence mechanisms: relaxation where the qubit decays into its ground state due to the interaction with the environment and dephasing, where interactions with the environment destroy the coherence of superposition states. In most experimental realizations decoherence times are rather small, such that active error correction schemes are necessary to perform algorithms which require large qubit registers and number of gates.

4. *Universal set of gates*: As mentioned in Sec. 1, a Turing machine can perform any classical algorithm, hence it is called universal. For the quantum version of a Turing machine, one also needs to realize a set of gates which is able to perform any possible quantum algorithm, i.e. a universal set of quantum gates. In particular it has been shown that it is sufficient to perform one two-qubit entangling gate and a small number of single qubit gates to meet universality. The experimental challenge here is to perform one and two qubit gates with high fidelities, within the decoherence time of the qubit register.

5. *Qubit specific measurement capability*: At the end of a quantum algorithm, it is necessary to extract the answer out of the system, otherwise the quantum computer would be useless. Therefore one needs to experimentally realize high fidelity measurement schemes to readout the state of the qubit register. Since the measurement must be performed within the coherence time, these measurement schemes also have to be fast compared to the decoherence rates of the system.

2.4 Qubit Realization with Integrated Circuits

Since the field of quantum information was born in the 1980s, a lot of qubit architectures have been proposed [23]. In this thesis we focus on superconducting qubits. For

the physical realization of a qubit one needs a system with two isolated addressable energy levels corresponding to the computational 0 and 1 of the qubit. Many qubit architectures use natural two-level systems e.g. the two different spin states of an electron in an atom. Here the benefit is that the system parameters do not depend on the fabrication process, they are fixed by nature.

Besides from this two-level systems that nature delivers, it is also possible to create artificial two-level systems to use as a qubit. The advantage of these qubits is, that the characteristic frequencies can be determined by the fabrication process, such that they can be chosen in a regime where good control electronics already exist. In natural two-level systems, on the other hand, the energy levels are fixed and one has to adjust control electronics, which can be challenging. Furthermore, these artificial qubits are fixed in space, e.g. they can be built on chip, and the interactions can be designed to fit for specific purposes.

The currently most promising candidate within the family of artificial atoms are the superconducting ones. Here the characteristic frequencies are in the GHz range, such that one can use the well developed field of microwave electronics for manipulation of the qubits. The necessity for superconducting circuits arises from the fact that any loss mechanism would decohere the qubits and induce a transition from a quantum mechanical to a classical system. On the other hand superconductivity is a robust macroscopic quantum phenomenon [24], and as such fits perfectly to the framework of quantum computing.

Here, we present two basic superconducting qubit realizations which are of importance for this thesis. On the one hand the charge qubit, which provides the basis for the Transmon qubit used in Chapter II and on the other hand the flux qubit which is of main interest in Chapter III. For further details see e.g. [25] for a detailed review or [26] for a shorter overview.

2.4.1   Josephson Junction

The simplest choice for a multi-level quantum system in an integrated circuit would be an LC-oscillator, i.e. a superconducting loop interrupted by a capacitance. However, the superconducting LC oscillator leads to the same Hamiltonian as a quantum harmonic oscillator with an equidistant energy structure. Here, it is not possible to address two energy levels separately making it incomplete for quantum computing purposes. To break the equidistant energy splitting, a nonlinear element, the so called Josephson junction, is needed in the circuit.

As shown in Fig. 1.2, the Josephson junction is a non-superconducting layer (usually an insulator) sandwiched by two superconducting layers. The usual choice for superconducting qubits is aluminum with an alumina layer of about 1 nm in between the superconducting layer [27]. If the Josephson junction is cooled down to the superconducting regime (about 15 mK), a tunneling of Cooper pairs across the junction leads to a nonzero current and voltage. Each superconducting layer can be described by a wave function with amplitude $|\Psi_i|$ and phase φ_i. The current induced by the tunneling is given by the first Josephson equation [28]

$$I = I_c \sin \varphi, \tag{1.13}$$

where $\varphi = \varphi_1 - \varphi_2$ denotes the phase difference across the junction. I_c corresponds to the maximum value a biasing current can adopt before superconductivity breaks down, called the critical current. The voltage across the junction is described by the
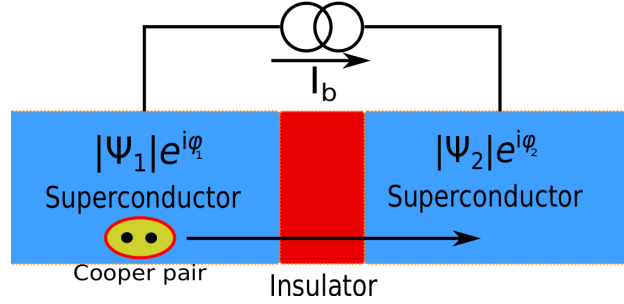
FIGURE 1.2: *A Josephson junction consists of two superconducting layers and an insulating layer in between. For a non-vanishing phase difference $\varphi_1 - \varphi_2$ Cooper pairs can tunnel across the insulating layer, resulting in a supercurrent across the junction.*

quantum Faraday law [28]

$$V = \Phi_0 \dot{\varphi}, \tag{1.14}$$

where $\Phi_0 = \hbar/2e$ is the magnetic flux quantum. Since the two conducting layers with an insulator in between also correspond to a capacitance, the Josephson junction can be represented by a capacitance C_J in parallel with a nonlinear inductance L_J. A microscopic derivation of the Josephson equations can be obtained using BCS theory; we refer the reader to [29] for further details.

2.4.2   The Charge Qubit

The Josephson junction provides the nonlinear ingredient necessary for the realization of superconducting qubits. However, there exist different possibilities to build a superconducting qubit, one of which is the charge qubit [30, 31, 32]. The corresponding circuit is shown in Fig. 1.3. Here the area isolated by the capacitance on the one end and the Josephson junction on the other end is called the superconducting island. In the quantum regime, Cooper pairs can tunnel through the junction onto the isolated island and with this change the corresponding energy. Therefore one can use the number of Cooper pairs on the island $\hat{n}$ as a quantum variable and write the Hamiltonian of the charge qubit as

$$\hat{H} = E_c(\hat{n} - n_g)^2 - E_J \cos \hat{\varphi}, \tag{1.15}$$

with charging energy $E_c = (2e^2)/(C_J + C_g)$, Jospehson energy $E_J = I_c \Phi_0$ and gate charge number $n_g = C_g V_g/(2e)$. The charge qubit is operated in the regime $E_c \gg E_J$ to maximize the anharmonicity. The term $E_c(\hat{n} - n_g)$ leads to anharmonic energy levels, where the two lowest ones can be used as the qubits logical 0 and 1. Since $\hat{\varphi}$ is a conjugated variable to $\hat{n}$, the cosine part of (1.15) induces a tunneling onto and from the island, changing the quantum number $\hat{n}$. Therefore the projection of the full Hamiltonian (1.15) on the two lowest charge states $|0\rangle$ and $|1\rangle$ yields

$$\hat{H}_{\text{CQB}} = -\frac{E_c}{2}(1 - 2n_g)\hat{\sigma}_z - \frac{E_J}{2}\hat{\sigma}_x, \tag{1.16}$$
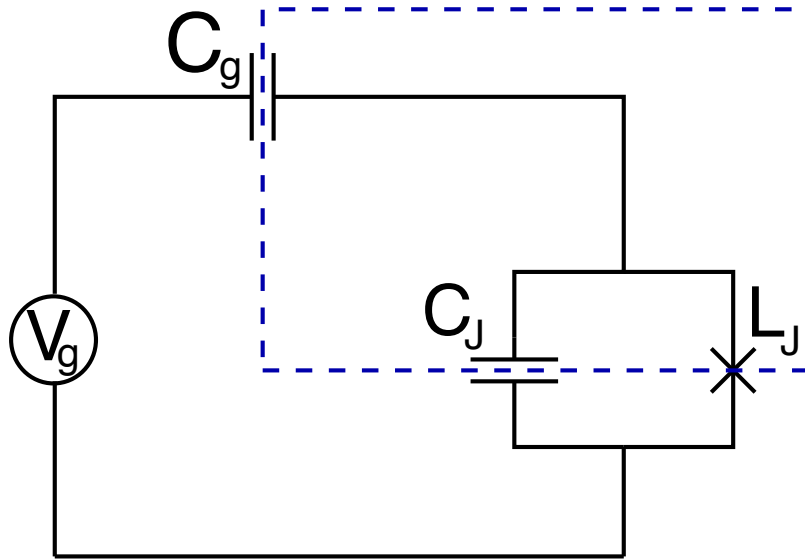
FIGURE 1.3: *Circuit of the charge qubit with gate voltage V_g, gate capacitance C_g, junction capacitance C_J and inductance L_J. The superconducting island is visualized by the blue (dotted) box.*

with the two corresponding eigenenergies

$$E_{0/1} = \mp \frac{1}{2} \sqrt{E_c^2 (1 - 2n_g)^2 + E_J^2} \tag{1.17}$$

and Pauli operators $\hat{\sigma}_z = -|0\rangle\langle 0| + |1\rangle\langle 1|$, $\hat{\sigma}_x = |0\rangle\langle 1| + |1\rangle\langle 0|$. The energy difference of the two states is controlled by the gate voltage. To reduce noise sensitivity of the charge qubit, it is usually operated at the degeneracy point $n_g = 1/2$, where the Hamiltonian is left with the $\hat{\sigma}_x$ contribution. However, charge noise in the material acting on the gate voltage has a crucial effect even slightly away from the degeneracy point, such that modern realizations operate in the regime $E_J \gg E_c$. This is realized by adding an additional shunt capacitance. In this regime the qubit is much more robust against noise sources, but on the other hand it comes at the price of low anharmonicites, making leakage to higher energy levels a serious issue [33]. This version of the charge qubit is called Transmon [33] and appears in Part II of this thesis.

2.4.3   The Flux Qubit

The flux qubit or persistent current qubit (three junction version) is a superconducting qubit using the flux degree of freedom. The easiest design of a flux qubit is the rf-SQUID, which consists of a simple superconducting loop interrupted by a Josephson junction. Due to coherence properties it is more common to use a three junction SQUID in real experiments (see Fig. 1.4). Fluxoid quantization tells us that the flux enclosed in a superconducting loop is restricted to specific values. A loop interrupted by Josephson junctions hence satisfies the relation

$$\sum_i \varphi_i + \frac{2\pi \Phi_{\text{tot}}}{\Phi_0} = 0, \tag{1.18}$$
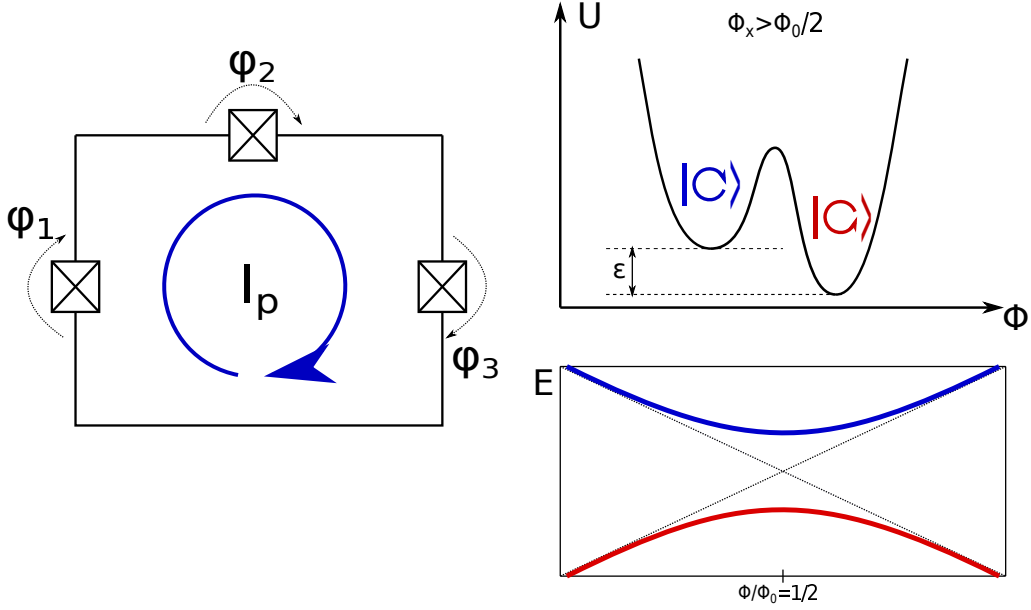
FIGURE 1.4: *Left: Circuit diagram of the commonly used three junction persistent current qubit. Upper Right: Double well potential of the flux qubit with the two wells corresponding to two different persistent current states. Lower right: Avoided crossing of the flux qubit energy spectrum, with degeneracy point at $\Phi_x = \Phi_0/2$*

with Φ_{tot} being the total flux enclosed by the loop and φ_i the flux difference across the i-th Josephson junction. If we assume one junction and apply an external flux Φ_x, the total magnetic flux is given by

$$\Phi_{\text{tot}} = \Phi_x - LI, \tag{1.19}$$

where L is the self-inductance and I the current through the loop. With the fluxoid quantization relation (1.18) and (1.19), the quantized Hamiltonian of the flux qubit can be written as

$$\hat{H} = \frac{\hat{Q}_c^2}{2C} + \frac{(\hat{\Phi} - \Phi_x)^2}{2L} - \beta \cos\left(\frac{2\pi\hat{\Phi}}{\Phi_0}\right), \tag{1.20}$$

with junction capacitance C and $\hat{Q}$ being the canonical conjugate to the quantized flux across the junction $\hat{\Phi}$, such that $[\hat{\Phi}, \hat{Q}] = i\hbar$. The nonlinearity of the flux qubit depends on the ratio of the Josephson energy E_J and the inductive energy $E_L = (\Phi_0/2\pi)^2/L$, i.e $\beta = E_J/E_L$. It is common to use the phase $\hat{\varphi} = 2\pi\hat{\Phi}/\Phi_0$ and Cooper pair number $\hat{q} = \hat{Q}/(2e)$ as dimensionless, conjugated quantum variables instead. Choosing the external flux as

$$\frac{\Phi_x}{\Phi_0} = \frac{1}{2} \mod 1, \tag{1.21}$$

the potential has the form of a symmetric double well. The two wells correspond to two different directions (clock- and counterclockwise) of the persistent current I_p, which is induced to fulfill the fluxoid quantization condition (1.18). At the degeneracy point

(1.21) the frustration between the two supercurrent directions is maximized. The cosine part of the Hamiltonian induces a tunneling between these two persistent current states. For an arbitrary bias point, the two-level approximation of the Hamiltonian (1.20) in the persistent current basis reads:

$$\hat{H} = -\frac{\epsilon}{2}\hat{\sigma}_z - \frac{\Delta}{2}\hat{\sigma}_x, \tag{1.22}$$

with energy asymmetry $\epsilon = I_p(\Phi_x - \Phi_0/2)$ between the two wells and tunnel matrix element Δ. The corresponding eigenvalues are given by

$$E_{0/1} = \pm\frac{\sqrt{\epsilon^2 + \Delta^2}}{2}, \tag{1.23}$$

resulting in a level anticrossing, as shown in Fig. 1.4. Flux qubits are usually operated at the degeneracy point, where they are to first order resistant against flux noise. On the other hand, high fidelity and fast QND readouts at this point is quite challenging, which is the main motivation for the novel measurement protocol presented Sec. 10 of this thesis.

The persistent current qubit was first proposed in [34] and up to now several quantum effects have been observed in these architectures [35, 36, 37]. Modern circuit model implementations usually use charge based qubits due to their better coherence times. However, especially for the realization of a real world adiabatic quantum computer, which will be studied in Chapter III of this thesis, flux qubits are the common choice. One takes advantage of their intrinsic coupling properties as well as their large nonlinearities. The best flux qubits which have been shown to be suitable for quantum annealing are currently produced by the researchers of the quantum enhanced optimization (QEO) program ($T_1 = 3.5\ \mu$s and $T_2^* = 0.13\ \mu$s) [38].

2.4.4 Circuit Quantum Electrodynamics

As shown in the first part of this section, artificial two-level systems serving as qubits can be created using superconducting circuits. However, to build an actual quantum computer one needs to couple, readout and control the respective qubits. Natural atomic two-level systems have characteristic frequencies in the optical range, hence optical cavities are used for this purpose. The study of interactions between light confined in a cavity and atoms is called cavity quantum electrodynamics (cQED) [39, 40]. In contrast, superconducting qubits work in the microwave regime, making it necessary to exchange optical cavities by coplanar waveguide resonators. Being quasi one-dimensional, these waveguides deliver an advantage over optical cavities due to their small mode volume leading to extremely high coupling strengths. The coupling can be achieved in various ways, by inductive or capacitive coupling with the qubit being outside the resonator, or by using electrostatic or galvanic coupling when placing the qubit inside the cavity. This field is called circuit QED [20, 41] and a lot of experimental realizations including coherent Rabi interactions, strong/ultrastrong coupling, readout and control has been presented in the last years [42, 43, 44, 45, 46, 47, 48].

To describe these usually classical microwave devices in a quantum mechanical language, one moves to a second quantized representation. This can be done using standard techniques which can be found in [49]. We refer the reader to this reference and will not review the quantization of a microwave resonator here. After quantization, one realizes that the microwave field in a resonator can be described analog to the optical case, resulting in harmonic oscillator modes. Therefore, the interaction

with a superconducting qubit is in first order given by Rabi dynamics

$$\hat{H}_{\text{int}} = g\hat{\sigma}_x \left(\hat{a}^\dagger + \hat{a} \right), \tag{1.24}$$

with Pauli matrix $\hat{\sigma}_x$ and bosonic field creation and annihilation operators $\hat{a}$ and $\hat{a}^\dagger$. The coupling strength g depends on the specific coupling implementation (for an example see e.g. [50]). Even though in circuit QED experiments ultrastrong couplings have been realized [42], in most cases the coupling strength is small enough to neglect non-secular terms and perform the rotating wave approximation, leading to the simplified Jaynes-Cummings Hamilton

$$\hat{H}_{\text{JC}} \approx g \left(\hat{\sigma}^\dagger \hat{a} + \hat{\sigma} \hat{a}^\dagger \right), \tag{1.25}$$

with $\hat{\sigma}^\dagger$ and $\hat{\sigma}$ being the raising and lowering operator of the qubit. The nonsecular terms are the fast oscillating ones appearing in (1.24). E.g if ω_c denotes the frequency of the cavity and ω_{QB} the qubit frequency, the nonsecular terms are proportional to $\mathrm{e}^{\pm i(\omega_{\text{QB}}+\omega_c)}$. For couplings $g \ll \omega_{\text{QB}} + \omega_c$ these terms average to zero and can be dropped (for more details see [51])

   As mentioned in the beginning of this section, waveguides are also used for qubit readout. Since the second part of this thesis presents an improved version of the usually used linear dispersive readout, we will give a brief introduction into the latter. Dispersive readout schemes aim for a QND measurement of the qubit, meaning one wants to suppress Rabi oscillations between the qubit and the resonator. Therefore the frequency of the resonator ω_c and the qubit ω_{QB} are far detuned ($\Delta = \omega_c - \omega_{\text{QB}} \gg g$), such that the qubit dynamics are assumed to be constant, but the qubit induces a frequency shift of the resonator field. For photon numbers beyond a critical value n_{crit} (for more details see e.g. [52]), the Hamiltonian of the qubit-resonator system can be approximated to order as

$$\hat{H}_{\text{disp}} = \left(\omega_c + \chi\hat{\sigma}_z \right) \hat{a}^\dagger \hat{a} - \frac{1}{2}\omega_{\text{QB}}\hat{\sigma}_z, \tag{1.26}$$

where $\chi = g^2/\Delta$ denotes the dispersive coupling strength between qubit and resonator. Eq. (1.26) shows that the cavity incorporates a state dependent frequency shift. This makes it possible to determine the qubit state by monitoring the transmission of the resonator using homodyne or heterodyne detection [20, 53], or a microwave photon counter [21, 54].

2.4.5   Currently available superconducting qubit architectures

In the last years the field of quantum computing made a transition from being a completely fundamental reasearch topic, to raising also the interest of commercial companies like IBM, Google, Microsoft and created various new startup companies like Rigetti Computing. Here, we will give a few numbers of the current superconducting qubit chip of IBM, such that the reader has an insight on the current status of superconducting qubits. The presented chip uses a variation of the Transmon qubit [33], which is based on the charge qubit (see Sec. 2.4.2), as most of the current so-called noisy intermediate scale quantum (NISQ) devices do. The additional shunt capacitance increases the ratio E_J/E_C ratio to approx. 50, making it extremely robust against charge noise. IBM build their 20 qubit universal quantum computing device, the IBM Q One 20-qubit in 2018/2019, achieving the following numbers [55]:

- T_1 (relaxation time) : $\approx 38.2\ \mu$s - 132.9 μs

- T_2 (decoherence time): $\approx 39.2\ \mu$s - 100.8 μs

- single qubit gate error rates: $8.2 \cdot 10^{-4} - 1.9 \cdot 10^{-4}$

- two qubit gate (CNOT) error rates: $285 \cdot 10^{-4} - 97 \cdot 10^{-4}$,

where the readout fidelity has yet to be determined. A detailed evaluation of the superconducting qubit architectures of all the leading groups can be found in [23] or on *Quantum Computing report* [56], including all relevant numbers as far as they are published.

There are also various announcements of the different companies for the near future. On the 2018 APS March meeting in Los Angeles, Google presented a 72-qubit chip (Bristlecone) [57], basically extending the same architecture they already used for their 9 qubit chip [58, 59, 60]. However, they have not published any results yet but gave some numbers in a talk at the Adiabatic Quantum Computing Conference 2018 [61] and APS March meeting 2019 [62, 63], comparing their 5 and 9 qubit devices against IBM Q indicating that their T_1 times are roughly 2-4 times worse but the single and two qubit gate fidelities are 2-10 times better. They expect the Bristlecone chip to have roughly the same numbers than the previous 5 and 9 qubit devices.

Rigetti computing even announced a chip with 128 superconducting qubits, but also didn't share any results so far. Both of these chips would break the magic number of around 50 qubits, where all currently existing supercomputers are assumed to no longer be able to simulate the corresponding qubit chip, making these chips potential candidates to prove quantum supremacy [64]. E.g. IBM presented a method to simulate a universal random circuit with depth 27 on a 2D lattice of 7×7 qubits within the limits of existing classical computers [65]. Note, that all the currently available devices are so called NISQ computers (see [66] for more details), which means that they do not include any error correction. These NISQ devices could be useful for some specific applications, but the scaling of these devices is limited to a number which is estimated somewhere around 100 qubits. To build quantum computers of larger qubit numbers, one must take advantage of error correction schemes like e.g. the surface code [16, 67]. However, until now no active error correction scheme has been experimentally realized on a superconducting qubit architecture, although Google achieved error detection and state preservation of five qubits [59].

2.4.6 Other Realizations

Despite the qubits based on Josephson junctions, there exist various other physical systems in which qubits have been realized, e.g. ion traps, semiconductor platforms, neutral atoms, photonic qubits, molecular approaches etc. Additionally there are theoretical proposals for more abstract qubits such as topological Majorana qubits, where no experimental prove of functionality has been achieved so far. A complete evaluation of the currently existing qubit platforms can be found in a study of the German IT security administration BSI [23]. We refer the reader to this reference for more information, since this thesis only focuses on Josephson qubits.

3 Open Quantum Systems

In Sec. 2.2 it was mentioned that an actual measurement always includes the interaction with an additional system, making the system of interest no longer closed. Such

interactions are not only present during measurements. In realistic models, one needs to include interactions with an environment, since control and measurement results in a quantum system that is no longer closed. To preserve the unitary time evolution in this case, one needs to include the environmental degrees of freedom, hence enlarge the corresponding Hilbert space to that of the system and the environment. In this section we will show how to derive an effective time evolution of the systems density matrix including the interaction with the environment, but without explicitly stating the time evolution of the latter. With this strategy, it is possible to derive an effective equation of motion for the system under the influence of the bath, avoiding the enormous overhead arising from the environmental degrees of freedom. The theory of open quantum systems is a distinct research area on its own and we can only touch the surface here to give the reader enough basics to understand the rest of this thesis. For a detailed description of open quantum systems, we refer the reader to the excellent reference [68].

3.1   General Equations of Motion

An open quantum system is described by a composition of the actual system S and the environment B, with which it interacts. The combined system S+B is again a closed system, such that its time evolution can be described by a unitary time operator. The dynamics of the system S change due to its inner dynamics and the interaction with B. We refer to the dynamics of the subsystem under the influence of the environment as the reduced system dynamics and call S the reduced system. To mathematically describe the compound system, the Hilbert space of the system is denoted by $\mathcal{H}_S$ and that of the environment with $\mathcal{H}_B$. The Hilbert space of the closed system (including S and B), is then given by the tensor product of these two Hilbert spaces $\mathcal{H} = \mathcal{H}_S \otimes \mathcal{H}_B$, and the Hamiltonian reads

$$\hat{H} = \hat{H}_S \otimes \mathbb{1}_B + \mathbb{1}_S \otimes \hat{H}_B + \hat{H}_{\text{int}}(t). \tag{1.27}$$

Here $\hat{H}_S$ is the self-Hamiltonian of the system, $\hat{H}_B$ the self Hamiltonian of the environment, $\hat{H}_{\text{int}}$ describes the in general time-dependent interaction between the system and the environment, and $\mathbb{1}_{S/B}$ denotes the identity on the system and bath, respectively. In principle, it is possible to write down an evolution operater of the compound system, using Hamiltonian (1.27). However, in most cases the combined dynamics are much to complicated e.g. due to infinite environmental degrees of freedom, such that it is beneficial to develop a simple way to calculate the reduced system dynamics under the influence of the environment, without caring for the actual time evolution of the environment. To do so, we write down the reduced system density matrix by tracing out the environmental degrees of freedom

$$\hat{\rho}_S(t) = \text{tr}_B\{\hat{\rho}(t)\}. \tag{1.28}$$

The expectation value of an arbitrary (in general explicitly time dependent) system operator is then given by

$$\left\langle \hat{A}(t) \right\rangle = \text{tr}_S\{\hat{A}(t)\rho_S(t)\}. \tag{1.29}$$

Using the unitary properties of the compound system the formal time evolution of the full density matrix reads

$$\hat{\rho}(t) = \hat{U}(t,t_0)\rho\hat{U}^\dagger(t,t_0), \tag{1.30}$$

where $\hat{U}(t, t_0)$ is the time propagater resulting from the full Hamiltonian (1.27). To get the time evolution of the reduced system one needs to again trace out the environmental degrees of freedom

$$\rho_S(t) = \text{tr}_B\left\{\hat{U}(t, t_0)\hat{\rho}\hat{U}^\dagger(t, t_0)\right\}. \tag{1.31}$$

Eq. (1.31) leads to a general version of the Liouville-Von Neumann equation for open quantum systems

$$\dot{\hat{\rho}}_S(t) = -\frac{i}{\hbar}\text{tr}_B\left\{\left[\hat{H}(t), \hat{\rho}(t)\right]\right\}. \tag{1.32}$$

In most cases it is extremely hard or even not possible to integrate Eq. (1.32) and obtain the exact time evolution of the reduced system. Therefore we will now show how to derive an effective master equation which simplifies the exact equation significantly by using various approximations. There are other types of open system equations, where the specific choice depends on the conditions required for the respective approximations included. However, in this thesis we only use the Lindblad master equation. For the other important ones we refer the reader to Ref. [68].

3.2 The Lindblad Master Equation

Equation (1.32) can be expressed as a master equation. As a starting point, we assume that the initial state is prepared as a product state between the system and the environment $\hat{\rho} = \hat{\rho}_S(0) \otimes \hat{\rho}_B$. The time evolution from the initial state to some time t can then be described by a map $V(t)$ acting on the space of density matrices of the reduced system $V(t) : S(\mathcal{H}_S) \mapsto S(\mathcal{H}_S)$, such that

$$\hat{\rho}_S(t) = V(t)\hat{\rho}_S(0) = \text{tr}_B\left\{\hat{U}(t, t_0)[\hat{\rho}_S(0) \otimes \hat{\rho}_B]\hat{U}^\dagger(t, t_0)\right\}. \tag{1.33}$$

The map $V(t)$ can be shown to be convex-linear, completely positive and trace preserving, which ensures that it maps valid quantum states to valid quantum states. $V(t)$ describes the time evolution of the reduced system over time t and is called a dynamical map. Since in general t is not fixed, the evolution of the open system is described by a family of dynamical maps $\{V(t)|t \geq 0\}$. In a lot of realistic systems, correlations between environmental degrees of freedom decay fast compared to the characteristic time scale of the system, such that it is valid to neglect memory effects in the reduced system dynamics

$$V(t_1 + t_2) = V(t_1)V(t_2). \tag{1.34}$$

This is called the Markovian approximation and the detailed mathematical restrictions which must be satisfied can be found in [68]. The dynamical map $V(t)$ can be written with the corresponding generator $\mathcal{L}$ of the semigroup

$$V(t) = \exp(\mathcal{L}t). \tag{1.35}$$

Using this property it is possible to write down the Markovian master equation for the reduced system (with $\hbar$ set to 1)

$$\dot{\hat{\rho}}_S(t) = \mathcal{L}\hat{\rho}_S(t). \tag{1.36}$$

The operator $\mathcal{L}$ is referred to as the Liouville super-operator. The most general form of Eq. (1.36) is called the Lindblad master equation and reads

$$\dot{\hat{\rho}}_S(t) = -i\left[\hat{H}_S, \hat{\rho}(t)\right] + \sum_k \gamma_k \left(\hat{L}_k\rho(t)\hat{L}_k^\dagger - \frac{1}{2}\left\{\hat{L}_k^\dagger\hat{L}_k, \hat{\rho}(t)\right\}\right). \qquad (1.37)$$

The Lindblad operators $\hat{L}_K$ describe the different decay channels implied by the environment and the γ_ks are the corresponding rates of the incoherent processes.

In general it is difficult to derive the Lindblad master equation out of the Hamilton description of the coherent evolution between system and environment. Detailed microscopic derivations of the Lindblad master equation can be found in [68] and we refer the reader to this excellent reference for more details. For the derivation in the weak coupling limit the following assumption, in addition to the mentioned Markov approximation, are made:

- Born approximation: The effect of the dynamics on the state of the environment can be neglected, such that for all times t the condition $\hat{\rho} = \hat{\rho}_S(t) \otimes \hat{\rho}_B$ is satisfied. This approximation is closely related to the Markov approximation, such that in literature the two are often merged into the Born-Markov approximation

- Rotating wave approximation: The nonsecular terms, i.e. the ones oscillating fast and average out for weak couplings (see Sec. 2.4.4) are neglected.

Chapter II

Parity Measurement

Robust high-fidelity parity measurement is an important operation in many applications of quantum computing. In this Chapter we show how in a circuit-QED architecture, one can measure parity in a single shot at very high contrast by taking advantage of the nonlinear behavior of a strongly driven microwave cavity coupled to one or multiple qubits. We work in a nonlinear dispersive regime treated in an exact dispersive transformation. We show that appropriate tuning of experimental parameters leads to very high contrast in the cavity and therefore to a high efficiency parity readout with a microwave photon counter or another amplitude detector. These tuning conditions are based on nonlinearity and hence are more robust than previously described linear tuning schemes.
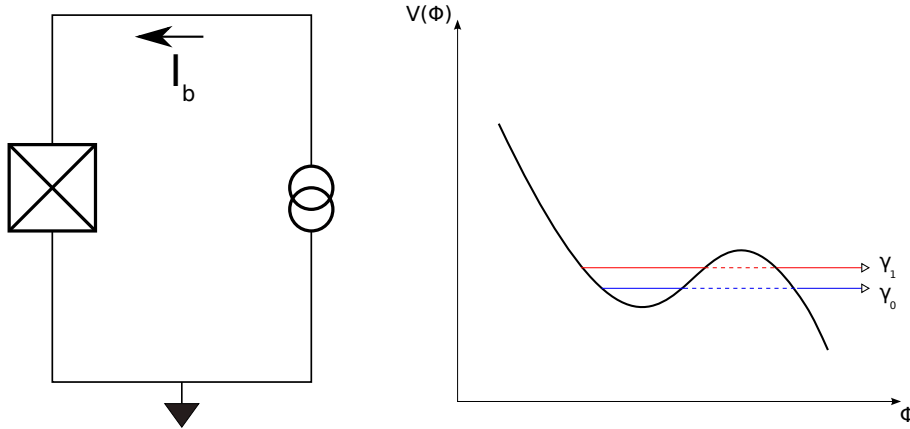
FIGURE 2.1: *Left: Circuit of the JPM; a superconducting loop is interrupted with a small capacitance Josephson junction and an additional bias current is applied. Right: Potential energy of the circuit shown on the left. In every well one finds isolated quasi-bound states.*

7 The Josephson Photomultiplier (JPM)

The parity measurement protocol presented in this chapter is based on an amplitude readout of the cavity at the end of the protocol. This means that in contrast to usual readout schemes of superconducting qubits, where a phase sensitive measurement of the cavity is used to distinguish the qubit states, we use a microwave photodetector. In contrast to optical frequencies, where materials with matching characteristical frequencies exist and can be used to build efficient photodetectors, in the microwave range one has to use artificial atoms. There are different proposals to build such a microwave photodetector. For definiteness we will present one realization, the Josephson Photomultiplier, which is studied theoretically in [21, 54, 69, 70], and has experimentally shown to be sufficient for effective microwave photodetection [71], as well as for the readout of superconducting qubits [72].

The JPM is in principle a current biased Josephson junction and the underlying circuit is shown in Fig. 2.1. Using Kirchhoff's laws, the potential of the JPM can be derived from the cirucit and reads

$$U(\varphi) = I_c \Phi_0 \cos \varphi - I_b \Phi_0 \varphi, \tag{2.1}$$

with bias current I_b. In Fig. 2.1 one sees that the potential energy has the form of a tilted washboard. In every well, one can identify quasi-bound energy levels, where the number of levels depends on the external bias I_b. Since the tails of the potential have finite height, the tunneling rate out of these stable energy levels is not zero. When such a tunneling process happens, the system is in a state with higher energy than the neighbouring local minima. Therefore the system runs down the washboard and rapidly changes the phase φ. This rapid phase change implies a voltage pulse, which can be detected using classical electronics. For the aim of a microwave photodetector the bias point is chosen such that only two metastable levels are placed in one well. Coupling the JPM to an occupied microwave cavity results in Rabi oscillations between the cavity and the two-level system. The tunneling probability is exponentially increased when the JPM gets excited from the ground to the first excited state. If one prepares the JPM in the ground state, the event of

an incoming photon results in an excitation to the first excited state. After this process the system is very likely to tunnel and imply a measurable voltage pulse. Hence a voltage pulse corresponds to a photon-induced transition of the JPM. Since the characteristic frequency of the JPM is in the microwave range, it can be used to detect single microwave photons efficiently. A complete theoretical description of the JPM can be found in Ref. [69].

8   Nonlinear Parity Readout with a Microwave Photodetector

The platform of circuit quantum electrodynamics (cQED) is a promising candidate for realizing quantum computing in a scalable architecture [20, 26, 59, 73, 74, 75, 76]. In this field, superconducting circuits are used to realize qubits. The two lowest levels of the energy spectrum play the role of the two qubit states. Waveguides and microwave cavities allow for control and coupling of superconducting qubits [75, 77]. Another crucial point is readout. For the implementation of quantum error correction [15, 78, 79, 80] as well as the realization of general multi-qubit circuit QED experiments [81, 82, 83, 84], high fidelity multi-qubit state readout is essential.

Currently, readout in superconducting circuits is mostly realized using homodyne field amplitude detection [20, 77, 85, 86, 87]. This scheme requires additional devices such as parametric amplifiers to measure the field amplitudes [86, 88]. While amplifiers are readily available, they require space-consuming microwave peripherals such as circulators [89]. In [21] we presented a scheme to readout the state of a qubit by coupling it dispersively to a driven microwave cavity and measure if the cavity is bright or dark using a microwave photon counter. It is also possible to measure multi-qubit parity states with this setup [54]. A challenge lies in the limited sensitivity of these detectors. Effects like back reflection of incoming photons and wrong rate calibration lead to photon loss in the counter, such that one needs a relatively high number of photons to actually get a count [70]. This can be in conflict with the applicability of the dispersive approximation [52].

A way out to increase contrast at limited sensitivity is to boost the signal and use the nonlinear response of the driven cavity [90], similar to how it has been done in the single qubit case. In [91] Boissenault et al. studied an M-level system dispersively coupled to a microwave cavity. They showed numerically that going to higher drive strengths where $n > n_{\mathrm{crit}}$ leads to a nonlinear behavior of the system dynamics resulting in a huge enhancement of the cavity occupation that can be used to distinguish the two logical qubit states. At the same time Bishop et al. [92] studied the analogous system with just two energy levels included. This amounts to a binary pre-measurement of the qubit state. They used the exact dispersive transformation [93] in a semi-classical regime to describe this phenomenon mathematically. The nonlinear effects were also demonstrated in experiment for readout of a two-level system [92, 94].

Here we study this transition to a nonlinear response of the cavity using the exact dispersive transformation and extend it to multiple qubits coupled to the transmission line while taking into account M energy levels of the system representing the qubit. We show how the exact dispersive transformation is performed for the general case of M energy levels and N qubits and derive an analytical expression for the steady state photon occupation of the cavity depending on the N-qubit state. Analogous to the results of [91] the equations lead to a strong enhancement in the cavity occupation depending on the qubit state. This state dependence can only be seen when we include higher energy levels than the two qubit states, since they lead to asymmetric frequency shifts of the effective cavity frequency.

We furthermore use stability analysis to derive an expression for the critical drive strength at which one can observe the strong enhancement in the cavity occupation.

An important observation is that besides the qubit state, the position of this transition also depends on the detuning of the drive frequency and the bare cavity frequency. We show that with this dependency one can tune the system such that it is possible to perform any arbitrary two qubit measurement in the logical basis, including parity readout. While one drive frequency is enough to perform parity measurements for two qubits, we show that one needs $\lfloor N/2 \rfloor$ different drive frequencies to extend the parity readout scheme to N qubits.

The advantage of the strongly driven regime is the high contrast of about 10^5 photons between the different states, such that even a photon detector with very low efficiency can be used to perform the scheme we present here. While it seems possible to use homodyne detection at first, here the problem is that an arbitrary detuning between drive and cavity frequency is not possible, because the drive is at the same time used for readout, which also causes a phase sensitivity of the readout we do not have when we use a microwave photon counter instead.

Another point which is crucial in this strong driven regime is the backaction of the high cavity occupation on the qubit state. Since we want to perform quantum non demolition measurements (QND) to use the scheme for instance for quantum error correction [6, 95], the post-measurement qubit state should be the corresponding parity eigenstate. We look at the effect of decoherence and relaxation of the qubit in this regime and show that all the appearing rates of the decoherence channels in the new frame (general dispersive frame) are of the order of the incoherent rates in the lab frame. This is important, to show that incoherent processes are not orders of magnitude larger in the frame we work in. Additionally we have to study the effect of photon leakage of the cavity on the decoherence of the qubits.

8.1   Two Qubit Case

8.1.1   System and Hamiltonian

Here we look at two qubits coupled to a strongly, classically driven microwave cavity. Since most of the current experiments use Transmon qubits, which have a weak anharmonicity, we will take into account 3 energy levels instead of only the two lowest qubit states. In Sec. 8.2 where we generalize the whole calculation, we expand this to the case of a general M level system. The cavity is additionally coupled to a microwave photon detector, which is used to distinguish between a bright and dark cavity without detecting the phase [21, 54]. The setup is shown in Fig 2.2, where the photon detection is performed by the JPM [69, 71], but in principle there are no restrictions on the type of photon detector. The bare qubit and cavity Hamiltonian $\hat{H}_0$ is given by

$$\hat{H}_0 = \omega_c \hat{a}^\dagger \hat{a} + \sum_{i=0}^{2} \omega_i^{(1)} \hat{\Pi}_i^{(1)} + \sum_{i=0}^{2} \omega_i^{(2)} \hat{\Pi}_i^{(2)}. \tag{2.2}$$

In this expression $\hat{a}$ and $\hat{a}^\dagger$ denote the bosonic annihilation and creation operator for a cavity mode of frequency ω_c, respectively and $\omega_i^{(j)}$ is the corresponding frequency of the energy level $|i\rangle^{(j)}$, where the upper index stands for the j-th qubit (here $j = 1, 2$). The operators $\hat{\Pi}_i^{(j)} = (|i\rangle \langle i|)^{(j)}$ are the projection operators on the i-th qubit energy level of the j-th qubit. To simplify the calculation we set $\hbar = 1$.
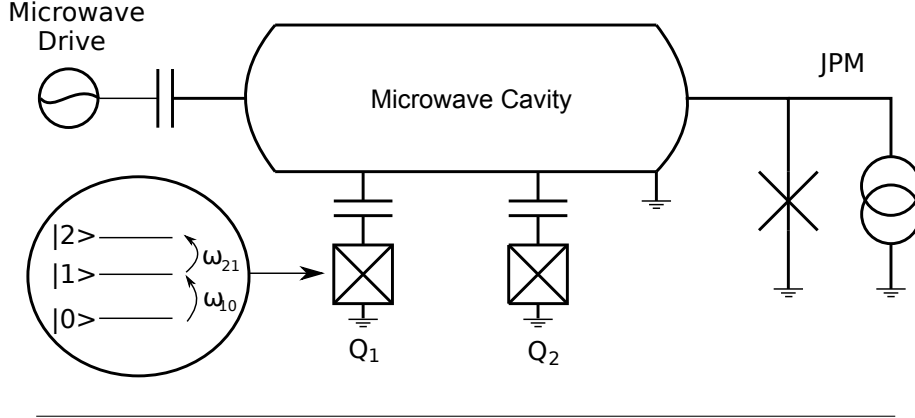
FIGURE 2.2: *System schematic. 2 Qubits are coupled to a driven microwave cavity. The existence of photons in the cavity is read out by a microwave photon counter.*

For later applying the exact dispersive transformation, we want to rewrite the Hamiltonian using the $\hat{\sigma}_z$ operators of the two dimensional subspaces

$$\sigma_{z,i}^{(j)} = -\hat{\Pi}_{i-1}^{(j)} + \hat{\Pi}_i^{(j)}. \tag{2.3}$$

The result is a Hamiltonian that highlights transitions

$$\hat{H}_0 = \omega_c \hat{a}^\dagger \hat{a} + \sum_{i=1}^{2} \tilde{\omega}_i^{(1)} \frac{\hat{\sigma}_{z,i}^{(1)}}{2} + \sum_{i=1}^{2} \tilde{\omega}_i^{(2)} \frac{\hat{\sigma}_{z,i}^{(2)}}{2}, \tag{2.4}$$

where $\tilde{\omega}_i^{(j)}$ are the transformed frequencies

$$\tilde{\omega}_1^{(j)} = \frac{4\omega_{10}^{(j)} + 2\omega_{21}^{(j)}}{3} \tag{2.5}$$

$$\tilde{\omega}_2^{(j)} = \frac{2\omega_{10}^{(j)} + 4\omega_{21}^{(j)}}{3}, \tag{2.6}$$

with $\omega_{ij}^{(k)} = \omega_i^{(k)} - \omega_j^{(k)}$. How to perform this transformation in general is shown in App. 8.A. Note that for two different qubits it is $\tilde{\omega}_i^{(1)} \neq \tilde{\omega}_i^{(2)}$.

The interaction between the cavity and the two qubits in the RWA is given by a Jaynes-Cummings term [96] for every allowed transition

$$\hat{H}_{\text{int}} = \hat{H}_{\text{int,QB1}} + \hat{H}_{\text{int,QB2}} \tag{2.7}$$

$$= \sum_{i=1}^{2} g_i^{(1)} \hat{I}_{+,i}^{(1)} + \sum_{i=1}^{2} g_i^{(2)} \hat{I}_{+,i}^{(2)}, \tag{2.8}$$

with coupling strength $g_i^{(j)}$ of the particular transition, interaction operator

$$\hat{I}_{\pm,i}^{(j)} = \hat{a}^\dagger \hat{\sigma}_i^{(j)} \pm \hat{a}\sigma_i^{\dagger(j)} \tag{2.9}$$

and the creation and annihilation operator of the respective qubit transition

$$\hat{\sigma}_i^{(j)} = (|i - 1\rangle \langle i|)^{(j)} \tag{2.10}$$

$$\hat{\sigma}_i^{\dagger(j)} = (|i\rangle \langle i - 1|)^{(j)}. \tag{2.11}$$

In the case of a Transmon qubit, the coupling matrix elements $g_i^{(j)}$ between the corresponding energy levels only depend on that of the $0 \leftrightarrow 1$ transition [33]

$$g_i^{(j)} = \sqrt{i} g_1^{(j)}. \tag{2.12}$$

To get a full description of the system, we also have to take into account the classical cavity drive which is represented by the Hamiltonian [97]

$$\hat{H}_d = \epsilon \left(\hat{a} \mathrm{e}^{i\omega_d t} + \hat{a}^\dagger \mathrm{e}^{-i\omega_d t} \right), \tag{2.13}$$

with drive strength ϵ and drive frequency ω_d.

Combining all terms we end up with the full Hamiltonian

$$\hat{H} = \underbrace{\hat{H}_0 + \hat{H}_{\mathrm{int}}}_{\equiv \hat{H}_{\mathrm{sys}}} + \hat{H}_d. \tag{2.14}$$

To use the setup shown in Fig. 2.2 for readout we work in the strong dispersive regime. The dispersive regime allows to reach a QND measurement by avoiding Rabi oscillations; the strong-dispersive regime allows to resolve all spectral lines. Additionally we assume the bad cavity regime, such that we get a hierarchy of system parameter constraints, which can be satisfied in most experiments

$$\gamma_1, \gamma_\Phi \ll \kappa \ll \frac{(g_i^{(j)})^2}{\omega_{i,i-1}^{(j)} - \omega_c} \ll g_i^{(j)} \ll \omega_c, \tag{2.15}$$

where κ denotes the cavity decay rate and γ_1, γ_Φ the qubit decay and dephasing rate, respectively. As usual, these incoherent rates need to be smaller than those induced by the measurement in order to faithfully detect the qubit, else it would decay before the qubit is detected.

8.1.2   Exact dispersive transformation

In the low photon number regime $n < n_{\mathrm{crit}}$ with $n_{\mathrm{crit}} = (\omega_{10} - \omega_c)^2 / 4g_1^2$, one can use the linear dispersive approximation to diagonalize (2.14). However, we want to go to regimes where $n \gg n_{\mathrm{crit}}$ and a perturbative approximation in n/n_{crit} fails to converge. Therefore we use a different approach, the exact dispersive transformation, which was introduced in [93] and has been applied in circuit QED multiple times [33, 52, 92].

The exact dispersive transformation for two qubits has the parametric form

$$\hat{D} = \exp\left(-\sum_{i=1}^2 \Lambda_i^{(1)}(\hat{N}_i^{(1)})\hat{I}_{-,i}^{(1)} - \sum_{i=1}^2 \Lambda_i^{(2)}(\hat{N}_i^{(2)})\hat{I}_{-,i}^{(2)} \right), \tag{2.16}$$

where the $\Lambda_i(\hat{N}_i^{(j)})$'s are scalar functions of $\hat{N}_i^{(j)} = \hat{a}^\dagger \hat{a} + \hat{\Pi}_i^{(j)}$. This operator denotes the excitation number of the cavity plus the i-th energy level. Since we are in the strong dispersive regime the $\hat{N}_i^{(j)}$s are approximately good quantum numbers , hence Λ can be seen as a scalar when performing the transformation.

Before we apply the transformation we calculate some important commutators. It is easy to show that

$$\left[\hat{I}_{-,1}^{(j)}, \hat{H}_0\right] = \underbrace{\left(\omega_{10}^{(j)} - \omega_c\right)}_{\Delta_1^{(j)}} \hat{I}_{+,1}^{(j)} \tag{2.17}$$

$$\left[\hat{I}_{-,2}^{(j)}, \hat{H}_0\right] = \underbrace{\left(\omega_{20}^{(j)} - \omega_c\right)}_{\Delta_2^{(j)}} \hat{I}_{+,2}^{(j)}. \tag{2.18}$$

To simplify the notation we introduce the following nested commutator [98]

$$\mathbf{ad}_A(B) \equiv [A, B] \quad \mathbf{ad}_A^n(B) \equiv \mathbf{ad}_A(\mathbf{ad}_A^{n-1}(B)) \tag{2.19}$$

With these commutators, we can apply the transformation on $\hat{H}_{\text{sys}}$, using Baker Campbell Hausdorffs formula

$$\begin{aligned}
\hat{H}_{\text{sys}}^D &= \hat{D}^\dagger \hat{H}_{\text{sys}} \hat{D} \\
&= \hat{H}_0 + \sum_{j=1}^{2} \sum_{k=0}^{\infty} \frac{(k+1)g + \Delta_1^{(j)}\Lambda_1^{(j)}}{(k+1)!} \mathbf{ad}_{\Lambda_i \hat{I}_{-,1}^{(j)}}^k \left(\hat{I}_{+,1}\right) \\
&\quad + \sum_{j=1}^{2} \sum_{k=0}^{\infty} \frac{(k+1)g + \Delta_2^{(j)}\Lambda_2^{(j)}}{(k+1)!} \mathbf{ad}_{\Lambda_i \hat{I}_{-,2}^{(j)}}^k \left(\hat{I}_{+,2}\right).
\end{aligned} \tag{2.20}$$

The functions $\Lambda_i^{(j)}$ will always depend on N_i, so we just write $\Lambda_i^{(j)} \equiv \Lambda_i^{(j)}(N_i)$ in the following. To get expression (2.20) we used some properties and relations of the appearing nested commutators that we prove in Appendix 8.D. A more detailed version of this calculation is shown in Appendix 8.C. Here we disregarded direct two photon transition terms (for instance terms proportional to $\hat{a}^2 \sigma_1^\dagger \sigma_2^\dagger$), since the probabilities for such transitions are much less than the one photon processes due to the weak anharmonicity of the Transmon potential (selection rules). It is possible to calculate a closed form of the appearing commutators which reads

$$\begin{aligned}
\mathbf{ad}_{\Lambda_i \hat{I}_{-,i}^{2k}} \left(\hat{I}_{+,i}\right) &= (-4)^k (\Lambda_i)^{2k} N_i^k \hat{I}_{+,i} \\
\mathbf{ad}_{\Lambda_i \hat{I}_{-,i}^{2k+1}} \left(\hat{I}_{+,i}\right) &= -2(-4)^k (\Lambda_i)^{2k+1} N_i^{k+1} \hat{\sigma}_{z,i}.
\end{aligned} \tag{2.21}$$

We put (2.21) into (2.20) and end up with the following expression for the transformed system Hamiltonian

$$\begin{aligned}
\hat{H}_{\text{sys}}^D = \hat{H}_0 + \sum_{k=1}^{2} \sum_{i=1}^{2} \Big[&f_1^{(j)} \left(\Delta_i^{(j)}, g_i^{(j)}, \Lambda_i^{(j)}, N_i^{(j)}\right) \hat{I}_{+,1} \\
&- 2N_q f_2^{(j)} \left(\Delta_i^{(j)}, g_i^{(j)}, \Lambda_i^{(j)}, N_i^{(j)}\right) \hat{\sigma}_{z,i}^{(j)} \Big],
\end{aligned} \tag{2.22}$$

with

$$f_1 \equiv \frac{\Delta_i \sin\left(2\Lambda_i \sqrt{N_i}\right)}{2\sqrt{N_i}} + g_i \cos\left(2\Lambda_i \sqrt{N_i^{(j)}}\right) \tag{2.23}$$

$$f_2 \equiv \frac{g_i \sin\left(2\Lambda_i \sqrt{N_i}\right)}{2\sqrt{N_i}} + \frac{\Delta_i \left\{1 - \cos\left(2\Lambda_i \sqrt{N_q}\right)\right\}}{4N_i}. \tag{2.24}$$

To obtain a diagonal system Hamiltonian we have to choose $\Lambda_i^{(j)}$ such that the $\hat{I}_{+,i}^{(j)}$ contribution is zero. Setting (2.23) equal to zero we find the following choice:

$$\Lambda_i^{(j)} = -\frac{\arctan\left(\lambda_i^{(j)}\sqrt{N_i^{(j)}}\right)}{2\sqrt{N_i^{(j)}}}. \tag{2.25}$$

with $\lambda_i^{(j)} = g_i^{(j)}/\Delta_i^{(j)}$. Finally we put this expression for $\Lambda_i^{(j)}$ into (2.20) and end up with the diagonal system Hamiltonian

$$\hat{H}_{\text{sys}}^D = \hat{H}_0 - \sum_{j=1}^{2}\sum_{i=1}^{2}\frac{\Delta_i^{(j)}}{2}\left(1 - \sqrt{1 + 4\lambda_i^{(j)2}N_i^{(j)}}\right)\hat{\sigma}_{z,i}^{(j)}, \tag{2.26}$$

This expression is exact up to the non parity conserving terms we ignored in (2.20). At this point we only moved $\hat{H}_{\text{sys}}$ into the dispersive frame, but to describe the whole setup we additionally have to transform the drive Hamiltonian $\hat{H}_d$. Since we are interested in the regime $n \gg n_{\text{crit}}$, the drive Hamiltonian stays in its original form by ignoring terms of the order $n^{-1/2}$ and λ_i^2 [92]

$$\hat{H}_d^D \approx \hat{H}_d. \tag{2.27}$$

For further calculations it is more convenient to work with a time independent Hamiltonian. Since $\hat{H}_d$ still includes a time dependence, we go into the frame rotating with the drive frequency $\hat{U} = \mathrm{e}^{-i\hat{n}\omega_d t}$. In this frame the drive is time independent $\hat{H}_d = \epsilon(\hat{a}^\dagger + \hat{a})$ and the system Hamiltonian just incorporates an additional frequency shift in the bare cavity part

$$\hat{H}_0 = \delta_c\hat{a}^\dagger\hat{a} + \sum_{j=1}^{2}\sum_{i=1}^{2}\tilde{\omega}_i^{(j)}\frac{\hat{\sigma}_{z,i}^{(j)}}{2}. \tag{2.28}$$

with $\delta_c = \omega_c - \omega_d$.

8.1.3 Photon amplitude and instability

The interesting value which is crucial for the usage of the setup in Fig. 2.2 for readout is the cavity occupation, which depends on the corresponding state of the qubit. Since (2.26) is diagonal, it is relatively easy to obtain the steady state solution of the photon amplitude. As mentioned in 8.1.2, we assume that the qubit occupation number is constant during the dynamics of the system, which is satisfied because of the diagonal structure of (2.26) and the strong detuning between cavity and qubit. Therefore the $\hat{\sigma}_{z,i}^{(j)}$s are constant, which simplifies the following calculation significantly.

As a starting point we use the Liouville Von-Neumann equation to obtain an equation of motion for the annihilation operator of the cavity mode. Additionally we include an incoherent channel described by the Lindblad operator $\hat{L}_\kappa = \sqrt{\kappa}\hat{a}$ [97], which represents photon loss in the cavity with rate κ. The adjoint master equation [68] leads to an equation of motion for the field operator $\hat{a}$ in the Heisenberg picture

$$\dot{\hat{a}} = i\left[\hat{H}_{\text{sys}}^D + \hat{H}_d, \hat{a}\right] - \frac{\kappa}{2}\hat{a}. \tag{2.29}$$

Putting in the expressions for $\hat{H}^D_{\text{sys}}$ and $\hat{H}_d$, we get

$$\dot{\hat{a}} = -i \left(\delta_c - \sum_{j=1}^{2} \sum_{i=1}^{2} \frac{g_i^{(j)} \lambda_i^{(j)}}{\sqrt{1 + 4\lambda_i^{(j)2} N_i^{(j)}}} \hat{\sigma}_{z,i}^{(j)} - i\frac{\kappa}{2} \right) \hat{a} - i\epsilon. \qquad (2.30)$$

Conjugation of (2.30) leads to the equation of motion for $\hat{a}^\dagger$. We are interested in the cavity occupation in the post ringup state. Usually the steady state describes the state reached at $t \longrightarrow \infty$, but for t with $\gamma_1 t, \gamma_\Phi t \gg 1$ the qubit state would be completely destroyed. However, for $\kappa t \gg 1$ the system is in a pseudo steady state, where the behavior is well described by the steady state solutions. This is the reason why we work in the bad cavity limit, such that for this time t_{pseudo} we still meet the condition $\gamma_1 t, \gamma_\Phi t \ll 1$.

Setting $\dot{\hat{a}} = \dot{\hat{a}}^\dagger = 0$ and solving both equations for $\hat{a}$ and $\hat{a}^\dagger$ we end up with an expression for the photon occupation in the steady state

$$n = \left\langle \hat{a}^\dagger \hat{a} \right\rangle = \frac{\epsilon^2}{\left[\delta_c - \chi\left(N_q\right) \right]^2 + \frac{\kappa^2}{4}}. \qquad (2.31)$$

with nonlinear cavity frequency shift

$$\chi\left(N_q\right) = \sum_{j=1}^{2} \sum_{j=1}^{2} \frac{g_i^{(j)} \lambda_i^{(j)}}{\sqrt{1 + 4\lambda_i^{(j)2} N_i^{(j)}}} \sigma_{z,i}^{(j)}. \qquad (2.32)$$

Note that the frequency shift itself depends on the qubit state, since it includes $\sigma_{z,i}^{(j)}$ such that the photon amplitude depends on the qubit state as well. Another crucial point is that the N_is include the photon number n in the cavity, such that (2.31) represents a transcendental equation. We can solve the equation iteratively and the results for some specific parameters are shown in Fig. 2.3.

There are three regimes which can be distinguished. For low drive strengths we see a linear response of the cavity up to a critical drive strength ϵ_1 and photon number n_1. This corresponds to the region where the system is described by the linear dispersive approximation. After that the amplitude shows a nonlinear behavior (bistable region) resulting in a strong enhancement of the photon occupation. Going to even higher drive strengths yields another critical point (ϵ_2, n_2), where the response of the cavity returns back to a linear behavior. The specific values of ϵ_1 and ϵ_2 depend heavily on the state of the qubit.

The effective cavity frequency on the other hand starts at a specific value which corresponds to the usual Stark shift and rapidly goes over to the bare cavity frequency in between the region $\epsilon_1 < \epsilon < \epsilon_2$. In the next chapter we will see that this nonlinear behavior results from a bifurcation of the transcendental equation (2.31) [99].

In the limit $n \to 0$, the expression for the frequency shift is

$$\lim_{n \to 0} \chi(N_q) = \sum_{j=1}^{2} \sum_{i=1}^{2} g_i^{(j)} \lambda_i^{(j)} \sigma_{z,i}^{(j)}. \qquad (2.33)$$

If we couple one qubit to the cavity and only take the two qubit states into account, we observe the linear χ-shift: $\chi = \pm g_1^2 / \Delta_1$ (see [20]). Thus even though the whole calculation was performed under the assumption $n \gg n_{\text{crit}}$ we still get the correct expressions for small values of n, such that we can assume that our equations also
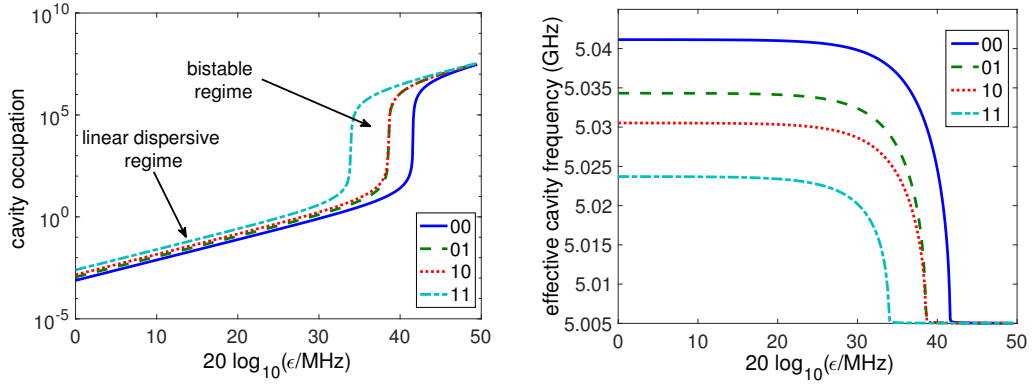
FIGURE 2.3:   *Photon amplitude (top) and effective cavity fre-*
quency (bottom) depending on the drive strength ϵ for the four dif-
ferent qubit states.   The parameters here are $(\omega_{10}, \omega_{21}, g_1)^{(1)}/2\pi =$
$(4.297, 4.071, 0.12)$ GHz, $(\omega_{10}, \omega_{21}, g_1)^{(2)}/2\pi = (4.094, 3.868, 0.12)$
GHz, $\omega_c = 5.005$ GHz and $\delta_c = 0$. For every state exists a specific
drive strength ϵ_{crit}, where the frequency rapidly jumps back to the bare
cavity frequency and one observes a strong enhancement in the cavity
occupation.

give good results in this regime. Another point worth to mention here is that in the
case where only two levels are included the frequency shift is completely symmetric,
such that the response when driving at the bare cavity frequency would be independent
of the state of the qubit. This shows that the pure existence of higher levels influences
the system dynamics, they do not have to be occupied at all.

8.1.4   Stability anlaysis

As mentioned before, the observed strong nonlinear behavior of the photon amplitude
is caused by a bifurcation of (2.31). In between the two linear regimes (see Fig.
2.3) equation (2.31) posses a bistable area with two attractors. Tuning the drive
strength through the first bifurcation point, which appears at ϵ_1, leads to a decision
of the cavity dynamics between the two attractors. Which of both attractors actually
describe the cavity state depends on the history of the system. In principle, small
fluctuations induced by environment-assisted processes can drive transitions between
the two attractors. However, as we see in Fig. 2.3 the difference in amplitude between
these is about 10^6 photons and these environmental fluctuations are assumed to be
rather small. Therefore the system tends to stay in the attractor it chooses when
its driven through the first bifurcation point, i.e. the transition time is exponentially
long.

In this section we want to calculate the two critical points that restrict the bistable
area using stability analysis similar to Drummond et al. [100]. It is difficult to use
the full expression (2.31) for stability analysis since n appears in a square root in the
denominator. As we see in Fig. 2.3 the transition happens around a cavity occupation
of about 10 photons. Therefore it is a good approximation to only keep terms up to
g_i^4/Δ_i^3, since for $n \approx 10$ we still meet the condition $n \cdot g_i^4/\Delta_i^3 \ll 1$. Expanding the
square root appearing in (2.26) up to that order we can derive an equation of motion

for the field amplitudes in the same manner as in the previous section

$$\frac{\partial}{\partial t}\begin{bmatrix} \alpha \\ \alpha^* \end{bmatrix} = \begin{bmatrix} -i\epsilon - \left[\frac{\kappa}{2} + ih(n)\right]\alpha \\ i\epsilon - \left[\frac{\kappa}{2} - ih(n)\right]\alpha^* \end{bmatrix}, \tag{2.34}$$

with $\langle\hat{a}\rangle = \alpha$, $\langle\hat{a}^\dagger\rangle = \alpha^*$ and photon number $n = \alpha^*\alpha$. The function h depends on the photon number n and is given by

$$h(n) = \delta_c + \sum_{j=1}^{2}\sum_{i=1}^{2}\Delta_i^{(j)}\left(\lambda_i^{(j)2} - 2\lambda_i^{(j)4}N_i^{(j)}\right)\sigma_{z,i}^{(j)}. \tag{2.35}$$

With $h(n)$ the steady state condition $\dot{n} = 0$ can be written as

$$|\epsilon|^2 = n\left(\frac{\kappa^2}{4} + h^2(n)\right). \tag{2.36}$$

Now we assume small fluctuations $\Delta\alpha(t)$ around the steady state solution

$$\alpha(t) = \alpha_0 + \Delta\alpha(t) \tag{2.37}$$

and get a linearized equation for the fluctuation

$$\frac{\partial}{\partial t}\begin{bmatrix} \Delta\alpha \\ \Delta\alpha^* \end{bmatrix} = \mathbf{A}\begin{bmatrix} \Delta\alpha \\ \Delta\alpha^* \end{bmatrix}, \tag{2.38}$$

with

$$\mathbf{A} = \begin{bmatrix} i\left(n\frac{\partial h(n)}{\partial n} + h(n)\right) + \frac{\kappa}{2} & i\alpha_0^2\frac{\partial h(n)}{\partial n} \\ -i\alpha_0^{*2}\frac{\partial h(n)}{\partial n} & -i\left(n\frac{\partial h(n)}{\partial n} + h(n)\right) + \frac{\kappa}{2} \end{bmatrix}. \tag{2.39}$$

The stability of equation (2.31) is then controlled by the Hurwitz criteria

$$\mathrm{Tr}(\mathbf{A}) > 0 \tag{2.40}$$

$$\mathrm{Det}(\mathbf{A}) > 0. \tag{2.41}$$

If these two criteria are fulfilled, the eigenvalues of the equation are stable. Therefore the bistability can only occur if one of the two equations (2.41) changes sign. Since $\mathrm{Tr}(A) = \kappa$ and we assume to have a cavity decay ($\kappa > 0$) only the second Hurwitz criterion indicates an instability. The bistable region is restricted by the two critical points that fulfill the condition $\mathrm{Det}(\mathbf{A}) = 0$, which leads to the following expression for the photon number at the critical points:

$$n_{1/2} = \frac{-2\Delta\omega_i \mp \sqrt{\Delta\omega^2 - \frac{3}{4}\kappa^2}}{6\chi}, \tag{2.42}$$

	00	01	10	11
$20\log_{10}(\epsilon_{2,\mathrm{an}}/\mathrm{MHz})$	41.4	38.7	37.6	33.4
$20\log_{10}(\epsilon_{\mathrm{crit,plot}}/\mathrm{MHz})$	41.6	38.6	37.9	33.2

TABLE II.1: Comparison between the analytical value of ϵ_2 calculated with (2.45) and the actual vlaue of ϵ_{crit} in FIG. 2.3. We see an almost perfect agreement.

where we adopted the notation of [100] by defining the parameters

$$\Delta\omega \equiv \delta_c + \sum_{j=1}^{2}\sum_{i=1}^{2}\Delta_i^{(j)}\left(\lambda_i^{(j)2} - 2\lambda_i^{(j)4}N_{\mathrm{QB},i}^{(j)}\right)\sigma_{z,i}^{(j)} \qquad (2.43)$$

$$\chi \equiv -\sum_{j=1}^{2}\sum_{i=1}^{2}2\Delta_i^{(j)}\lambda_i^{(j)4}\sigma_{z,i}^{(j)} \qquad (2.44)$$

with $N_{\mathrm{QB},i}^{(j)} = \left\langle \hat{\Pi}_i^{(j)} \right\rangle$. To get the drive strengths ϵ_1 and ϵ_2 corresponding to the two bifurcation points, we have to put expression (2.42) into the equation for ϵ (2.36)

$$\epsilon_{1/2} = \sqrt{n_{1/2}\left(\frac{\kappa^2}{4} + h^2(n)\right)}. \qquad (2.45)$$

It is obvious that the photon numbers resulting from equation (2.42) has to be positive, such that a bifurcation only occurs if $\Delta\omega^2 > 3\kappa^2/4$ and $\chi\Delta\omega < 0$. The first of these inequalities shows that we do not observe a nonlinear behavior if the leakage rate of the cavity is to high. On the other hand the second inequality leads to the fact that the cavity has to be in the blue detuned regime with respect to the qubit frequencies. The second condition also indicates the borders (dotted vertical lines) in Fig. 2.4. Note that $\Delta\omega$ as well as χ depend on the state of the two qubit subset, such that ϵ_1 and ϵ_2 depend on it as well, which explains the different position of the transition in Fig 2.3.

What we know up to now is that the transition between the two attractors (which we call low and high amplitude attractor in the following) occurs at some value in the bistable area $\epsilon_{\mathrm{crit}} \in (\epsilon_1, \epsilon_2)$. The dynamics of the amplitude depend on the history of the system. Starting at a drive strength smaller than the first bifurcation point ϵ_1 and slowly tune it up to higher drive strengths aims the system to stay in low amplitude attractor until it reaches the second bifurcation point ϵ_2, where this attractor no longer exists and it rapidly jumps into the high amplitude attractor. On the other hand starting at higher drive strengths than the second bifurcation point ϵ_2 leads to a behavior the other way round. The system stays in the high amplitude attractor until it reaches the bifurcation point ϵ_1 and then rapidly "jumps" into the low amplitude attractor, since the high amplitude attractor does not exist for $\epsilon < \epsilon_1$. Therefore the dynamics of the system depend on how the tuning of the parameter ϵ is performed, i.e. the history of the system.

The values for ϵ_2 for the parameters in Fig. 2.3 are given in Tab. II.1. Comparing them to the actual values values of ϵ_{crit} in Fig. 2.3 we see an almost perfect coincidence of ϵ_2 with ϵ_{crit} for all states, which is due to the fact that we started with a small photon number when we solved equation (2.31) iteratively. In a real experiment where one starts with small drive strength and slowly tunes up the drive strength the system tends to stay in the low amplitude solution for every state as long as possible, hence
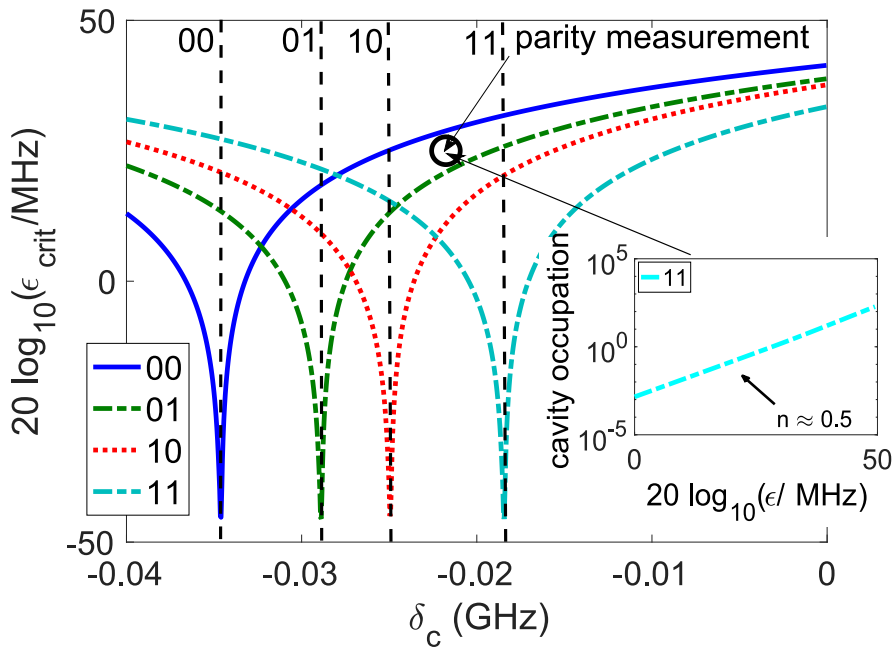
FIGURE 2.4: *Critical point $\epsilon_{\text{crit}} = \epsilon_2$ depending on the cavity drive detuning δ_c for the same parameters as in Fig. 2.3. The dotted vertical lines indicate the value of δ_c, where the condition $\Delta\omega\chi < 0$ is no longer fulfilled such that no bifurcation occurs if we increase δ_c to higher negative values and the system stays in the low amplitude attractor for all drive strengths. For a parity measurement we have to choose δ_c such that we are in the area where the transition to the high amplitude attractor occurs first for $|01\rangle$ and $|10\rangle$ (here $\delta_c \approx -0.02$). In this region $|11\rangle$ does not show a bifurcation and stays in the low amplitude attractor, such that for the corresponding critical drive strength ϵ_{crit} the photon number for $|11\rangle$ is about 0.5 (see inset plot). Additionally we have to drive with $\epsilon_2^{01} < \epsilon < \epsilon_2^{00}$, such that we do not reach the bifurcation point for $|00\rangle$ which assures that we also have a small photon amplitude if the system is in $|00\rangle$.*

the transition in this case can be assumed to be very closed to ϵ_2. Therefore we will assume ϵ_2 to be the actual transition point of the amplitude in the following, since this is the more reasonable method in experiment.

8.1.5 Application to qubit readout and 2 Qubit parity measurement

In the previous sections we assumed that we drive the cavity on resonance $\delta_c = 0$. Therefore it is not possible to detune drive and cavity frequency arbitrarily. Since the bifurcation points are fixed by the qubit parameters in this case, the ordering of the transition depending on the qubit states is also fixed, e.g. ϵ_{crit} for the $|00\rangle$ state will always be larger than the other ones. Because of this, the usage for readout is limited. If we are interested in parity readout, there is no possibility to distinguish even from odd parity states in the case $\delta_c = 0$, since the ϵ_{crit}s of the odd parity states lie in between the ϵ_{crit}s of the even parity states.

Currently readout of superconducting qubits is in most cases performed by homodyne detection schemes [20, 77, 85, 86, 87] where the drive and cavity frequency are in resonance or slightly detuned $\delta_c \approx 0$ [20, 101] (heterodyne detection). Therefore the

detuning between the drive and the cavity frequency is somehow fixed. However, it is also possible to use a microwave photon counter (e.g. the JPM) for readout. Using a microwave photon counter for the readout process of the cavity gives the possibility to arbitrarily detune the drive from the bare cavity frequency $\delta_c \neq 0$. The dependence of the critical drive strength ϵ_{crit} on the detuning δ_c is shown in Fig. 2.4. We see that ϵ_{crit} decreases if we go to higher negative values of δ_c up to a point, where the condition $\Delta\omega\chi < 0$ is no longer satisfied and we no longer have a bifurcation of (2.31), hence the system stays in the low amplitude attractor (linear regime) over the full range of ϵ (see dotted vertical lines in Fig. 2.4).

   To perform two qubit parity measurements with this set up, one has to drive the system with a detuning δ_c in between the point where $|11\rangle$ goes over to a stable behavior and the point where this happens for $|10\rangle$ (circled area in Fig. 2.4). In this region ϵ_{crit} for the odd parity states is smaller than for the $|00\rangle$ state. The $|11\rangle$ state on the other hand stays in the low amplitude solution. Hence the photon number in the cavity if the system is in the $|11\rangle$ state is about 0.5 (see Fig. 2.4) for the corresponding ϵ. All in all with this tuning, the cavity is in a low amplitude state if the qubit is in an even parity state and vice versa.

   When we take a closer look and compare the frequency shifts in Fig. 2.3 and Fig. 2.4, we see that the value of the detuning that gives the border between stable and unstable behavior in Fig. 2.4 for the respective state, matches almost perfectly with the corresponding bare χ-shift (at $\epsilon = 0$). We will see in Sec 8.2 that this behavior can also be observed for more than two qubits. Therefore we can give an analytic expression for the optimal driving point, if one wants to perform parity measurements. A possible physical explanation for this is, that as soon as the drive frequency is higher than the χ-shifted cavity one switches from a red detuned to a blue detuned drive and the drive is no longer forcing the frequencies closer to ω_c. The bare χ-shift is given by (2.33). The optimal driving point lies in between the stability border of $|11\rangle$ and the one of $|10\rangle$ hence is given by:

$$\omega_{d,\mathrm{opt}} = \omega_c + \frac{\chi_{10} + \chi_{11}}{2}, \tag{2.46}$$

where χ_{ij} denotes the bare chi shift if the qubits are in the state $|ij\rangle$. The regime that can be used for parity readout is therefore bounded by (area between two dotted vertical lines 11 and 10 in Fig. 2.4)

$$\omega_c + \chi_{11} < \omega_d < \omega_c + \chi_{10}. \tag{2.47}$$

Choosing a detuning in this regime, which is about 7 MHz broad for the parameters in Fig. 2.4, leads to the right positions of the bifurcation points to perform two qubit parity measurements.

   There is another crucial point one has to take care of when performing the measurement. We have to drive with the right frequency and the right intensity ϵ at the same time. In a real experiment, one would start with a low drive strength and tune the drive strength up into the regime $\epsilon_{\mathrm{crit}}^{01} < \epsilon < \epsilon_{\mathrm{crit}}^{00}$, hold the drive strength in this regime for $\kappa t \gg 1$ and then bring the JPM in resonance with the cavity to read out if the cavity is bright or dark, which corresponds to odd or even parity respectively. If we tune the system in this way we have a photon occupation of about 10^6 photons if the qubits are in an odd parity state and about $1 - 10$ if they are in an even parity state. Note that there can be a small difference in photon number between $|11\rangle$ and $|00\rangle$ but compared to the huge contrast between the odd and even states, this does not significantly influence the measurement. However, to distinguish between

the two parity states we need a photodetector which only clicks if the photon number is above the even parity threshold which can be realized by a lossy photodetector or back reflection in the photon transfer from cavity to detector (see [70]).

By tuning δ_c right one can perform any possible two qubit measurement in the logical basis, so this scheme is not restricted to parity measurement. Performing e.g. projective state measurement just needs to drive the system such that the corresponding ϵ_{crit} is the lowest one. For some of the states we are in the region where the dynamics do not show a bifurcation, but this again is no problem because of the same reason as in the parity measurement scheme; the dynamics stay in the low amplitude attractor, hence the photon number is low for the corresponding ϵ.

Note that in the case of two identical qubits the two odd parity states would show exactly the same behavior, which means $\epsilon_{\mathrm{crit}}^{01} = \epsilon_{\mathrm{crit}}^{10}$. However, in real experiments it is often the case that the qubits have different parameters, since it is hard to produce two completely identical qubits. Therefore we assumed slightly different qubit parameters in Fig 2.4, and we see that if the parameters do not vary too much, parity measurement can still be performed even if the qubits are not completely indistinguishable. For two qubit parity measurements we only need one drive frequency. We will see in Sec 8.2, that this scheme can be expanded to N qubit parity measurements but with a need of $\lfloor N/2 \rfloor$ drive frequencies, where $\lfloor x \rfloor$ denotes the floor function that maps x to the next smaller integer.

8.2 N Qubit case

8.2.1 General formulation and photon amplitude

In this section we expand our result of Sec. 8.1 to N qubits coupled to the readout cavity and we take into account M energy levels. The bare qubit and cavity Hamiltonian $\hat{H}_0$ of this general case has the form

$$\hat{H}_0 = \omega_c \hat{a}^\dagger \hat{a} + \sum_{j=1}^{N} \sum_{i=1}^{M-1} \omega_i^{(j)} \hat{\Pi}_i^{(j)}, \qquad (2.48)$$

where we used the same notation as in the previous section, but the upper limits of the two appearing sums are given by the number of qubits N and the M energy levels taken into account. Again we set $\hbar = 1$ for simplicity. For the two qubit case it was not difficult to rewrite the Hamiltonian using the $\sigma_{z,i}^{(j)}$ operators defined in Eq. (2.3), since we just had to solve an equation system with two variables. Here we need a general transformation rule to get the corresponding Hamiltonian including only $\sigma_{z,i}^{(j)}$ operators in the bare qubit part. How to obtain this transformation is shown in Appendix 8.A. After this transformation we can write the bare Hamiltonian as

$$\hat{H}_0 = \omega_c \hat{a}^\dagger \hat{a} + \sum_{j=1}^{N} \sum_{i=1}^{M-1} \tilde{\omega}_i^{(j)} \frac{\hat{\sigma}_{z,i}^{(j)}}{2}, \qquad (2.49)$$

with the transformation rule

$$\tilde{\omega}_i^{(j)} = \sum_{k=1}^{M-1} A_{i,k}^{-1} \omega_{k,k-1}, \qquad (2.50)$$
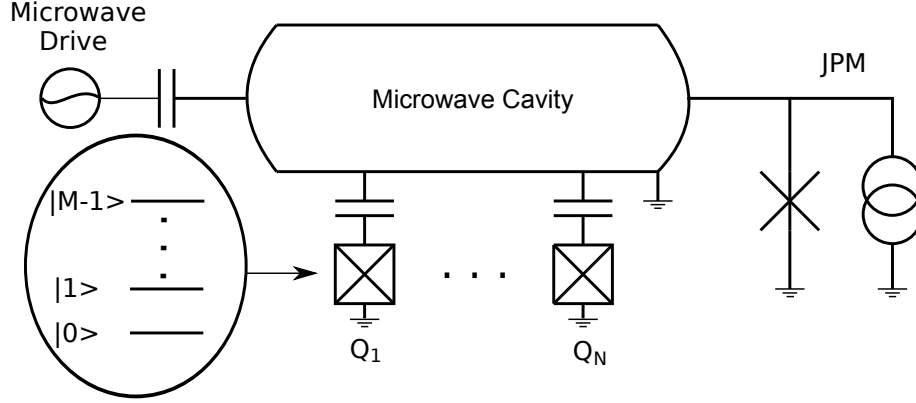
FIGURE 2.5:   *System schematic of the general case.   N Qubits are coupled to a driven microwave cavity.   We take into account M levels.*

where the matrix elements of A^{-1} are given by (see Appendix 8.A)

$$A_{i,k}^{-1} = \begin{cases} -\frac{i(k-M-2)}{M} & 1 \le i \le k \\ -\frac{k(i-M-2)}{M} & k \le i \le M-1. \end{cases} \tag{2.51}$$

The interaction under the RWA leads to a Jaynes-Cummings term for every possible qubit transition summed up over all qubits

$$\hat{H}_{\text{int}} = \sum_{j=1}^{N} \sum_{i=1}^{M-1} g_i^{(j)} \hat{I}_{+,i}^{(j)}, \tag{2.52}$$

where the definition of $\hat{I}_{\pm,i}^{(j)}$ is similar to (2.9). Since we are still assuming Transmon qubits, the coupling matrix elements of the respective qubit depends on the coupling rate of the corresponding $|0\rangle$ to $|1\rangle$ transition in the same manner as before (see Eq. (2.12)).

The drive Hamiltonian $\hat{H}_d$ does not change in the N qubit case and is therefore still (2.13).

The exact dispersive transformation in the general case is given by

$$\hat{D} = \exp\left(\sum_{j=1}^{N} \sum_{i=1}^{M-1} \Lambda_i^{(j)}(\hat{N}_i^{(j)}) \hat{I}_{-,i}^{(j)} \right), \tag{2.53}$$

with $\Lambda_i^{(j)}(\hat{N}_i)$ defined in (2.25). Since $[\hat{\sigma}_{z,i}, \hat{\sigma}_{z,i+1}] \ne 0$, the definition of the $\tilde{\Delta}_i^{(j)}$ is different for higher levels

$$\tilde{\Delta}_i^{(j)} = \begin{cases} \Delta_1^{(j)} - \frac{\tilde{\omega}_2^{(j)}}{2}, & i = 1 \\ \Delta_{M-1}^{(j)} - \frac{\tilde{\omega}_{M-2}^{(j)}}{2}, & i = M-1 \\ \Delta_i^{(j)} - \left(\frac{\tilde{\omega}_{i-1}^{(j)} + \tilde{\omega}_{i+1}^{(j)}}{2} \right), & \text{else.} \end{cases} \tag{2.54}$$

Applying this transformation on the system Hamiltonian is a little more difficult than in the previous section and is done in Appendix 8.B. However, the resulting Hamiltonian has a similar form, except that the appearing sums go to N and $M-1$
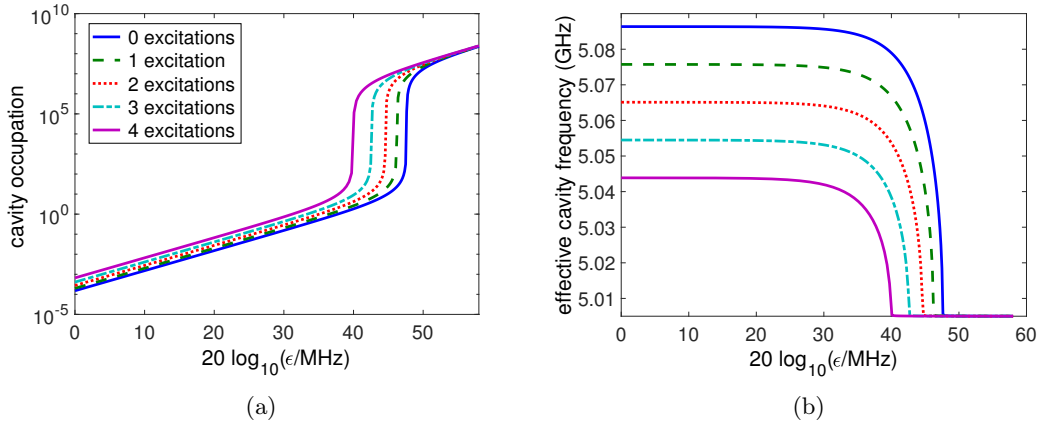
FIGURE 2.6: *Photon amplitude (a) and effective cavity frequency (b) depending on the drive strength ϵ. The plot is for four identical qubits including 10 energy levels. The parameters here are $(\omega_{10}, \omega_{21}, g_1)^{(j)}/2\pi = (4.297, 4.071, 0.12)$ GHz, $\omega_c = 5.005$ GHz and $\delta_c = 0$. For every set of states with the same number of excitations there exists a specific drive strength, where the frequency rapidly jumps back to the bare cavity frequency and one observes a strong enhancement in the cavity occupation.*

respectively

$$\hat{H}_{\mathrm{sys}}^D = \hat{H}_0 - \sum_{j=1}^{N} \sum_{i=1}^{M-1} \frac{\tilde{\Delta}_i^{(j)}}{2} \left(1 - \sqrt{1 + 4\lambda_i^{(j)} N_i^{(j)}} \right) \hat{\sigma}_{z,i}^{(j)}. \qquad (2.55)$$

We again moved to the frame rotating with the drive frequency ω_d, such that δ_c instead of ω_c appears in $\hat{H}_0$. Like before we ignored non parity conserving transitions.

With this Hamiltonian we can again derive equations of motion for the field amplitudes and solve the equation for the photon occupation in the cavity for the steady state resulting in

$$\langle n \rangle = \frac{\epsilon^2}{[\delta_c - \chi\left(N_q\right)]^2 + \frac{\kappa^2}{4}} \qquad (2.56)$$

which is the same expression as in section two (see Eq. (2.31)) but the appearing χ shift has more contributing terms

$$\chi\left(N_q\right) = \sum_{j=1}^{N} \sum_{i=1}^{M-1} \frac{g_i^{(j)} \lambda_i^{(j)}}{\sqrt{1 + 4\lambda_i^{(j)2} N_i^{(j)}}} \sigma_{z,i}^{(j)}. \qquad (2.57)$$

The analogy of the expression we found here and the ones in the previous section indicate that it is very likely that we also observe a nonlinear behavior comparable to the two qubit case. To see that this is indeed the case, we can perform a stability analysis in the same manner as before. Doing so we get the same expression for the photon numbers at the two bifurcation points.

$$n_{1/2} = \frac{-2\Delta\omega \mp \sqrt{\Delta\omega^2 - \frac{3}{4}\kappa^2}}{6\chi}, \qquad (2.58)$$

with the parameters

$$\Delta\omega \equiv \delta_c + \sum_{j=1}^{N}\sum_{i=1}^{M-1} \tilde{\Delta}_i^{(j)}\left(\lambda_i^{(j)2} - 2\lambda_i^{(j)4}N_{\mathrm{QB},i}^{(j)}\right)\sigma_{z,i}^{(j)} \tag{2.59}$$

$$\chi \equiv -\sum_{j=1}^{N}\sum_{i=1}^{M-1} 2\tilde{\Delta}_i^{(j)}\lambda_i^{(j)4}\sigma_{z,i}^{(j)}. \tag{2.60}$$

The conditions that the amplitude shows a instable behavior are the same as for the two qubit case, but with the changed parameters (2.59) and (2.60).

Since we have more qubits and energy levels here, we get a different position for the bifurcation points for every qubit state (assuming that we have slightly different parameters for every single qubit). However, we are only interested in the occupation of the two lowest energy levels of the qubits, since they realize the two mathematical qubit states needed for quantum computation. Again it is the existence of higher levels that influence the whole system, they do not have to be occupied.

The results for the four qubit case is shown in Fig. 2.6. We see that the system behaves the similar to the two qubit case. The photon amplitude shows a huge enhancement at the second bifurcation point ϵ_{crit} (2.45). Analytical expressions for the two bifurcation drive strengths can be obtained by putting the general expression for the bifurcation photon numbers (2.58) into the expression for the drive strength (2.36). In Fig. 2.6 we included 10 energy levels, which is usually more than the number of levels that are relevant in practice [91]. However, we show in App. 8.C that in our case only the next lowest level which is not occupied matters, hence here $M = 3$ yields the correct results.

8.2.2 Multi-qubit parity Measurements

In Sec. 8.1.5 we have shown how to perform two qubit parity measurements in the nonlinear regime using our setup. Now we want to show that the same can be done for N qubits, we just need more than one drive frequency. To perform an N qubit parity measurement we need $\lfloor N/2 \rfloor$ different drive frequencies. In the N qubit case the bifurcation drive strength ϵ_{crit} depends on the detuning between the drive and the bare cavity frequency as well. Therefore we can again take this as an advantage to tune ϵ_{crit} of the different states such that they fit for parity readout.

The values of ϵ_{crit} depending on δ_c are shown in Fig. 2.7, for the case of four identical qubits. Hence only qubits with different excitation number can be distinguished. We see that in the four qubit case in between the borders that restrict the instability condition of $|0001\rangle$ and $|0111\rangle$ lies the border of the even parity state $|0011\rangle$. Therefore it would not be possible to get ϵ_{crit} for the two odd states smaller than for $|0011\rangle$ at the same time, which gives rise to the need of two different drive frequencies. One between the instability borders of $|0111\rangle$ and $|1111\rangle$, which means $\omega_c + \chi_{1111} < \omega_D^{(1)} < \omega_c + \chi_{0111}$ and the other one in between the instability borders of $|0001\rangle$ and $|0011\rangle$: $\omega_c + \chi_{0011} < \omega_D^{(2)} < \omega_c + \chi_{0001}$ as shown in Fig. 2.7. By comparing the frequency shifts in Fig. 2.6 and Fig. 2.7 we again see a coincidence with the instability borders and the bare χ-shifts of the respective states. The optimal drive

frequencies lie in the middle of the respective regime

$$\omega_{D,\text{opt}}^{(1)} = \omega_c - \frac{\chi_{0111} + \chi_{1111}}{2} \tag{2.61}$$

$$\omega_{D,\text{opt}}^{(2)} = \omega_c - \frac{\chi_{0001} + \chi_{0011}}{2}, \tag{2.62}$$

where χ_{ijkl} denotes the bare χ-shift of $|ijkl\rangle$ and can be calculated with (2.57). When we drive the system with these two frequencies, there exists a region of the drive strength

$$\begin{aligned} \max[\epsilon_{\text{crit}}^{0111}(\omega_D^{(1)}), \epsilon_{\text{crit}}^{0111}(\omega_D^{(2)})] &< \epsilon \\ \min[\epsilon_{\text{crit}}^{0001}(\omega_D^{(1)}), \epsilon_{\text{crit}}^{0000}(\omega_D^{(2)})] &> \epsilon \end{aligned} \tag{2.63}$$

where the dynamics of the two odd parity states are described by the high amplitude attractor and the dynamics of the even states by the low amplitude attractor (either since ϵ is smaller then the corresponding ϵ_{crit}, or the state no longer fulfills the condition of instability, which means $\epsilon_{\text{crit}} \to \infty$).

The calibration of the experiment can be performed in the same manner as in the one drive frequency case. First tune the two drives of the system to the right frequencies and then turn up the drive strength into the regime (2.63), hold the drive strengths constant for $t \gg 1/\kappa$ and after that bring the JPM into resonance to read out the state of the cavity.

We can expand this measurement scheme to N qubits. In this case we need $\lfloor N/2 \rfloor$ different drive frequencies. Since we could show that the instability borders and the bare cavity shifts are identical for the two as well as for the four qubit case, we can follow that this also holds for the N qubit case. The respective drive frequencies have to be in between all instability borders of odd and even states (as in the two and four qubit case). Let $\{|\Psi\rangle_i\}$ be the subset of odd parity states and $\{|\Phi\rangle_j\}$ the subset of even parity states of a N qubit system, where i and j denote the number of excitations respectively. With this notation the optimal drive strengths are given by

$$\omega_{D,\text{opt}}^{(i)} = \omega_c - \frac{\chi_{|\Psi\rangle_i} + \chi_{|\Phi\rangle_{i+1}}}{2}, \tag{2.64}$$

where the appearing χ-shifts are again the bare χ-shifts of the corresponding states. Note that in the case of an even number of qubits, it is $i = 1, \ldots, N/2$ and $j = 1, \ldots, N/2 + 1$ and in the case of an odd number of qubits $i = 1, \ldots, (N+1)/2$ and $j = 1, \ldots, (N+1)/2$.

8.3 Is the Measurement Protocol QND?

In this section we want to take a closer look at the QNDness of our measurement protocol. One crucial point here is to calculate the transformed incoherent rates in the new exact dispersive frame and show that they do not increase in a much faster way than the original rates, especially do not scale proportional to the photon number n.

Another important incoherent process is the leakage of photons out of the cavity (key point for the protocol), which leads to dephasing between superpositions of equal parity states corresponding to different frequencies. Again it is to check if this dephasing rate is in the range of the intrinsic incoherent rates of the qubits or if it destroys the QND character of the measurement.
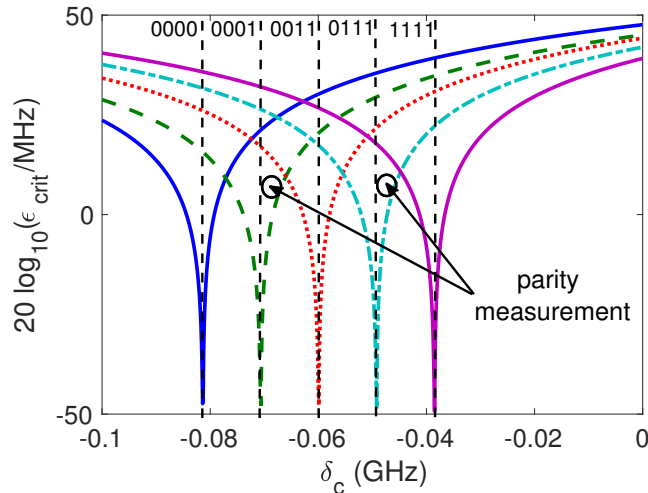
FIGURE 2.7:   *Value of $\epsilon_{\mathrm{crit}} = \epsilon$ depending on the detuning between drive and cavity frequency for four identical qbuits with the same parameters as in Fig. 2.6. The dotted vertical lines indicate the border, where the instable behavior disappears for larger detunings and the dynamics are just described by the low amplitude attractor. To measure parity we need to drive the system with two different frequencies. One such that δ_c lies in between the dotted vertical line of $|1111\rangle$ and $|0111\rangle$ and the other one such that δ_c lies in between the dotted vertical line corresponding to $|0011\rangle$ and $|0001\rangle$.*

8.3.1   Transformation of incoherent channels for $n \gg 1$

In this section we take a look at qubit intrinsic incoherent effects, such as dephasing and relaxation and how the corresponding Lindblad operators behave under the exact dispersive transformation. The consequence of such effects in the regime of small photon numbers is well studied [52, 94, 102, 103, 104] using the Polaron transformation, therefore we want to see how the system behaves in the regime in which we are interested, i.e. $n \gg 1$. Since we want to perform QND measurements our setup, it is important that the appearing dephasing and relaxation rates are not scaling with n or some other parameter that is huge in our regime of interest.

We want to focus on the case of the first section here, where we studied two three level systems coupled to a transmission line, again in the strong dispersive regime. The general case could also be calculated, but it is not necessary, since all leading effects that appear in the N qubit case with M energy levels taken into account will also appear in this easier system. For example leakage to the fourth level will be less probable than leakage to the third one, such that we get an upper bound for all higher leakage processes. Furthermore possible interactions between the qubits induced by the high photon number in the cavity will also appear in this smaller system, if they are present, which is the reason why we include the second qubit and not concentrate on one.

As mentioned, we are in the regime $n \gg 1$:

$$N_q = N_{\mathrm{QB}} + n \approx n, \tag{2.65}$$

such that $\Lambda(\hat{N}_q)$ acts like a scalar on qubit operators. Additionally we assume the semiclassical limit, such that

$$\hat{a} \to \alpha$$
$$\hat{a}^\dagger \to \alpha^*.$$

First we want to study relaxation of the first qubit with rate γ_1. The corresponding Lindblad operator is $\hat{L}_1^D = \sqrt{\gamma_1}\hat{\sigma}_{z,1}^D$. Therefore we have to calculate the transformation of $\hat{\sigma}_1$:

$$\hat{\sigma}_1 = \hat{D}^\dagger \hat{\sigma}_1 \hat{D} \tag{2.66}$$

$$= e^{\Lambda_1(n)I_{1,-} + \Lambda_2(n)I_{2,-}} \hat{\sigma}_1 e^{-\Lambda_1(n)I_{1,-} - \Lambda_2(N_q)I_{2,-}} \tag{2.67}$$

$$= \sum_{k=0}^\infty \frac{1}{k!} \left(\Lambda_1^k(n)\mathbf{ad}_{I_{-,1}}^k(\sigma_1) + \Lambda_2^k(n)\mathbf{ad}_{I_{-,2}}^k(\sigma_1) \right). \tag{2.68}$$

The expressions for the first commutator can be calculated in a closed form

$$\mathbf{ad}_{I_{-,1}}^{2k-1}\hat{\sigma}_1 = 2^{2(k-1)}\sqrt{n}^{2k-1}(-1)^k\hat{\sigma}_{z,1} \tag{2.69}$$

$$\mathbf{ad}_{I_{-,1}}^{2k}\hat{\sigma}_1 = \begin{cases} \hat{\sigma}_1 & k = 0 \\ 2^{2k-1}\sqrt{n}^{2k}(-1)^k\hat{\sigma}_{x,1} & k \geq 1 \end{cases}. \tag{2.70}$$

with $\sigma_{x,i} = |i-1\rangle\langle i| + |i\rangle\langle i-1|$. Putting (2.69) and (2.70) into (2.68) yields

$$\hat{\sigma}_1^D = \hat{\sigma}_1 - \frac{1}{2}\left(\frac{\arctan^2(2\lambda_1\sqrt{n})}{\sqrt{1+4\lambda_1^2 n}}\hat{\sigma}_{x,1} - \frac{2\lambda_1\sqrt{n}}{\sqrt{1+4\lambda_1^2 n}}\sigma_{z,1} \right) \tag{2.71}$$

$$+ \sum_{k=0}^\infty \frac{1}{k!}\Lambda_2^k(n)\mathbf{ad}_{I_{-,2}}^k\hat{\sigma}_1 \tag{2.72}$$

In the same manner we get a closed expression for the second operator. First we calculate two orders

$$\text{first order:} \qquad [I_{2,-}, \hat{\sigma}_1] = -\alpha^*|0\rangle\langle 2| \tag{2.73}$$

$$\text{second order:} \qquad -\alpha^*[I_{2,-}, |0\rangle\langle 2|] = -|\alpha|^2\hat{\sigma}_2. \tag{2.74}$$

In second order there appears the commutator between $I_{-,2}$ and $\hat{\sigma}_2$, which can be calculated with the formula (2.69) and (2.70), such that we get for $k \geq 1$

$$\mathbf{ad}_{I_{-,2}}^{2k-1} = (-1)^k\sqrt{n}^{2k-1}2^{2(k-2)}\Lambda_2^{2k-1}(n)\hat{\sigma}_{z,2} \tag{2.75}$$

$$\mathbf{ad}_{I_{-,2}}^{2k} = (-1)^k 2^{2k-3}\sqrt{n}^{2k}\Lambda_2^{2k}(n)\sigma_{x,2}. \tag{2.76}$$

Putting (2.75) and (2.76) and the expression for the first and second order into (2.72),

we get the full expression for $\hat{\sigma}_1^D$ which yields the following expression for the corresponding Lindblad operator:

$$
\begin{aligned}
L_1^D = {} & \gamma_1 \hat{\sigma}_1 \\
& + \frac{\gamma_1}{2} \frac{\arctan^2(2\lambda_1\sqrt{n})}{\sqrt{1+4\lambda_1^2 n}} \hat{\sigma}_{x,1} + \frac{\gamma_1}{8} \frac{\arctan^4(2\lambda_2\sqrt{n})}{\sqrt{1+4\lambda_2^2 n}} \hat{\sigma}_{x,2} \\
& + \gamma_1 \frac{\lambda_1\sqrt{n}}{\sqrt{1+4\lambda_1^2 n}} \hat{\sigma}_{z,1} + \frac{\gamma_1}{4} \frac{\sqrt{n}\lambda_2 \arctan^2(2\lambda_2 n)}{\sqrt{1+4\lambda_1^2 n}} \hat{\sigma}_{z,2} \\
& + \frac{\gamma_1}{2} \arctan(2\lambda_2 n)\hat{\sigma}_1\hat{\sigma}_2 - \frac{\gamma_1}{8}\arctan^2(2\lambda_2 n)\hat{\sigma}_2
\end{aligned}
\tag{2.77}
$$

We observe as a first term the original relaxation with rate γ_1 and six additional terms. The first one is a dephasing in the $\hat{\sigma}_{x,1}$ basis, which leads to a mixing of the ground and first excited state. The corresponding rate has an *arctan* in the numerator and a term proportional to $\sqrt{n}$ in the denominator, which leads to a rate much smaller than γ_1 for $n \gg 1$. The same argument holds for the second term, which leads to a dephasing in the $\sigma_{x,2}$ basis. This term has no crucial effect on the qubit as well. The third term leads to a dephasing between the ground and first excited state. The rate here is smaller than the original relaxation rate γ_1 for all values of n. The fourth term leads to a dephasing between the first excited state and the second excited state. Here we observe a rate which will also be in the order of the original γ_1, since we have $\sqrt{n}$ in the numerator as well as the denominator. The fifth and sixth term lead to interactions between the second excited state and the ground and first excited state, respectively. Anyways the rates here are again at the order of the original relaxation rate γ_1. All in all we have shown that relaxation in this system leads to additional incoherent effects, but all are happening with a rate smaller or comparable with γ_1. Since we need condition (2.15) to perform any quantum mechanical operations with the system, nothing crucial happens here.

Now we take a look at dephasing between the ground and first excited state. The corresponding Lindblad operator can be written as $L_\varphi^D = \gamma_\varphi \sigma_{z,1}^D$. The calculation can be performed in the same way as for $\hat{\sigma}_1^D$, where we need the following commutators:

$$
\mathbf{ad}_{I_{-,1}}^{2k-1}\hat{\sigma}_{z,1} = (-1)^{k-1}2^{2k-1}\sqrt{n}^{2k-1}\sigma_{x,1}
\tag{2.78}
$$

$$
\mathbf{ad}_{I_{-,1}}^{2k}\hat{\sigma}_{z,2} = (-1)^k 2^{2k}\sqrt{n}^{2k}\hat{\sigma}_{z,1}
\tag{2.79}
$$

$$
\mathbf{ad}_{I_{-,2}}^{2k-1}\hat{\sigma}_{z,1} = (-1)^k 2^{2(k-1)}\sqrt{n}^{2k-1}\hat{\sigma}_{x,2}
\tag{2.80}
$$

$$
\mathbf{ad}_{I_{-,2}}^{2k}\hat{\sigma}_{z,1} = (-1)^k 2^{2k-1}\sqrt{n}^{2k}\hat{\sigma}_{z,2},
\tag{2.81}
$$

which yields the following expression for the dephasing operator in the new frame:

$$
\begin{aligned}
L_\varphi^D = {} & \gamma_\varphi \hat{\sigma}_{z,1} \\
& - \gamma_\varphi \frac{\arctan^2(2\lambda_1\sqrt{n})}{\sqrt{1+4\lambda_1^2 n}} \hat{\sigma}_{z,1} - \frac{\gamma_\varphi}{2} \frac{\arctan^2(2\lambda_2\sqrt{n})}{\sqrt{1+4\lambda_2^2 n}} \hat{\sigma}_{z,2} \\
& - \gamma_\varphi \frac{2\lambda_1\sqrt{n}}{1+4\lambda_1^2 n} \hat{\sigma}_{x,1} - \gamma_\varphi \frac{\lambda_2\sqrt{n}}{\sqrt{1+4\lambda_2^2 n}} \hat{\sigma}_{x,2}.
\end{aligned}
\tag{2.82}
$$

Again we have the original dephasing term appearing in the Lindblad operator with rate γ_1. The first two additional terms lead to dephasing between the ground state and the first excited state and the first excited state and the second one, respectively. The rates are extremely small in the regime $n \gg 1$ such that we can neglect them.

The last two terms lead to dephasing in the $\hat{\sigma}_{x,1}$ and $\hat{\sigma}_{x,2}$ basis, but with a rate at least smaller than the original dephasing rate γ_φ.

All in all we have shown that we do not have any relevant incoherent processes affecting the qubits, with rates higher than the relaxation and dephasing rate of the qubit. This gives the possibility to perform QND measurements in this regime.

8.3.2   Dephasing due to photon leakage

In the parity measurement protocol we assumed a cavity decay rate κ, which is greater than the intrinsic incoherent rates of the qubits. This assumption is important to reach the pseudo steady state and measure before the qubit states decay. Since states with the same parity can lead to different cavity frequency shifts (see Fig. 2.3), the photons leaking out of the cavity carry qubit information. This leakage leads to an effective dephasing (see e.g. [105]) of superpositions of parity states. We want to study this process and calculate the respective dephasing rate. Note that only even parity states cause different shifts in the cavity, since odd parity states are in the high amplitude attractor, where the frequency is exactly the bare cavity frequency for all states (see see Fig. 2.3). Therefore we only study the dephasing between even parity states.

In the measurement protocol, the drive strength is chosen such that the system stays in the low amplitude attractor for even parity states. Here the behavior is still linear (see 2.3), hence we can approximate the Hamiltonian (2.26)

$$\hat{H} \approx \hat{H}_0 + \sum_{j=1}^{2} \sum_{i=1}^{2} \frac{\left(g_i^{(j)}\right)^2}{\Delta_i^{(j)}} \hat{a}^\dagger \hat{a} \hat{\sigma}_{z,i}^{(j)} + \hat{H}_d, \tag{2.83}$$

where we assumed that we are already in the frame rotating with the drive frequency. The incoherent evolution of the density matrix is described by the Lindbladian master equation

$$\begin{aligned}
\dot{\rho} = &-i\left[H, \rho\right] + \kappa \mathcal{D}[\hat{a}]\rho \\
&+ \sum_{j=1}^{2} \sum_{i=1}^{2} \gamma_{1,\mathrm{i}} \mathcal{D}[\hat{\sigma}_i^{(j)}] + \sum_{j=1}^{2} \sum_{i=1}^{2} \gamma_{\Phi,\mathrm{i}} \mathcal{D}[\hat{\sigma}_{z,i}^{(j)}],
\end{aligned} \tag{2.84}$$

which includes three incoherent processes, photon loss of the cavity with rate κ, relaxation with rate $\gamma_{1,i}$ and dephasing with rate $\gamma_{\Phi,i}$. We assume the intrinsic incoherent rates to be equal for all qubits. The qubit-cavity density matrix of an equal superposition of even parity states can be written down as (for simplicity we label $|00\rangle = |0\rangle$ and $|11\rangle = |1\rangle$)

$$\hat{\rho} = \hat{\rho}_{00}^c |0\rangle\langle 0| + \hat{\rho}_{01}^c |0\rangle\langle 1| + \hat{\rho}_{10}^c |1\rangle\langle 0| + \hat{\rho}_{11}^c |1\rangle\langle 1|, \tag{2.85}$$

where $\hat{\rho}_{ij}^c$ describe the field part of the density matrix. Putting this density matrix expression into (2.84) we get equations of motion for the density matrix elements $\hat{\rho}_{ij}$. These can be solved using the positive-P representation leading to the time evolution of the density matrix

$$\hat{\rho}(t) = \sum_{i,j=0}^{1} c_{ij}(t) |i\rangle\langle j| \otimes |\alpha_i(t)\rangle\langle\alpha_j(t)| \tag{2.86}$$

For the detailed calculation see Appendix 8.D. The induced qubit dephasing is described by the parameter

$$c_{10}(t) = \frac{a_{10}(t)}{\langle \alpha_1(t) | \alpha_0(t) \rangle}, \tag{2.87}$$

with

$$a_{10} = a_{10}(0) \mathrm{e}^{\left[-(\gamma_2 + i\tilde{\omega})t \right]} \mathrm{e}^{\left[-i4(\chi_1 - \chi_2/2) \int_0^t \alpha_1(t')\alpha_0^*(t')\mathrm{d}t' \right]} \tag{2.88}$$

and

$$\alpha_1(t) = \alpha_1^s + \mathrm{e}^{\left[-(\frac{\kappa}{2} + i2(\chi_1 - \chi_2) + i\delta_c)t \right]} \left(\alpha_1(0) - \alpha_1^s \right) \tag{2.89}$$

$$\alpha_0(t) = \alpha_0^s + \mathrm{e}^{\left[-(\frac{\kappa}{2} - i2\chi_1 + i\delta_c) \right]} \left(\alpha_0(0) - \alpha_0^s \right). \tag{2.90}$$

The steady state values of the field operators are given by

$$\alpha_1^s = \frac{-i\epsilon}{\kappa/2 + i2(\chi_1 - \chi_2) + i\delta_c} \tag{2.91}$$

$$\alpha_0^s = \frac{-i\epsilon}{\kappa/2 - i2\chi_1 + i\delta_c}. \tag{2.92}$$

The results are similar to [105], but get an additional χ_2 contribution from the third energy level. This leads to a no longer symmetric dependence of the dephasing rate on the detuning δ_c, which can be explained by the asymmetric frequency shift of the cavity (in the two-level case the shift is $\pm\chi$). Note that we assumed identical qubits in the derivation such that the appearing linear shifts read $\chi_i = g_i^2/\Delta_i$. The measurement should be performed in a pseudo steady state, when system dynamics are almost zero. Therefore we assume the limit $\kappa t \gg 1$, where the photon leakage induced dephasing rate can be written as

$$\Gamma_\Phi = -4(\chi_1 - \chi_2/2)\mathrm{Im}\left\{ \alpha_1^s \alpha_0^s * \right\}. \tag{2.93}$$

Putting all together we finally get the following expression for the dephasing rate induced by photon leakage of the cavity

$$\Gamma_\Phi = \frac{4\kappa\epsilon^2\chi_2}{\left(\frac{\kappa^2}{4} + \delta_c^2 + 2\delta_c\chi_2 + 4\chi_1^2 - 4\chi_1\chi_2 \right)^2 + \kappa^2\chi_2^2} \tag{2.94}$$

For the parameters in Fig. 2.4, for the two qubit parity measurement protocol the detuning is $\delta_c \approx -20$ MHz and the corresponding drive strength is $\epsilon \approx 10$ MHz. These parameters lead to an effective dephasing of the qbuit with rate $\Gamma_\Phi \approx 9$ kHz. Since the cavity decay is assumed to be in the range of a few MHz, we can assume that a pseudo steady state is reached before the cavity photon loss has a significant decoherence effect on the superposition of equal parity states which leaves the measurement QND. Anyways, Γ_Φ and the intrinsic relaxation and dephasing rates give a limiting factor to the fidelity of the measurement. For the N qubit case the result is similar, but since there are more than one drive strengths needed, we also have more dephasing channels. However, they are all in the range of a few kHz, hence even adding all of them up does not lead to a significant dephasing as long as the number of qubits does not get too large.

Note that one could as well use the Polaron Transformation in the manner of [104] to calculate the repsective dephasing rate

8.4 Conclusion

In conclusion we have derived a mathematical description of N superconducting qubits coupled dispersively to a microwave cavity by generalizing the exact dispersive transformation. We have obtained that our system of interest shows a nonlinear behavior for a critical drive strength, that results in a huge enhancement ($\sim 10^5$ photons) of the photon occupation in the microwave cavity. This critical drive strength depends on the qubit state and can therefore be used for high efficiency state readout.

Furthermore we have shown that the state dependent critical drive strength can be varied by the detuning between cavity and drive. Due to this dependence it is possible to perform various high efficiency measurements including multi-qubit parity readout, using a microwave photon counter to measure the cavity occupation and we have shown how to tune the system to realize these measurements. We gave expressions for the drive frequencies to perform mutli-qubit parity measurements, where one needs $\lfloor \frac{N}{2} \rfloor$ different drive frequencies to measure the parity of N coupled qubits.

Additionally we studied the effect of relaxation and dephasing in the high occupation regime and have shown that the appearing incoherent rates are smaller or equal to the original rates. Also the photon leakage rate of the cavity does not lead to a fast decay of qubit coherence. There are some other incoherent processes that could be considered (like broadening due to photon number variations of equal parity states [21]), but they are not as significant as the studied processes in typical Transmon systems. This makes the presented protocol a candidate for high contrast QND parity readout.

Appendices

8.A Frequency Transformation in the Bare Hamiltonian

We start with the bare qubit and cavity Hamiltonian

$$\hat{H}_0 = \omega_c \hat{a}^\dagger \hat{a} + \sum_{j=1}^{N} \sum_{i=0}^{M-1} \omega_i^{(j)} |i\rangle \langle i|^{(j)} . \tag{2.95}$$

The goal is to transform the state projection operators $|i\rangle \langle i|^{(j)}$ into the operators

$$\hat{\sigma}_{z,i}^{(j)} = - |i-1\rangle \langle i-1|^{(j)} + |i\rangle \langle i|^{(j)} , \tag{2.96}$$

such that we end up with a Hamiltonian of the form

$$\hat{H}_0 = \delta_c \hat{a}^\dagger \hat{a} + \sum_{j=1}^{N} \sum_{i=1}^{N} \tilde{\omega}_i^{(j)} \frac{\hat{\sigma}_{z,i(j)}}{2} . \tag{2.97}$$

Comparing (2.95) and (2.97) we get the following transformation rule for the frequencies:

$$2\omega_0^{(j)} = -\tilde{\omega}_1^{(j)} + \sum_{k=1}^{M-1} \beta_j^{(j)} \tilde{\omega}_j^{(j)}$$

$$2\omega_1^{(j)} = \tilde{\omega}_1^{(j)} - \tilde{\omega}_2^{(j)} + \sum_{k=1}^{M-1} \beta_j^{(j)} \tilde{\omega}_j^{(j)}$$

$$2\omega_2^{(j)} = \tilde{\omega}_2^{(j)} - \tilde{\omega}_3^{(j)} + \sum_{k=1}^{M-1} \beta_j^{(j)} \tilde{\omega}_j^{(j)}$$

$$\vdots$$

$$2\omega_{M-2}^{(j)} = \tilde{\omega}_{M-2}^{(j)} - \tilde{\omega}_{M-1}^{(j)} + \sum_{k=1}^{M-1} \beta_j^{(j)} \tilde{\omega}_j^{(j)}$$

$$2\omega_{M-1}^{(j)} = \tilde{\omega}_{M-1}^{(j)} + \sum_{k=1}^{M-1} \beta_j^{(j)} \tilde{\omega}_j^{(j)},$$

where $\beta_j^{(j)}$ is an arbitrary complex number. The last term in the equations comes from the fact that we can add an arbitrary vacuum contribution to the Hamiltonian in every qubit subspace without changing the system dynamics. Subtracting the second equation from the first and so on for every pair of neighboring equations leads

to

$$2\omega_{10}^{(j)} = \omega_1^{(j)} - \omega_0^{(j)} = 2\tilde{\omega}_1^{(j)} - \tilde{\omega}_2^{(j)}$$
$$2\omega_{21}^{(j)} = -\tilde{\omega}_1^{(j)} + 2\tilde{\omega}_2^{(j)} - \tilde{\omega}_3^{(j)}$$
$$2\omega_{32}^{(j)} = -\tilde{\omega}_2^{(j)} + 2\tilde{\omega}_3^{(j)} - \tilde{\omega}_4^{(j)}$$
$$\vdots$$
$$2\omega_{M-2,M-3}^{(j)} = -\tilde{\omega}_{M-3}^{(j)} + 2\tilde{\omega}_{M-2}^{(j)} - \tilde{\omega}_{M-1}^{(j)}$$
$$2\omega_{M-1,M-2}^{(j)} = -\tilde{\omega}_{M-2}^{(j)} + 2\tilde{\omega}_{M-1}^{(j)}.$$

This can be written down in a matrix representation

$$2\omega_{i,i-1}^{(j)} = \sum_{k=1}^{M-1} A_{i,k}\tilde{\omega}_k^{(j)}, \tag{2.100}$$

with the transformation matrix

$$A = \begin{pmatrix} 2 & -1 & 0 & 0 & 0 & 0 & \cdots & 0 \\ -1 & 2 & -1 & 0 & 0 & 0 & \cdots & 0 \\ 0 & -1 & 2 & -1 & 0 & 0 & \cdots & 0 \\ & & & \ddots & \ddots & \ddots & & \vdots \\ 0 & & \cdots & \cdots & & -1 & 2 & -1 \\ 0 & & \cdots & \cdots & & & -1 & 2 \end{pmatrix}. \tag{2.101}$$

This is a Töplitz matrix with $c = b = -1$ and $a = 2$. The inverse of this kind of Töplitz matrix can be found in literature and is given by

$$A^{-1} = \begin{cases} P_{ij} & 1 \le i \le j \\ Q_{ij} & j \le i \le n \end{cases}, \tag{2.102}$$

with

$$P_{ij} = -\frac{i(j-n-1)}{(n+1)}$$
$$Q_{ij} = -\frac{j(i-n-1)}{(n+1)}.$$

Combining all these results the frequencies $\tilde{\omega}_i^{(j)}$ can be calculated as

$$\tilde{\omega}_i^{(j)} = \sum_{k=1}^{M-1} 2A_{i,k}^{-1}\left(\omega_k^{(j)} - \omega_{k-1}^{(j)}\right). \tag{2.103}$$

8.B   Exact Dispersive Transformation

In this section of the appendix we show how to diagonalize the Hamiltonian

$$\hat{H}_{\text{sys}} = H_0 + H_{\text{int}}. \tag{2.104}$$

To do so we apply the unitary transformation

$$\hat{D} = \exp\left[-\sum_{j=1}^{N}\sum_{i=1}^{M-1}\Lambda_i^{(j)}(\hat{N}_i)\hat{I}_{-,i}^{(j)}\right], \tag{2.105}$$

where $\Lambda_i^{(j)}(N_i)$ is a scalar function of $\hat{N}_i$. The excitation number of every subspace ($\hat{N}_i$) is assumed to be constant, such that Λ acts like a scalar on the system Hamiltonian. We use the Baker Campbell Hausdorff formula

$$\mathrm{e}^{A}B\mathrm{e}^{-A} = \sum_{m=0}^{\infty}\frac{1}{m!}\mathbf{ad}_A^n B. \tag{2.106}$$

Before we transform $\hat{H}_{\mathrm{sys}}$ we calculate some important commutators. It is easy to show that

$$\left[\hat{I}_{-,i}^{(j)}, \hat{H}_0\right] = \tilde{\Delta}_i^{(j)} I_{+,i}, \tag{2.107}$$

where

$$\tilde{\Delta}_i^{(j)} = \begin{cases} \delta_1^{(j)} - \frac{\tilde{\omega}_2^{(j)}}{2}, & i = 1 \\ \Delta_{M-1}^{(j)} - \frac{\tilde{\omega}_{M-2}^{(j)}}{2}, & i = M-1 \\ \Delta_i^{j} - \left(\frac{\tilde{\omega}_{i-1}^{(j)}+\tilde{\omega}_{i+1}^{(j)}}{2}\right), & \text{else.} \end{cases} \tag{2.108}$$

and the definitions of Sec. 8.1.1. With this commutator relation, we can calculate the transformation

$$\hat{D}^{\dagger}H_{\mathrm{sys}}\hat{D} = \hat{H}_0 + \sum_{j=1}^{N}\sum_{i=1}^{M-1}g_i^{(j)}\hat{I}_{-,i} \tag{2.109}$$

$$+ \sum_{k=1}^{\infty}\frac{1}{k!}\sum_{j=1}^{N}\sum_{i=1}^{M-1}\mathbf{ad}_{\Lambda_i^{(j)}I_{-,i}}^k\left(\hat{H}_0 + \sum_{l=1}^{M-1}g_l^{(j)}\hat{I}_{-,l}\right) \tag{2.110}$$

$$= \hat{H}_0 + \sum_{k=0}^{\infty}g_i^{(j)}\frac{k+1}{(k+1)!}\mathbf{ad}_{\Lambda_i^{(j)}I_{-,i}}^k\left(\hat{I}_{+,i}^{(j)}\right) \tag{2.111}$$

$$+ \sum_{k=0}^{\infty}\sum_{j=1}^{N}\sum_{i=1}^{M-1}\mathbf{ad}_{\Lambda_i^{(j)}I_{-,i}}^k\left(\hat{I}_{+,i}\right) \tag{2.112}$$

$$= \hat{H}_0 + \sum_{N,M}\sum_{k=1}^{\infty}\frac{(k+1)g_i^{(j)}+\tilde{\Delta}_i^{(j)}\Lambda_i^{(j)}}{(k+1)!}\mathbf{ad}_{\Lambda_i^{(j)}I_{-,i}}\left(\hat{I}_{+,i}\right). \tag{2.113}$$

Here we made two steps, where we take use of the two relations we proof in Sec. 8.C. The firs one is, that we splitted the two parts of the Hamiltonian on the right entry of the nested commutators, so we assumed

$$\mathbf{ad}_{\sum_{i=1}^{M-1}\Lambda_i\hat{I}_{-,i}}^k\hat{H}_0 = \sum_{i=1}^{M-1}\mathbf{ad}_{\Lambda_i\hat{I}_{-,i}}\hat{H}_0 \tag{2.114}$$

which is true due to the fact that $\left[\hat{I}_{-,i}, \hat{I}_{-,j}\right] = 0$ for $i \neq j$, if we ignore non parity conserving terms and $\left[\hat{I}_{-,i}\left[\hat{H}_0, \hat{I}_{-,j}\right]\right] = 0$. The last relations is true since $\left[\hat{H}_0, I_{-,j}\right] \propto \hat{I}_{-,j}$. Using this relations and the proof in Appendix. 8.C , (2.114) is true.

On the other hand, we used that

$$\mathbf{ad}^k_{\sum_{i=1}^{M-1}\Lambda_i\hat{I}_{-,i}}\left(\sum_{j=1}^{M-1}\hat{I}_{+,j}\right) = \sum_{i=1}^{M-1}\mathbf{ad}^k_{\Lambda_i\hat{I}_{-,i}}\hat{I}_{+,i}, \tag{2.115}$$

which is true due to the proof in Appendix 8.C and with the relation $\left[I_{-,i}, \hat{I}_{+,j}\right] = 0$ for $i \neq j$ again up to non parity conserving terms.

There only appears one commutator in the expression and it can easily be calculated to be

$$\mathbf{ad}^{2n}_{\Lambda_i^{(j)}I_{-,i}}\left(\hat{I}_{+,i}^{(j)}\right) = (-4)^n\Lambda_i^{(j)2n}N_i^nI_{+,i} \tag{2.116}$$

$$\mathbf{ad}^{2n+1}_{\Lambda_i^{(j)}I_{-,i}}\left(\hat{I}_{+,i}^{(j)}\right) = -2(-4)\Lambda_i^{(j)2n+1}N_i^{n+1}\sigma_{z,i}. \tag{2.117}$$

Putting (2.117) into (2.113) we end up with:

$$\hat{H}^D_{\text{sys}} = \hat{H}_0 \tag{2.118}$$

$$+ \sum_{j=1}^N\sum_{i=1}^{M-1}\left(\left[\frac{\tilde{\Delta}_i^{(j)}\sin\left(2\Lambda_i^{(j)}\sqrt{N_i}\right)}{2\sqrt{N_i}} + g_i^{(j)}\cos\left(2\Lambda_i^{(j)}\sqrt{N_i}\right)\right]I_{+,1} \tag{2.119}$$

$$-2N_i\sigma_{z,i}\left[\frac{g_i^{(j)}\sin\left(2\Lambda_i^{(j)}\sqrt{N_i}\right)}{2\sqrt{N_i}} + \frac{\tilde{\Delta}_i^{(j)}\left\{1-\cos\left(2\Lambda_i^{(j)}\sqrt{N_i}\right)\right\}}{4N_i}\right]\right). \tag{2.120}$$

To get a diagonal Hamiltonian we have to define the scalar functions $\Lambda_i^{(j)}$ as follows:

$$\Lambda_i^{(j)}(N_i) = -\frac{\arctan\left(2\lambda_i^{(j)}\sqrt{N_i}\right)}{2\sqrt{N_i}}. \tag{2.121}$$

With this choice for $\Lambda_i^{(j)}$ we end up with a diagonal system Hamiltonian

$$\hat{H}^D_{\text{sys}} = \delta_c\hat{a}^\dagger\hat{a} + \hat{H}_0 - \sum_{j=1}^N\sum_{i=1}^{M-1}\frac{\tilde{\Delta}_i^{(j)}}{2}\left(1 - \sqrt{1 + \frac{g_i^{(j)}}{\tilde{\Delta}_i^{(j)}}N_i}\right) \tag{2.122}$$

8.C The Effect of Higher Energy Levels

In this section of the appendix we want to show that only the lowest non occupied energy level (in our case $|2\rangle$) of the qubits has an effect on the results. Including even higher levels does not change either the frequency shifts nor the behavior of the photon amplitude. This can be seen in Fig. 2.8 where we show the effective frequency shift and compare the results when we include the lowest three energy levels with the results when we include the lowest ten. One sees that the results of the two cases are completely identical, such that we can claim that only the three lowest levels affect
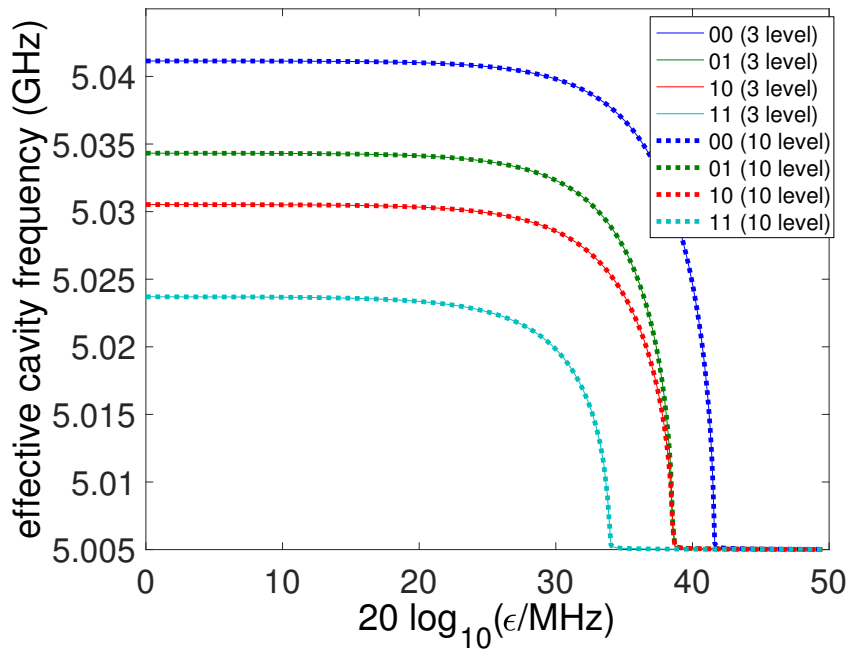
FIGURE 2.8: *Comparison between the results of the effective cavity frequency when including three or ten energy levels. We see that the results are absolutely identical, such that it seems to be reasonable to only include the lowest non occupied energy level into the calculations to get correct results. The parameters are the same as in Fig. 2.3.*

the results. More precisely it seems reasonable that the lowest non occupied energy level is the last one that has an effect on the system.

8.D   Proofs for Exact Dispersive Transformation

In this section of the appendix we will prove two relations for nested commutators that we need to split up terms when we perform the exact dispersive transformation including more than two energy levels.

8.D.1   First Proof

Given four operators A, B, C, and D, we want to show that

$$\mathbf{ad}_{A+B}^n (B + C) = \mathbf{ad}_A^n(C) + \mathbf{ad}_B^n(D),$$ (2.123)

if the following relation is fulfilled:

$$[A, B] = [A, D] = [B, C] = [C, D] = 0.$$ (2.124)

We use induction to show that (2.123) is valid for all n. Let's start with the case $n = 1$ which is trivial:

$$[A + B, C + D] \underbrace{=}_{(2.124)} [A, C] + [B, D].$$ (2.125)

So we now that for $n = 1$ the relation holds. Lets assume that for $n = k$ (2.125) holds, that is

$$\mathbf{ad}_{A+B}^k(C + D) = \mathbf{ad}_A^k(C) + \mathbf{ad}_B^k(D). \tag{2.126}$$

Let $n = k + 1$:

$$
\begin{aligned}
\mathbf{ad}_{A+B}^{k+1}(C + D) &= \left[A + B, \mathbf{ad}_{A+B}^k(C + D)\right] \\
&= \left[A + B, \mathbf{ad}_A^k(C) + \mathbf{ad}_B^k(D)\right] \\
&= \left[A, \mathbf{ad}_A^k(C)\right] + \left[B, \mathbf{ad}_B^k(D)\right] \\
&\quad + \left[A, \mathbf{ad}_B^k(D)\right] + \left[B, \mathbf{ad}_A^k(C)\right].
\end{aligned}
\tag{2.127}
$$

To get the relation we want, we have to show that

$$\left[A, \mathbf{ad}_B^k(D)\right] = \left[B, \mathbf{ad}_A^k(C)\right] = 0. \tag{2.128}$$

For this we again use induction and only show it for one of the terms, since the second calculation is analog. Again the case $n = 1$ is fulfilled:

$$[A, [B, D]] = -[B, [D, A]] - [D, [A, B]] \underbrace{=}_{(2.124)} 0, \tag{2.129}$$

where we used the Jacobi-identity for operators. So lets assume the statement is true for $n = k$. Let $n = k + 1$

$$\left[A, \mathbf{ad}_B^{k+1}(D)\right] = \left[A, \left[B, \mathbf{ad}_B^k(D)\right]\right] \tag{2.130}$$

$$= -\left[B, \left[\mathbf{ad}_B^k(D), A\right]\right] - \left[\mathbf{ad}_B^k(D), [A, B]\right] = 0 \tag{2.131}$$

where we again used the Jacobi-identity and the induction hypothesis. In the same manner we can show that $\left[B, \mathbf{ad}_A^k(C)\right] = 0$, such that we finally proofed (2.125) under the condition (2.124) for all $n \in \mathbb{N}$.

8.D.2 Second Proof

Here want to prove a second identity we need to perform the exact dispersive transformation in our case. We show that

$$\mathbf{ad}_{A+B}^k(C) = \mathbf{ad}_A^k(C) + \mathbf{ad}_B^k(C), \tag{2.132}$$

if the following relations are satisfied:

$$[A, B] = 0 \tag{2.133}$$

$$[B, [C, A]] = [A, [C, B]] = 0. \tag{2.134}$$

Again we use induction. The identity is trivial to show for $n = 1$. So we assume (2.132) holds for $n = k$. Let $n = k + 1$:

$$\mathbf{ad}_{A+B}^{k+1}(C) = \left[A + B, \mathbf{ad}_{A+B}^k(C)\right] \tag{2.135}$$

$$= \left[A + B, \mathbf{ad}_A^k(C) + \mathbf{ad}_B^k(C)\right] \tag{2.136}$$

$$= \mathbf{ad}_A^{k+1}(C) + \mathbf{ad}_B^{k+1}(C) \tag{2.137}$$

$$+ \left[A, \mathbf{ad}_B^k(C)\right] + \left[B, \mathbf{ad}_A^k(C)\right]. \tag{2.138}$$

To prove (2.132) we therefore have to show that

$$\left[A, \mathbf{ad}_B^k(C)\right] = \left[B, \mathbf{ad}_A^k(C)\right] = 0. \tag{2.139}$$

We start with the first term. For $n = 1$:

$$[A, [B, C]] = -[B, [C, A]] - [C, [A, B]] = 0, \tag{2.140}$$

where we used the Jacobi-identity and relations (2.133) and (2.134). Let's assume we have proven the identity for $n = k$. Let $n = k + 1$:

$$\left[A, \mathbf{ad}_B^{k+1}(C)\right] = \left[A, \left[B, \mathbf{ad}_B^k(C)\right]\right] \tag{2.141}$$

$$= -\left[B, \left[\mathbf{ad}_B^k(C), A\right]\right] - \left[\mathbf{ad}_B^k(C), [A, B]\right] = 0 \tag{2.142}$$

Likewise one can show that $\left[B, \mathbf{ad}_A^k(C)\right] = 0$ and therefore we have proven the identity (2.132) under the conditions (2.133) and (2.134) for all $n \in \mathbb{N}$.

8.E Equation System to Determine Dephasing

Here we solve the equation system to get the expression for the cavity leakage induced dephasing of Sec. 8.3.1. Putting the density matrix (2.85) into the Lindblad equation (2.84) we get equations of motion for the cavity parts of the density matrix

$$\dot{\hat{\rho}}_{11} = \kappa \mathcal{D}[\hat{a}]\hat{\rho}_{11} - (\gamma_1^{(1)} + \gamma_1^{(2)})\hat{\rho}_{11} - i\epsilon\left[\hat{a}^\dagger + \hat{a}, \hat{\rho}_{11}\right] - i(\chi_1^{(1)} + \chi_1^{(2)})\left[\hat{a}^\dagger\hat{a}, \hat{\rho}_{11}\right] - i\delta_c\left[\hat{a}^\dagger\hat{a}, \hat{\rho}_{11}\right]$$

$$\tag{2.143}$$

$$\dot{\hat{\rho}}_{00} = \kappa \mathcal{D}[\hat{a}]\hat{\rho}_{00} + (\gamma_1^{(1)} + \gamma_1^{(2)})\hat{\rho}_{11} - i\epsilon\left[\hat{a}^\dagger + \hat{a}, \hat{\rho}_{00}\right] + i(\chi_1^{(1)} + \chi_1^{(2)})\left[\hat{a}^\dagger\hat{a}, \hat{\rho}_{00}\right] - i\delta_c\left[\hat{a}^\dagger\hat{a}, \hat{\rho}_{00}\right]$$

$$\tag{2.144}$$

$$\dot{\hat{\rho}}_{10} = \kappa \mathcal{D}[\hat{a}]\hat{\rho}_{10} - (\gamma_2^{(1)} + \gamma_2^{(2)})\hat{\rho}_{10} - i\epsilon\left[\hat{a}^\dagger + \hat{a}, \hat{\rho}_{10}\right]$$

$$- i\left[(\chi_1^{(1)} + \chi_1^{(2)})\left\{\hat{a}^\dagger\hat{a}, \hat{\rho}_{10}\right\} - (\chi_2^{(1)} + \chi_2^{(2)})\hat{a}^\dagger\hat{a}\hat{\rho}_{10}\right] - i\delta_c\left[\hat{a}^\dagger\hat{a}, \hat{\rho}_{10}\right] - i(\tilde{\omega}_1 + \frac{\tilde{\omega}_2}{2})\hat{\rho}_{10}$$

$$\tag{2.145}$$

$$\dot{\hat{\rho}}_{01} = \kappa \mathcal{D}[\hat{a}]\hat{\rho}_{01} - (\gamma_2^{(1)} + \gamma_2^{(2)})\hat{\rho}_{01} - i\epsilon\left[\hat{a}^\dagger + \hat{a}, \hat{\rho}_{01}\right]$$

$$+ i\left[(\chi_1^{(1)} + \chi_1^{(2)})\left\{\hat{a}^\dagger\hat{a}, \hat{\rho}_{10}\right\} - (\chi_2^{(1)} + \chi_2^{(2)})\hat{\rho}_{10}\hat{a}^\dagger\hat{a}\right] - i\delta_c\left[\hat{a}^\dagger\hat{a}, \hat{\rho}_{01}\right] + i(\tilde{\omega}_1 + \frac{\tilde{\omega}_2}{2})\hat{\rho}_{01},$$

$$\tag{2.146}$$

where $\gamma_2^{(j)} = \gamma_1^{(j)} + \gamma_\Phi^{(j)}/2$ and $\chi_i^{(j)} = (g_i^{(j)})^2/\tilde{\Delta}_i^{(j)}$. Now we assume that both qubits have the same relaxation and dephasing rate and define $\tilde{\omega} = \tilde{\omega}_1 + \tilde{\omega}_2/2$. In general there exist no solution for these four equations because of the coupling term introduced by γ_1. In our case we are only interested in dephasing rate, such that we can set $\gamma_1 = 0$ in the equations for the diagonal parts. To solve the above equation system, we consult the generalized P representation and express the cavity density matrix elements as

$$\hat{\rho}_{ij}^c = \int \Lambda(\alpha, \beta) P(\alpha, \beta) \mathrm{d}\mu(\alpha, \beta), \tag{2.147}$$

with probability densities P_{ij}. Here we use the so called positive-P representation, where

$$\Lambda(\alpha, \beta) = \frac{|\alpha\rangle \langle \beta^*|}{\langle \beta^*|\alpha\rangle} \tag{2.148}$$

$$\mathrm{d}\mu(\alpha, \beta) = \mathrm{d}^2\alpha \mathrm{d}^2\beta \tag{2.149}$$

Putting the positive-P representation of the matrix elements into equations (2.143)-(2.146) using the relations (see e.g. [106])

$$\hat{a}\Lambda(\alpha, \beta) = \alpha\Lambda(\alpha, \beta) \tag{2.150}$$

$$\hat{a}^\dagger\Lambda(\alpha, \beta) = (\beta + \partial_\alpha)\Lambda(\alpha, \beta) \tag{2.151}$$

$$\Lambda(\alpha, \beta)\hat{a}^\dagger = \beta\Lambda(\alpha, \beta) \tag{2.152}$$

$$\Lambda(\alpha, \beta)\hat{a} = (\partial_\beta + \alpha)\Lambda(\alpha, \beta) \tag{2.153}$$

we get equations of motion for these probability densities

$$\dot{P}_{11} = \partial_\alpha \left[(i\epsilon + 2i(\chi_1 - \chi_2)\alpha + i\delta_c\alpha + \kappa\alpha/2)P_{11} \right] + \partial_\beta \left[(-i\epsilon - 2i(\chi_1 - \chi_2)\beta - i\delta_c\beta + \kappa\beta/2)P_{11} \right]$$
$$\tag{2.154}$$

$$\dot{P}_{00} = \partial_\alpha \left[(i\epsilon - 2i\chi_1\alpha + i\delta_c\alpha + \kappa\alpha/2)P_{00} \right] + \partial_\beta \left[(-i\epsilon + 2i\chi_1\beta - i\delta_c\beta + \kappa\beta/2)P_{00} \right]$$
$$\tag{2.155}$$

$$\dot{P}_{10} = \partial_\alpha \left[(i\epsilon + 2i(\chi_1 - \chi_2)\alpha + i\delta_c\alpha + \kappa\alpha/2)P_{10} \right] + \partial_\beta \left[(-i\epsilon + 2i\chi_1\beta - i\delta_c\beta + \kappa\beta/2)P_{10} \right]$$
$$- i4(\chi_1 - \chi_2/2)\alpha\beta P_{10} - 2\gamma_2 P_{10} - i\tilde{\omega}P_{10}$$
$$\tag{2.156}$$

$$\dot{P}_{01} = \partial_\alpha \left[(i\epsilon - 2i\chi_1\alpha + i\delta_c\alpha + \kappa\alpha/2)P_{01} \right] + \partial_\beta \left[(-i\epsilon - 2i(\chi_1 - \chi_2)\beta - i\delta_c\beta + \kappa\beta/2)P_{01} \right]$$
$$+ i4(\chi_1 - \chi_2/2)\alpha\beta P_{01} - 2\gamma_2 P_{10} + i\tilde{\omega}P_{01}$$
$$\tag{2.157}$$

Here we assumed identical qbuits, hence $\chi_i^{(j)} = \chi_i^{(k)} = \chi_i$ and $\gamma_i^{(j)} = \gamma_i^{(k)} = \gamma_i$. These equations can be solved with the Ansatz

$$P_{11} = \delta^{(2)} \left[\alpha - \alpha_1(t) \right] \delta^{(2)} \left[\beta - \alpha_1^*(t) \right] \tag{2.158}$$

$$P_{00} = \delta^{(2)} \left[\alpha - \alpha_0(t) \right] \delta^{(2)} \left[\beta - \alpha_0^*(t) \right] \tag{2.159}$$

$$P_{10} = a_{10}(t)\delta^{(2)} \left[\alpha - \alpha_1(t) \right] \delta^{(2)} \left[\beta - \alpha_0^*(t) \right] \tag{2.160}$$

$$P_{01} = a_{01}(t)\delta^{(2)} \left[\alpha - \alpha_0(t) \right] \delta^{(2)} \left[\beta - \alpha_1^*(t) \right] \tag{2.161}$$

which yields the following differential equations:

$$\dot{\alpha}_1 = -i\epsilon - i\left(\delta_c + \chi_1 - \chi_2 - i\kappa/2\right)\alpha_1 \tag{2.162}$$

$$\dot{\alpha}_0 = -i\epsilon - i\left(\delta_c - \chi_1 - i\kappa/2\right)\alpha_0 \tag{2.163}$$

$$\dot{a}_{10} = -i(\tilde{\omega} - i2\gamma_2)a_{10} - i4(\chi_1 - \chi_2/2)\alpha_1\alpha_0^* a_{10} \tag{2.164}$$

$$\dot{a}_{01} = i(\tilde{\omega} + i2\gamma_2)a_{01} + i4(\chi_1 - \chi_2/2)\alpha_0\alpha_1^* a_{01}. \tag{2.165}$$

In this equation system we see the phase difference with which the two states $|\alpha_0\rangle$ and α_1 oscillate, which leads to an effective dephasing. The differential equations for α_i and a_{ij} can easily be solved and lead to the time evolution of the density matrix (2.86) we used in Sec 8.3.2 to calculate the respective dephasing rate

Chapter III

Adiabatic Quantum Computing

Adiabatic quantum computing (AQC) is an alternative form of quantum computing. In contrast to the circuit model, where the computation is encoded into a series of unitary quantum gates, adiabatic quantum computing incorporates the solution of the problem in the ground state of some final system Hamiltonian. The main principle is to evolve the system over time, from an easily preparable ground state of some Hamilonian, to the ground state of the desired Hamiltonian. The solution of the problem is encoded in the ground state of the desired Hamiltonian. If this evolution is slow enough, the adiabatic theorem ensures that the system stays in the instantaneous ground state. AQC is also known to be universal as shown by Aharonov et al. in 2004 [107]. In this chapter we present two concepts whose realization would yield an advantage for AQC. On the one hand a measurement scheme which allows for a fast readout of flux qubits in the persistent current basis at the flux degeneracy point and on the other hand a coupling scheme that produces four body local interactions.

9 Introduction to AQC

First we give a brief introduction into AQC. We explain the basic principles behind it and present an algorithm which shows a provable quantum speedup over classical computing. For further informations we refer the reader to the broad literature available on AQC, where especially the review of Albash and Lidar [108] gives a nice and complete overview. Note that in this chapter we change notation to $\hat{X}, \hat{Y}, \hat{Z}$ for the Pauli spin matrices, since it is more common in the context of AQC.

9.1 General Concepts

9.1.1 The adiabatic theorem

The main principle behind AQC is the adiabatic theorem which makes a statement about the time evolution of a quantum state depending on the time interval on which the dynamics happen. It states that if the dynamics are slow enough, an initial ground state does not get excited during the evolution. Various modifications which can be interpreted as an application of the adiabatic theorem where used in the history of physics, where the most popular one is probably the Born-Oppenheimer approximation [109]. However, the first mathematically rigorous proof of the adiabatic theorem was given by Kato in 1950 [110]. The aidabatic approximation is stated compactly by Albash and Lidar as follows [108]:

The adiabatic theorem states, roughly, that for a system initially prepared in the ground state $|\epsilon_0\rangle$ (or another eigenstate) of a time dependent Hamiltonian $H(t)$ with the time evolution governed by the Schrödinger equation

$$i\frac{\partial |\Psi(t)\rangle}{\partial t} = H(t) |\Psi(t)\rangle$$

(with $\hbar$ set to 1), will approximately keep the instantaneous ground state (or other eigenstate) $|\epsilon_0(t)\rangle$ of $H(t)$, provided that $H(t)$ varies "sufficiently slowly".

The bottleneck of this statement is the term *sufficiently slow*, which is not a rigorous statement. Kato quantified what this restrictions on the time scale of the system dynamics mathematically means. We will give a approximate bound on the time scale here.

Lets assume that $|\epsilon_j(t)\rangle$ with $j = 0, 1, \ldots$ is the set of eigenstates of $H(t)$ with ordered eigenenergies $\epsilon_j(t)$ ($\epsilon_j(t) \leq \epsilon_{j+1}(t)$). The simplest formulation of the adiabatic theorem than assures that if we prepare the system initially in the eigenstate $|\epsilon_j(0)\rangle$ it will remain in the same time evolved eigenstate $|\epsilon_j(t)\rangle$ for all times t if the following condition is satisfied:

$$\max_{t\in[0,t_f]} \frac{|\langle\epsilon_i|\partial_t H|\epsilon_j\rangle|}{|\epsilon_i - \epsilon_j|^2} \ll 1 \qquad \forall i \neq j, \tag{3.1}$$

where t_f denotes the final time of the evolution. In AQC the time evolution happens in the ground state, because the ground state is stable against relaxation. Therefore it is useful to define the energy gap between ground and first excited state $\Delta(t) = \epsilon_1(t) - \epsilon_0(t)$. The adiabatic condition is in this context often given by $t_f \gg 1/\Delta_{\min}$, with minimal gap $\Delta_{\min} = \min_t \Delta(t)$.

One can criticize that the given condition no longer ensures the dynamics assumed in the adiabatic approximation if the system includes a separate, independent time scale [111] (e.g. an oscillatory driving term). Therefore more rigorous statements were made over the years, on the one hand treating different time scales more carefully

[112] and on the other hand giving tighter bounds [108, 113, 114, 115, 116, 117, 118]. However, for the purposes of this thesis the above version of the adiabatic theorem is sufficient and we refer the reader to the cited literature for the more rigorous versions.

9.1.2 General Hamiltonian

As mentioned before, in AQC the solution to the computational problem is encoded in the ground state of a Hamiltonian $\hat{H}_1$, which in general can be extremely complex. This Hamiltonian is often referred to as the target Hamiltonian. Since the ground state of $\hat{H}_1$ is not known before the computation, one needs an initial state in which one prepares the system. Here one chooses an easily preparable state, which yields the ground state of the starting Hamiltonian $\hat{H}_0$. After preparing the system in the ground state of $\hat{H}_0$, one slowly evolves the system from $\hat{H}_0$ to $\hat{H}_1$. The corresponding time-dependent Hamiltonian has the form

$$\hat{H}(s) = (1-s)\hat{H}_0 + s\hat{H}_1, \tag{3.2}$$

with the normalized time parameter $s = t/t_f$ evolving from 0 to 1. The time evolution has to be chosen such that the adiabatic theorem is applicable, meaning qualitatively the minimal gap of $\hat{H}(s)$ is large compared to the total evolution time t_f. As predicted by the adiabatic theorem this condition ensures that the system stays in the ground state of $\hat{H}(s)$ during the whole evolution, meaning it ends up with the ground state of $\hat{H}_1$. Since the ground state of $\hat{H}_1$ encodes the wanted solution, the computational problem is solved. In general one can choose more complicated schedules to optimize the computation time, as we will see in Sec. 9.2

In a more visible manner, one can think about AQC as a particle starting in the minimum of an easy energy landscape with just one minimum to a much more complicated landscape with a lot of local minima where the particle can get stuck. Classically the only way to get out of a local minimum is through thermal excitation whereas in a quantum mechanical system the particle is also able to tunnel through the barriers in the energy landscape as illustrated in Fig. 3.1. This picture visualizes the advantage of quantum annealing over the classical counterpart. However, a bare tunneling process gets the particle out of the minimum, but does not change the energy, hence it is necessary to include some relaxation into the system (for more details see [119, 120]). Also tunneling is rather inefficient if the system is stuck in a broad minimum, such that at some points in the annealing schedule it is beneficial to pause and let thermalization happen. These considerations lead to the investigation of features in newer AQC realization like pausing, quenching and reverse annealing [121, 122, 123, 124, 125, 126]. We refer the reader to the cited literature for more information.

A typical example which is naturally suitable for AQC is finding the ground state of the Ising spin Hamiltonian. Here the target Hamiltonian is given by [127]

$$\hat{H}_1 = -\frac{1}{2}\sum_{i=1}^{N} h_i \hat{Z}_i + \sum_{<i,j>} J_{ij}\hat{Z}_i\hat{Z}_j, \tag{3.3}$$

which describes N interacting spin 1/2 particles. In (3.3) the interaction is restricted to nearest neighbors, which is often a good approximation for realistic systems. As a
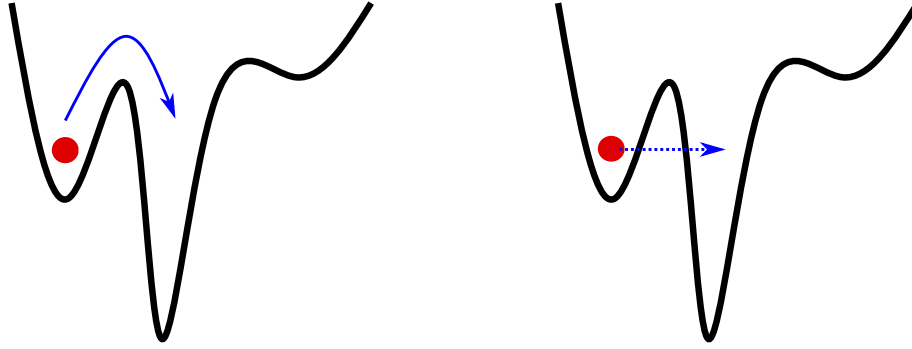
FIGURE 3.1: *Difference between classical annealing and quantum annealing. In the classical case (left) the particle needs thermal excitation to get out of the local minimum, whereas in the quantum case it can tunnel through the barrier (right)*

starting Hamiltonian the usual choice is

$$\hat{H}_0 = \Delta \sum_{i=1}^{N} \hat{X}_i, \tag{3.4}$$

whose unique ground state is easy to prepare (e.g by applying a strong transversal field). The Ising spin Hamiltonian can be used to describe interesting phenomena in spin-like systems, e.g. quantum phase transitions [124, 125]. However, finding the ground state of (3.3) can be very difficult. In fact the Ising spin glass problem can be shown to be NP-complete for dimensions larger than two [128]. Therefore finding the ground state of (3.3) provides a natural way to compare AQC with classical computers.

Adiabatic quantum computing is also shown to be equivalent to the circuit model and is therefore able to solve as a universal quantum computer [7]. However, for the realization of universality one has to engineer interactions which do not naturally appear in physical systems, either non-pairwise or non-stoquastic interactions. Non-pairwise interactions are the main interest of Sec. 11, where we present a novel flux qubit coupling device which induces four local interactions. Non-stoquastic interactions are described by interaction Hamiltonians with non-negative off diagonal elements (e.g. $J\hat{X}_i\hat{X}_j$, with $J > 0$) and are also hard to engineer in physical systems [129, 130, 131]. In principle one has to couple the system using the conjugated quantum variable (e.g. in flux qubit couple charge degree of freedom). One experimental realization of such non-stoquastic interactions using a special coupling architecture can be found in [132]. Additionally there exists a theoretical proposal for an alternative flux qubit which intrinsically delivers the possibility of nonstoquastic interactions [133].

9.2 Grover Search Algorithm

The Grover algorithm was the first proposed algorithm for a quantum computer with provable quantum speedup. Originally the algorithm is designed for the circuit model, but we will show in this section that it has an AQC equivalent which is able to achieve the same speedup.

The problem tackled by the Grover algorithm is to search an unsorted database of N items for a specific marked codeword m in as few queries as possible. One can quantify the problem using binary codewords.

Formally one is allowed to call a function $f : \{0,1\}^n \mapsto \{0,1\}$, where the function satisfies $f(m) = 1$ and $f(x) = 0 \; \forall x \neq m$. Note that the number of possible items is given by 2^n. The goal is to find an algorithm, that identifies the marked item m with as few queries of the database as possible. One can easily show that the best classical method to find the marked item scales linearly with N.

To implement the problem on an AQC, we need a final Hamiltonian. We choose $\hat{H}_1 = \mathbb{1} - |m\rangle \langle m|$, where m in this case is the binary representation of the marked codeword. One can easily check that $|m\rangle$ is the ground sate of $\hat{H}_1$ with eigenvalue 0. All other computational basis states give eigenvalue 1. Note that it is not a priori clear how to implement $\hat{H}_1$ in an actual physical system. In the circuit version of Grover's algorithm one assumes an oracle in form of a unitary operator, which initializes some function f. The Hamiltonian can be seen as the counterpart of this oracle in the adiabatic version. Clearly the motivation behind such oracle based algorithms are rather proof of principle than actually application based. However, $\hat{H}_1$ fulfills the requirements for the final Hamiltonian. As initial Hamiltonian, we use $\hat{H}_0 = \mathbb{1} - |\phi\rangle \langle \phi|$. The state $|\phi\rangle$ denotes the state

$$|\phi\rangle = \frac{1}{\sqrt{N}} \sum_{i=0}^{N-1} |i\rangle, \tag{3.5}$$

which is assumed to be easy preparable (see discussion about Ising model in Sec. 9.1.2). Now that we defined the initial and final Hamiltonian we can write down the time-dependent system Hamiltonian

$$\hat{H}(s) = (1-s)\hat{H}_0 + s\hat{H}_1 \tag{3.6}$$
$$= (1-s)(\mathbb{1} - |\phi\rangle \langle \phi|) + s(\mathbb{1} - |m\rangle \langle m|)). \tag{3.7}$$

If the system initially is in the ground state of $\hat{H}_0$, which is given by $|\phi\rangle$, the time evolution during the anneal happens in a two dimensionl subspace with basis $|m\rangle$ and $|m^T\rangle$. By representing $\hat{H}(s)$ in this two dimensional subspace it is easy to calculate the eigenvalues in this subspace and the gap between the two eigenvalues in this subspace is given by (for more details see [108])

$$\Delta(s) = \sqrt{(1-2s)^2 + \frac{4}{N}s(1-s)}. \tag{3.8}$$

The time scaling of the algorithm is determined by the minimal gap, which occurs at $s = 1/2$:

$$\Delta_{\min} = 2^{-n/2}. \tag{3.9}$$

Using a rigorous version of the adiabatic condition, which e.g. can be found in [108], this leads to the following condition on the annealing time

$$t_f \gg \frac{3}{\Delta_{\min}^2}, \tag{3.10}$$

which unfortunately states that the scaling of the adiabatic Grover algorithm is the same as the classical counterpart. However, here we used a linear time schedule. In general one can choose more complicated time schedules of the form

$$\hat{H}(s) = (1 - A(s))\hat{H}_0 + A(s)\hat{H}_1, \tag{3.11}$$

with $A(0) = 0$ and $A(s) = 1$. Eq. Since we did not observe any speedup so far, it may be necessary to improve the time schedule. Note that the minimal gap appears at $s = 1/2$, so it would make sense to choose a time schedule which slows down closed to this area and speeds up away from the minimal gap. One possible choice is given by the differential equation

$$\partial_s A = c\Delta_p[A(s)], \quad p, c > 0. \tag{3.12}$$

For this schedule and the choice $p = 2$ the scaling can be shown to be

$$t_f \gg k \times \sqrt{N}, \tag{3.13}$$

where k is a constant factor. Therefore the adiabatic version of the Grover algorithm shows the same scaling as the circuit based version, yielding a provable quantum speedup of both. Since the circuit model and AQC are known to be universal, this is also the best scaling possible with an adiabatic algorithm.

10 Flux Qubit Readout at Arbitrary Bias Points

Common flux qubit readout schemes are qubit dominated, meaning they measure in the energy eigenbasis of the qubit. For various applications meausrements in a basis different from the actual energy eigenbasis are required. Here we present an indirect measurement protocol, which is detector dominated instead of qubit dominated, yielding a projective measurement in the persistent current basis for arbitrary bias points. We show that with our setup it is possible to perform a quantum nondemolition measurement (QND) in the persistent current basis at all flux bias points with fidelities reaching almost 100%.

10.1 Introduction

The measurement postulate is fundamental in the formulation of quantum mechanics [6]. To obtain information about the quantum state of a closed system one needs to employ an interaction with an additional readout system (meter). The required interaction affects the measured system, resulting in a change of its quantum state. It is possible to design this interaction, such that the measured observable is an integral of motion during the readout process, and is thus minimally affected by the detector. This is called a quantum non-demolition (QND) measurement. QND measurements enable repeated measurements having the same outcome, to exceed the standard quantum limit [19].

In the field of quantum information QND measurements play an important role in various aspects like e.g. error correction [16, 134], initialization by measurement [135] or one way quantum computing [136]. A promising candidate for the real world implementation of quantum computers are superconducting qubits [26]. Here QND measurements have been experimentally realized for different qubit realizations [48, 101, 137, 138, 139, 140, 141, 142]. The main principle behind all these measurements is to couple the qubit to a far-detuned resonator and measure the state-dependent frequency of the resonator using homodyne/heterodyne measurements [20, 53] or a photodetector [21, 54, 70, 143]. These so called dispersive measurements can be performed in the linear [21, 52] and the nonlinear regime [91, 101, 138, 139, 141, 143]. Dispersive measurements as well as most measurements performed in the field of quantum information are qubit dominated. In these schemes the qubit basis is the preferred basis due to the weak coupling, leading to the fact that the qubit basis determines the measured observable.

Flux qubits [34] are especially interesting for the field of quantum annealing [7, 108, 112, 144, 145, 146] where the intrinsic possibility for inductive coupling and the rather large anharmonicity deliver a big advantage. However, for flux qubits QND measurements in the persistent current basis have only been performed far away from the flux degeneracy point. At the degeneracy point the expectation value of the persistent current, i.e the measurement variable is zero for the qubit energy eigenstates. Measurement in the energy eigenbasis at the degeneracy point is possible by coupling the qubit transversely to a resonator, leading to a measurement of the quantum inductance [147, 148, 149, 150], or by using a more complicated scheme based on modulated coupling [151]. On the other hand flux qubits are most robust against environmental effects (e.g 1/f noise) at the degeneracy point, making it very attractive

---

to operate at this point. The possibility to measure during the anneal process in the persistent current basis, without first driving the qubit far away from the degeneracy point would yield huge benefits, e.g. avoid quenches in annealing schedules, which limit success probability [108, 124, 125].

Also state tomography would benefit from such a readout scheme, since here one has to be able to perform measurement in canonically conjugated bases [152, 153]. Flux qubit readout at the degeneracy point by measuring of the state dependent Josephson inductance corresponds to a measurement in the qubit energy eigenbasis, whereas readout at this point in the persistent current basis yields a measurement in the conjugated basis. Therefore a combination of both serves the possibility for effective state tomography of single and multiple qubit states.

Here we present a method to measure the state of a flux qubit for arbitrary biases at and far away from the degeneracy point, both QND and with a high measurement fidelity. In contrast to existing protocols, here the measurement is always performed in the persistent current basis as opposed to the energy eigenbasis for $\Delta \neq 0$. The presented indirect measurement protocol includes a quantum probe in between the flux qubit we want to read out and the actual readout resonator (e.g. SQUID), namely a compound Josephson junction SQUID (cjj-SQUID) [154, 155, 156]. The most characteristic feature of the cjj-SQUID is the possibility to control the tunneling matrix element with an external flux. Taking advantage of this feature, we can map the qubit states to pointer states of the cjj-SQUID and after that decrease the tunneling rate. With this strategy we effectively decouple the qubit from the probe before performing the macroscopic readout, a necessary condition for QND measurements. In contrast to usual measurement schemes here we present a detector dominated measurement by choosing strong or even ultrastrong coupling between the qubit and the quantum probe, such that the measured observable is determined by the eigenbasis of the operator coupled to the probe. Here this is the persistent current basis, as opposed to the qubit energy eigenbasis.

We show that our measurement protocol enables a QND measurement at the degeneracy point and can achieve measurement fidelities of almost 100% with no unnecessary backaction on the qubit. The results are obtained by quantizing the measurement circuit and by studying the underlying dynamics numerically as well as analytically.

10.2 Circuit and Hamiltonian

Standard flux qubit readout in the persistent current basis is usually realized by coupling a SQUID to the flux qubit to be measured [35, 137, 138, 139, 140, 157, 158, 159]. The two main strategies in use are to operate the SQUID as a switching device [160] or as an oscillator with state dependent frequency [137, 138, 161]. In our scheme we include an additional ingredient, the cjj-SQUID, [155] in between the qubit and the actual readout SQUID, realizing the quantum probe of our indirect measurement. This cjj-SQUID is a superconducting loop interrupted by a smaller dc-SQUID. It behaves like an rf-SQUID with a tunable critical current, serving as a coupler that can be tuned from off to ultrastrong (coupling rate higher than qubit frequency) using an external flux bias. This device has various uses in quantum information mostly as an advanced flux qubit design [154, 155, 156]. The Hamiltonian of the cjj-SQUID can be written down using circuit quantization [156]

$$\hat{H}_{\text{cjj}} = \frac{\phi_0^2}{L} \left(4\xi^2 \frac{\hat{q}^2}{2} + \frac{(\hat{\varphi} - \tilde{\varphi}_x)^2}{2} - \beta_{\text{cjj}}(\Phi_c) \cos \hat{\varphi} \right), \tag{3.14}$$
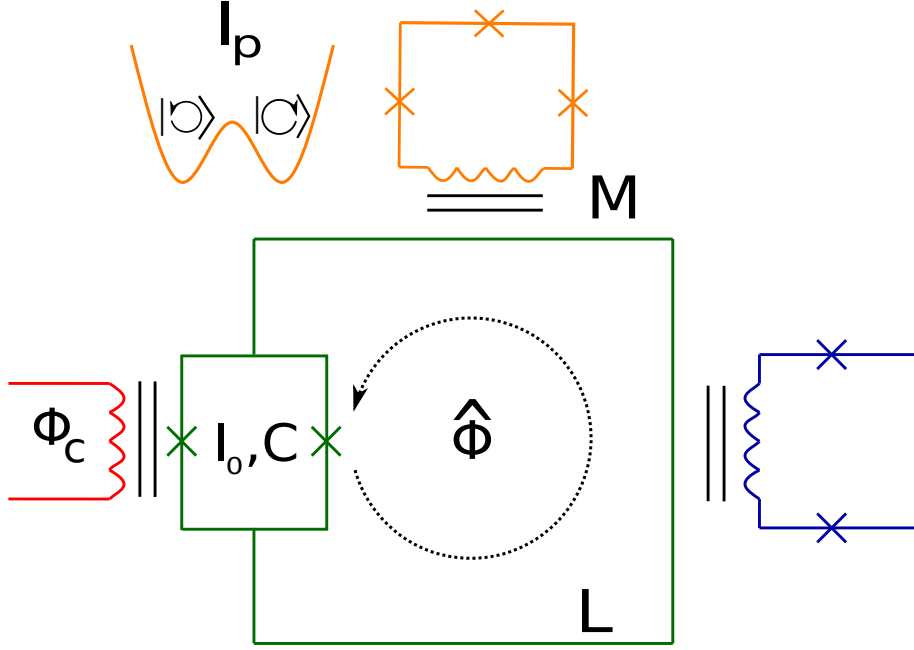
FIGURE 3.2: *Circuit for the measurement protocol. The qubit (yellow) is coupled to the large SQUID loop of the quantum probe, here the cjj-SQUID (green). To measure the persistent current of the cjj-SQUID in the end, the large loop is coupled to an additional flux readout loop (blue). To control the barrier of the cjj-SQUID an external control flux Φ_c (red) is applied to the small SQUID loop.*

where $\xi = e/\phi_0 \sqrt{L/C_\Sigma}$, and $\phi_0 = \Phi_0/2\pi$, with mutual inductance M, persistent current I_p, inductance of the large cjj-SQUID loop L, sum of the two junction capacitances C_Σ and Φ_0 the flux quantum. The quantum variable of the probe is the average phase of the junctions $\hat{\varphi} = 2\pi\hat{\Phi}/\Phi_0$ and $\hat{q}$ is the conjugated variable. As shown in Fig. 3.2 two different fluxes can be applied to the two loops of the cjj-SQUID. Here Φ_c denotes the flux applied to the small SQUID loop and $\varphi_x = \Phi_x/\phi_0$ the flux applied to the larger loop. Using Φ_c it is possible to tune the barrier of the cjj-SQUIDs double well potential up and down. The actual flux dependence on Φ_c is $\beta_{\text{cjj}}(\Phi_c) = (2I_0 L/\phi_0)\cos(\Phi_c/2\phi_0)$ [156], with critical current of the SQUID junctions I_0.

The external flux on the larger loop on the other hand determines the tilt of the double well potential, hence we couple the flux qubit we want to read out to this loop. The coupling is realized via a mutual inductance M of the qubit and the cjj-SQUID incorporates an additional contribution $(MI_p/\phi_0)\hat{Z}$ to φ_x. I_p denotes the persistent current of the qubit. Since this contribution depends on the Pauli spin operator $\hat{Z}$ in the persistent current basis of the qubit, the effect on the cjj-SQUID depends on the qubit state. The overall system Hamiltonian can then be written as

$$\hat{H} = \frac{\Phi_0^2}{L}\left(4\xi^2\frac{\hat{q}^2}{2} + \frac{\left(\hat{\varphi} - \frac{MI_p}{\phi_0}\hat{Z} - \tilde{\varphi}_x\right)^2}{2} - \beta_{\text{cjj}}(\Phi_c)\cos\hat{\varphi}\right) + \hat{H}_{\text{qb}}. \qquad (3.15)$$
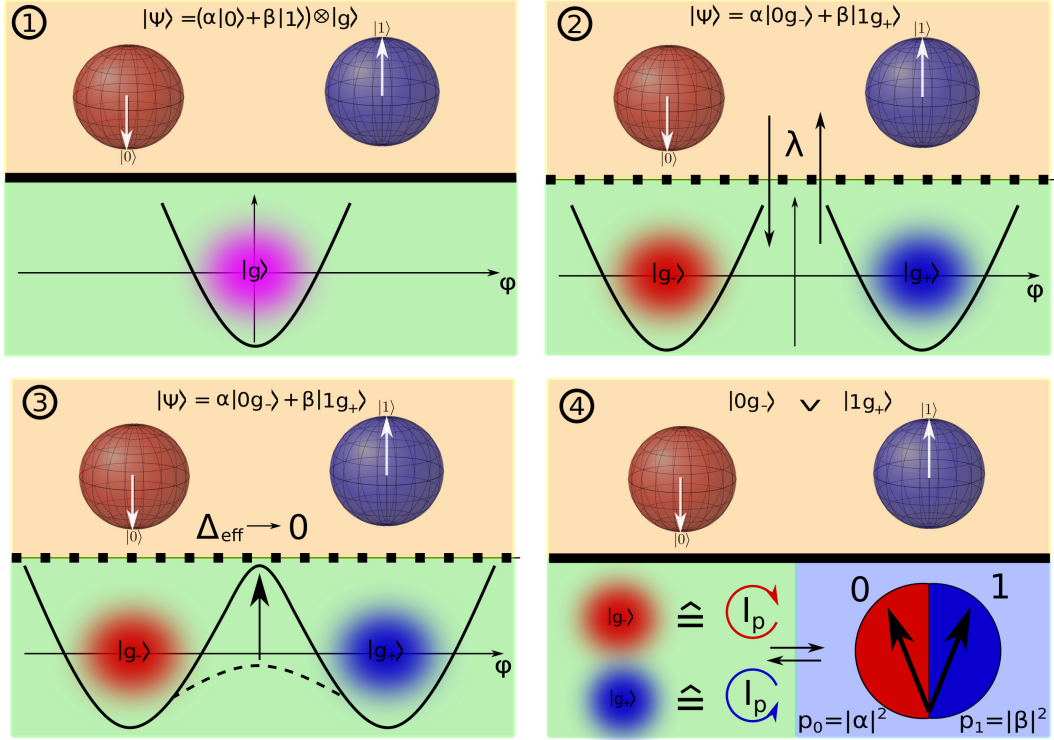
FIGURE 3.3: *Principle of the measurement scheme. Color code analog to Fig 3.2. 1.) Initialization (upper left): The qubit (yellow) and the cjj-SQUID (green) initial state are prepared. 2.) Premeasurement (upper right): The coupling between the qubit and the cjj-SQUID is ramped up, such that the qubit states get entangled with corresponding pointer states. 3.) Effective decoupling (lower left): The c-jj SQUID potential is turned from a single well to a double well potential. 4.) Readout (lower right): The cjj-SQUID persistent current state is read out with an additional flux readout device (e.g rf-SQUID).*

The Hamiltonian of the flux qubit can be expressed in the two-level approximation using Pauli spin operators

$$\hat{H}_{\text{qb}} = \frac{\epsilon}{2}\hat{Z} + \frac{\Delta}{2}\hat{X} \tag{3.16}$$

Eq. 3.16 is written down in the persistent current basis of the qubit $\{|\circlearrowleft\rangle, |\circlearrowright\rangle\}$. The energy spacing between these states is given by $\epsilon = I_p(\Phi_{\text{QB}} - \Phi_0/2)$ and Δ denotes the tunneling energy . Especially at the degeneracy point $\epsilon = 0$, the energy eigenstates of the qubit are orthogonal to the persistent current states and are given by the symmetric and antisymmetric superpositions of the ladder.

To later ensure symmetric pointer states, we bias the cjj-SQUID at the symmetry point $\tilde{\varphi}_x = \pi$, yielding

$$\hat{H} = \frac{\phi_0^2}{L}\left(4\xi^2\frac{\hat{q}^2}{2} + \frac{\hat{\varphi}^2}{2} + \beta_{\text{cjj}}(\Phi_c)\cos\hat{\varphi} - \frac{g}{\sqrt{\xi}}\hat{\varphi}\hat{Z}\right) + \hat{H}_{\text{qb}}, \tag{3.17}$$

where $g = \sqrt{\xi}MI_p/\phi_0$ denotes the coupling parameter and with $\varphi_x = \tilde{\varphi}_x + \pi$. The Hamiltonian can be divided into the bare qubit part, the quadratic part of the cjj-SQUID, the tunable nonlinear part of the cjj-SQUID and transverse coupling part.

For further calculations we will write $\hat{\varphi}$ as

$$\hat{\varphi} = \frac{1}{\sqrt{2m\Omega}}(\hat{a}^\dagger + \hat{a}), \tag{3.18}$$

with effective mass $m = 1/(2\xi)^2$, $\Omega = 2\xi$ and where $\hat{a}$ and $\hat{a}^\dagger$ are the annihilation and creation operator of the quadratic part of the cjj-SQUID Hamiltonian, satisfying the commutation relation $\left[\hat{a}, \hat{a}^\dagger\right] = \mathbb{1}$. Using Eq. (3.18) the Hamiltonian can be expressed by ladder operators

$$\hat{H} = E_L \left[\Omega \hat{a}^\dagger \hat{a} + m\Omega^2 \beta_{\text{cjj}}(\Phi_c) \cos\left(\frac{1}{\sqrt{2m\Omega}}(\hat{a}^\dagger + \hat{a})\right) - g(\hat{a}^\dagger + \hat{a})\hat{Z} \right] + \hat{H}_{\text{qb}}, \tag{3.19}$$

with inductive energy of the large coupler loop $E_L = \phi_0^2/L$.

10.3 Measurement Protocol

In this section we present the protocol of the measurement. Here we qualitatively discuss the main steps and the basic idea behind them, before we quantitatively analyze the whole procedure in the next section. It has four main steps, the initialization, the premeasurement, the effective decoupling and the readout of the probe. The whole measurement protocol is visualized in Fig. 3.3.

In the initialization step we prepare the qubit in an arbitrary initial state $\alpha \left|\circlearrowleft\right\rangle + \beta \left|\circlearrowright\right\rangle$ and the cjj-SQUID in the ground state $\left|g\right\rangle$. Here the qubit and the probe are decoupled and the screening parameter β_{cjj} of the cjj-SQUID is zero, meaning it is described by a harmonic oscillator potential.

After initialization we start the premeasurement. For this, we turn on the coupling between the qubit and the cjj-SQUID. During this step, the external bias on the small coupler loop is still chosen as $\Phi_c = \Phi_0/2$, such that the barrier is zero and the cjj-SQUID potential is purely quadratic. By turning on the coupling between the cjj-SQUID and the qubit, an entangled state between the qubit and the pointer states of the probe is created, performing the premeasurement. Since the cjj-SQUID starts in the ground state $\left|g\right\rangle$, the coupling term shifts the center of the Gaussian distribution of the phase. For zero coupling, the cjj-SQUID state is centered around $\langle\hat{\varphi}\rangle = 0$, until the coupling shifts the mean value to $\langle\hat{\varphi}\rangle = \pm\varphi_p \left\langle\hat{Z}\right\rangle$. Note that the shift depends on the qubit state as follows from (3.17).

Here we want to choose parameters such that the interaction does not induce any excitation of the cjj-SQUIDs initial ground state, meaning we require a perfect adiabatic time evolution of the system [162]

$$(\alpha \left|\circlearrowleft\right\rangle + \beta \left|\circlearrowright\right\rangle) \left|g\right\rangle \longrightarrow \alpha_{\text{eff}} \left|\circlearrowleft, g_-\right\rangle + \beta_{\text{eff}} \left|\circlearrowright, g_+\right\rangle, \tag{3.20}$$

where $\left|g\right\rangle$ is the coupler ground state centered around zero and $\left|g_\pm\right\rangle$ are the corresponding displaced ground states centered around $\pm\varphi_p$. α_{eff} and β_{eff} include the time evolution under the bare qubit Hamiltonian [162], i.e. if the system is not in an eigenstate of $\hat{H}_{\text{qb}}$. The effective coupling energy Δ_{eff} gets rescaled due to the interaction with the cjj-SQUID [162]. To make the adiabatic approximation applicable, the timescale of the interaction must satisfy the adiabatic theorem [110]. This yields the condition

$$\max_t \frac{\dot{g}(t)}{\sqrt{\xi}} \ll \Omega. \tag{3.21}$$

Violating this condition leads to transitions between cjj-SQUID pointer states which destroys the distinguishability, since there is no longer a clear map between direction of persistent current and qubit state.

Besides the fact that we want the measurement to discriminate between the qubit states, we additionally want the measurement to be QND. A QND measurement is achieved, when the measured observable is an integral of motion during the measurement, meaning successive measurements of the qubit yield the same result [14]. This is achieved by the third step of our protocol, the effective decoupling. Especially in the case $\epsilon \ll \Delta$, the non-commuting part of the system and the interaction Hamiltonian is crucial, hence severe backaction would appear during the macroscopic readout of the probe. Therefore in the effective decoupling step, we use the external bias Φ_c to ramp the barrier of the cjj-SQUID potential from a single well harmonic potential to a double well potential with a high barrier. This exponentially decreases the effective coupling energy Δ_{eff}, resulting in a reduction of the non-commuting part. With this we freeze the dynamics of the qubit, yielding an effective decoupling of the qubit and the probe, necessary for a QND measurement [14]. Note that the tuning of the barrier also has to be adiabatically on the cjj-SQUID timescale to again avoid excitations to higher modes, such that we have to modify condition (3.21) and include the time derivative of the screening parameter $\beta_{cjj}(t)$

$$\max_t \left[\frac{\dot{g}(t)}{\sqrt{\xi}}, \dot{\beta}_{cjj}(t) \right] \ll \Omega. \tag{3.22}$$

In a last step we can measure the probe state using the additional persistent current readout with indicating almost no backaction, since $\Delta_{\text{eff}}(T) \approx 0$

Because of the non-commuting nature of the interaction and the system Hamiltonian, there is also a backaction induced during the premeasurement and the effective decoupling. Therefore one needs to perform these two steps fast with respect to the characteristic qubit timescale

$$T\sqrt{\Delta^2 + \epsilon^2} \ll h, \tag{3.23}$$

where T denotes the overall time of the measurement protocol. However, this general condition is to strict in our case. On the one hand the whole point of the third step is to decrease the effective decoupling rate to almost zero and on the other hand in the case $\epsilon \gg \Delta$ the backaction is negligible, since system and interaction Hamiltonian almost commute. Including these facts, the QND condition for our system is given by

$$\int_0^T \Delta_{\text{eff}}(t)\mathrm{d}t \ll h, \tag{3.24}$$

Note that the effective tunneling rate is time dependent, since it is influenced by the interaction with the probe. Because of the entanglement of the pointer states and the qubit states after the premeasurement, a high barrier of the cjj-SQUID potential also frustrates a tunneling between the qubit states. This leads to the fact that 3.24 is even satisfied for measurement times larger than the qubits characteristic time, as we will see in the next section.

Before the macroscopic readout of the probe state, it is important that the two pointer states are statistically distinguishable, meaning that the maximal coupling strength $g_{\text{max}} = g(T)$ needs to be chosen such that the condition [163]

$$\langle \varphi(T) \rangle_1 - \langle \varphi(T) \rangle_0 \geq 2 \left[\sigma_1(T) + \sigma_0(T) \right], \tag{3.25}$$

is satisfied at the end. Here $\langle\varphi(T)\rangle_i$ is the expectation value of the pointer state if the qubit is in state i and $\sigma(T)_i$ is the respective standard deviation. Both are taken at the end of the measurement protocol.

The distinguishability criterion gives a lower bound for the necessary maximal coupling strength $g_{\max}$. The measurement fidelity is limited by the overlap of the pointer states and transitions between different cjj-SQUID states during the interaction process. Therefore the most general expression for the measurement fidelity is given by

$$\mathcal{F}_{\text{meas}} = \frac{\mathcal{F}_{\circlearrowleft} + \mathcal{F}_{\circlearrowright}}{2}, \tag{3.26}$$

where $\mathcal{F}_i$ denotes the probability to get the right measurement result if the qubit is prepare in the energy eigenstate $|i\rangle$. The state fidelities read

$$\mathcal{F}_i = \int_{a_i}^{b_i} \left(\left|\langle\varphi, \circlearrowright |\hat{U}(t)|g, i\rangle\right|^2 + \left|\langle\varphi, \circlearrowleft |\hat{U}(t)|g, i\rangle\right|^2 \right) \mathrm{d}\varphi \tag{3.27}$$

where $i \in \{\circlearrowleft, \circlearrowright\}$, $\hat{U}(t)$ is the time evolution operator which describes the time dynamics of the measurement process and $\{a_{\circlearrowright}, b_{\circlearrowright}\} = \{-\infty, 0\}$, $\{a_{\circlearrowleft}, b_{\circlearrowleft}\} = \{0, \infty\}$.

10.4 Numerical Results

We want to quantitatively study the measurement protocol. The most important point here is to quantify the right time scales and system parameters to obtain high measurement fidelities and prove the QNDness of the protocol. In Sec. 10.3 the premeasurement and decoupling of the protocol were discussed successively, but to get a faster measurement and reduce backaction we will combine these two steps. This means we turn on the coupling and in the same time period we ramp the barrier of the cjj-SQUID potential. In an experiment this would give the opportunity to control the coupling and the cjj-SQUID with one control flux.

10.4.1 measurement fidelity

To numerically study the measurement fidelity we use the harmonic oscillator representation of the cjj-SQUID (3.19). With this representation we can write down the Hamiltonian in harmonic oscillator modes of the cjj-SQUID using the formula

$$\langle n|\mathrm{e}^{ir(\hat{a}^\dagger+\hat{a})}|m\rangle = i^{3n+m}\sqrt{\frac{n!}{m!}}\mathrm{e}^{-\frac{r^2}{2}}r^{n-k}L_n^{(n-m)}(r^2), \tag{3.28}$$

where $L_n^{(n-m)}(r^2)$ refers to the generalized Laguerre polynomial. Here we truncate the Hamiltonian after 100 oscillator states. Since $g(t)$ and $\beta_{\text{cjj}}(t)$ are time dependent we have to solve a time dependent Schrödinger equation. For this we use a standard Runge-Kutta method.

In Fig. 3.4 we see the probability distribution of the cjj-SQUID after performance of the measurement protocol. We use the simplest possible time schedule, where we tune up the coupling and the barrier linearly. Here the maximal value of the coupling is $\lambda_{\max} = 1$, the maximal nonlinearity $\beta_{cjj}^{\max} = \beta_{cjj}(T)$ is 2 and $\xi = 0.1$. The overall time interval in which we ramp up both parameters is chosen to be $10/\Omega$ and the coupler frequency is ten times the qubit frequency. We perform the measurement protocol at the flux degeneracy point $\epsilon = 0$ and choose as initial state the qubit ground state $|0\rangle = (|\circlearrowleft\rangle + |\circlearrowright\rangle)/\sqrt{2}$. Fig. 3.4 shows that the pointer states resolve the qubit states
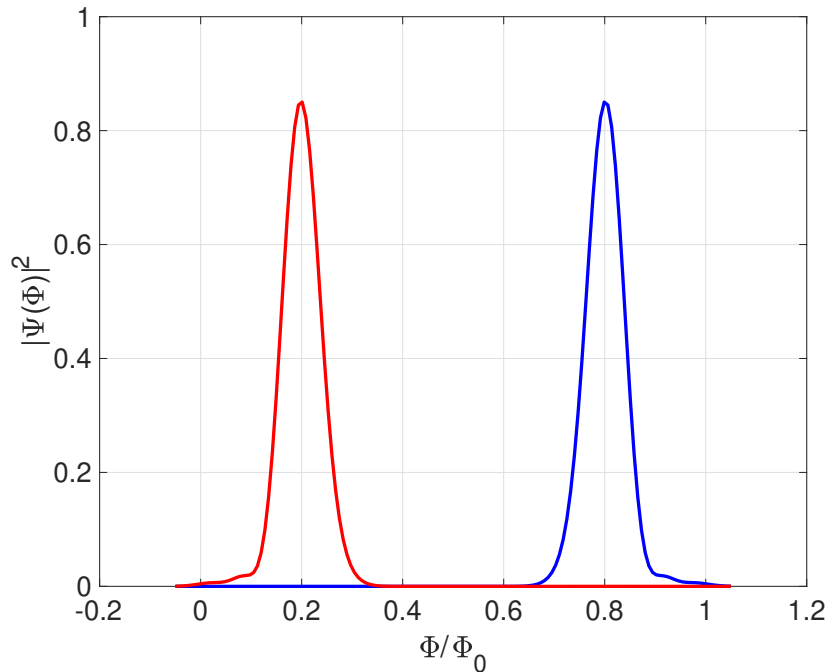
FIGURE 3.4: *Probability distribution for a linear time schedule with $\lambda(T) = 1$ and $\beta_{cjj}(T) = 2$ as final values. As initial state we choose the qubit ground state $|0\rangle = 1/\sqrt{2}(|\circlearrowleft\rangle + |\circlearrowright\rangle)$.*

accurately. The projection of the final combined state into the qubit persistent current state $|\circlearrowleft\rangle$ and $|\circlearrowright\rangle$ shows a probability distribution peaked around a value $-\varphi_p$ and φ, respectively. Therefore the two different qubit states correspond to two different persistent current directions of the cjj-SQUID (clockwise and counterclockwise). The two distributions show the respective shifted cjj-SQUID ground state where the shift depends on the qubit state.

The different persistent current states of the cjj-SQUID can be measured with the additional readout device in a next step, yielding a projective measurement of the flux qubit in the persistent current basis. As can be seen in Fig. 3.4 the overlap of the two distributions is almost zero promising a good measurement fidelity. For the parameters of Fig. 3.4 the measurement fidelity is $1 - 10^{-5}$.

To quantify the dependence on the maximal coupling strength, we show the measurement fidelity dependence on g_{max} for different values of ξ in Fig 3.5. We see that the measurement fidelity strongly increases for larger values of g_{max} until it reaches a plateau at fidelity 1. For smaller ξ, the fidelities are lower. Even though the ultrastrong coupling regime is accessible in flux qubit architectures ([42, 164, 165]), it is more feasible to work in the strong coupling regime. However, even in this regime which corresponds to $g_{max}/\Omega \approx 0.1$, the measurement fidelities are quite high. E.g. for $\xi = 0.1$ we reach a fidelity of 80.8%. Since the coupling is weaker the interaction time needed for a resolving premeasurement is also longer, hence it is supporting to choose longer measurement times. For an increased measurement time of $T = 50/\Omega$ the fidelity for $\xi = 0.1$ and $g = 0.1$ already reaches 95%. Here we model measurement at the flux degeneracy point, but the protocol leads to high fidelities for $\epsilon \neq 0$ as well, e.g. for the same parameters as in Fig. 3.4 but for the case $\epsilon = \Delta$, a measurement fidelity of $1 - 10^{-5}$ is achievable.
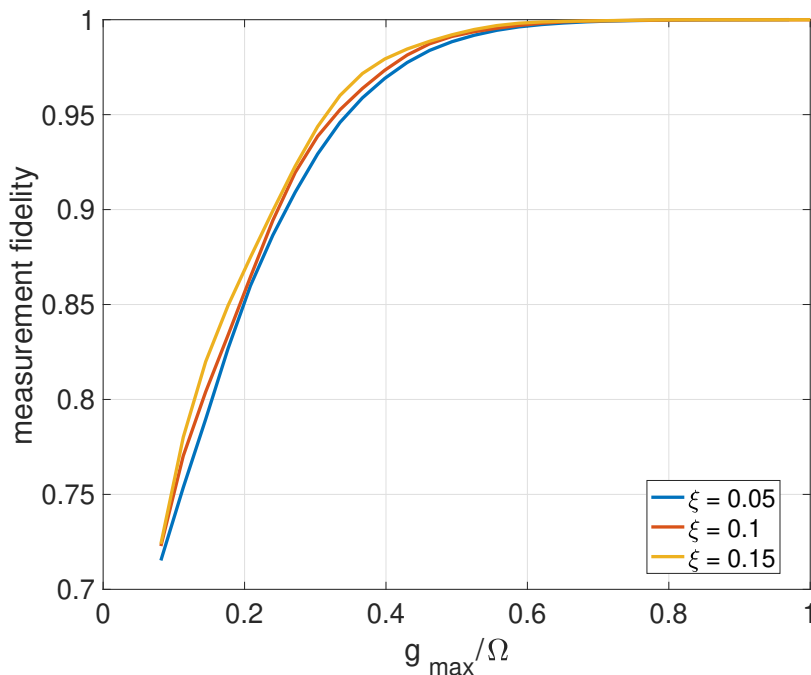
FIGURE 3.5: *Dependence of the fidelity on the maximum coupling strength g_{max} for different values of ξ.*

Here we model measurement at the flux degeneracy point, but the protocol also works analogously for $\epsilon \neq 0$.

10.4.2 Backaction

In the last section we showed that the measurement protocol works and that we can achieve high fidelities. However, usual dispersive measurement protocols in the persistent current basis fail to be QND at $\epsilon \ll \Delta$, since the interaction Hamiltonian does not commute with the system Hamiltonian. This implies a change of qubit population in the measurement basis, mostly because of the rather slow nature of dispersive measurements. Here the measurement is performed relatively fast with respect to the qubit frequencies and the non-commuting part is discriminated exponentially by turning on the barrier, hence we expect the backaction having a less crucial effect. In this section we want to confirm this by numerically tracking the time dynamics of the density matrix elements of the qubit.

In Fig. 3.6, the time evolution of the density matrix elements for the initial qubit state $|0\rangle = 1/\sqrt{2}(|\circlearrowleft\rangle + |\circlearrowright\rangle)$ and at the degeneracy point $\epsilon = 0$ is studied. The parameters are the same as in Fig. 3.4. We see that the measurement induces a strong dephasing in the measurement basis (persistent current basis). This is what one expects since entangling the qubit with the respective pointer states means transferring qubit information to the probe system ([68] or [14]). The fact that the measurement induces a dephasing in the persistent current basis proves that the meausrement protocol does not measure in the energy eigenbasis of the qubit, but in the eigenbasis of the probe. The diagonal elements on the other hand stay constant, meaning the population in the persistent current basis is conserved (note again that energy eigenstates are the two equal superposition states of the persistent current).

As mentioned before, a way to determine the QNDness of a measurement is the comparison of repeated successive readouts. Since here the measurement observable is the persistent current, we have to study the decay of the corresponding states $|\circlearrowright\rangle, |\circlearrowleft\rangle$ of the qubit to check for QNDness. The QNDness in our system can be quantified as the probability that the qubits initial persistent current state is preserved after premeasurement, irrespective of the measurement outcome [14, 140], yielding the expression

$$\mathcal{F}_{\text{QND}} = \frac{\langle \circlearrowright |\hat{U}_{\text{QB}}(t)| \circlearrowright\rangle + \langle \circlearrowleft |\hat{U}_{\text{QB}}(t)| \circlearrowleft\rangle}{2}, \tag{3.29}$$

where $\hat{U}_{\text{QB}}(t) = \text{Tr}_{cjj}\{\hat{U}(t)\}$ denotes the effective time evolution of the qubit during the premeasurement. As mentioned, to ensure QNDness of the protocol we ramp up the barrier and effectively discriminate the time evolution of the system, which leads to the fact that only in the beginning of the protocol the qubit suffers a small rotation. For the parameters of Fig. 3.4, expression (3.29) can be determined numerically and yields a QND fidelity of $\mathcal{F}_{\text{QND}} = 99.6\%$. We are optimistic that further optimization strategies (e.g. find optimized schedules) could lead to even better results, yielding a perfect QND measurement with a measurement fidelity of almost 100%.

Note that we do not include environmental effects here which would set an upper limit for the QNDness. The most crucial one in flux qubit architectures is usually $1/f$ flux noise [166, 167]. Flux noise changes the value of ϵ such that the chosen initial state $|0\rangle$ is no longer an eigenstate of the Hamiltonian resulting in a small change of the qubit population over time. Additionally flux noise changes the symmetry character of the potentials such that the minima of the cjj-SQUID potential are no longer symmetric. This does not change the QNDness per se but the overall measurement fidelity.

10.5   Analytical Fidelity

In this section we will analytically describe the setup presented in Sec I, especially giving approximate expression for the success probability.

Since we are in the regime where the energy of the cjj-SQUID is larger than the energy of the qubit , we consider the qubit Hamiltonian as the perturbation of the system

$$V = \frac{\epsilon}{2}\hat{Z} + \frac{\Delta}{2}\hat{X}. \tag{3.30}$$

As shown in Sec. 10.2, the phase-charge space representation of the unperturbed Hamiltonian reads

$$H_0(t) = E_L \left(\frac{\hat{q}^2}{2m} + m\Omega^2 \frac{\varphi^2}{2} + m\Omega^2 \beta_c(t) \cos(\varphi) - m\Omega^2 \lambda(t) Z\varphi \right). \tag{3.31}$$

with $\lambda(t) = g(t)/\sqrt{\xi}$. Without the cosine term, this yields a shifted harmonic oscillator where the shift depends on the qubit state. To include the contribution of the non-harmonic cosine part, we will approximate the potential around its minimum. It is

$$U'(\varphi)/E_L = m\Omega^2\varphi - m\Omega^2\beta_c(t)\sin(\varphi) - m\Omega^2\lambda(t)Z. \tag{3.32}$$
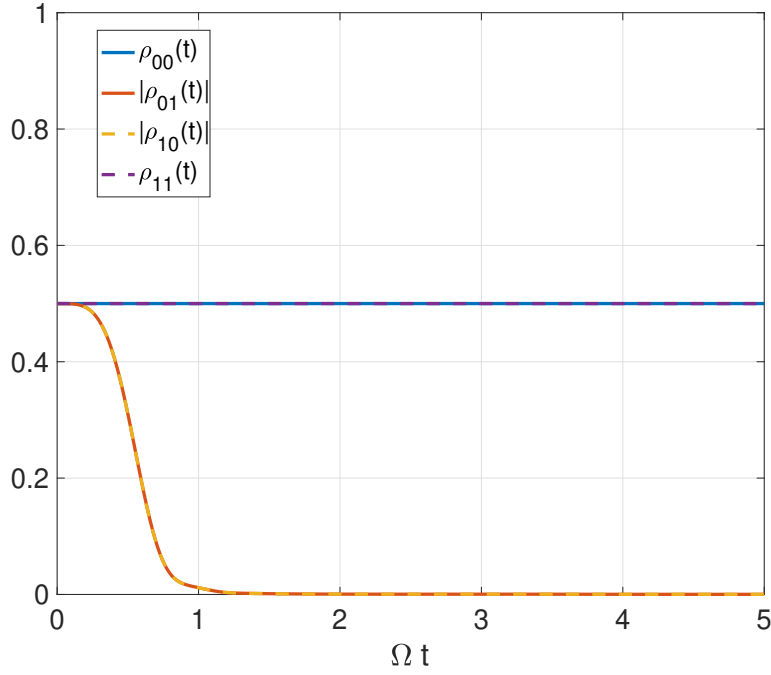
FIGURE 3.6: *Time evolution of the density matrix elements of the qubit subspace for the initial state $|0\rangle$.*

The condition $U'(\varphi) = 0$ leads to an equation for the potential minimum, depending on Z. Since $\langle Z \rangle = \pm 1$ the position is symmetric for the two qubit states

$$\varphi_{\pm}(t) = \pm\varphi_p(t), \tag{3.33}$$

where $\varphi_p(t)$ denotes the positive valued minimum. The effective potential up to second order then reads

$$U(\varphi)/E_L \approx \varphi_p(t)Z + \frac{m\Omega^2}{2}\left[1 - \beta_c(t)\cos(\varphi_p(t))\right]\left(\varphi - \varphi_p(t)\hat{Z}\right)^2 \tag{3.34}$$

$$= \varphi_p(t)Z + \frac{m\tilde{\Omega}(t)^2}{2}\varphi^2 - m\tilde{\Omega}(t)^2\varphi_p(t)\varphi\hat{Z}. \tag{3.35}$$

with time dependent frequency $\tilde{\Omega}(t) = \Omega\sqrt{1 - \beta_c(t)\cos(\varphi_p)}$. Note that the frequency does not depend on the qubit state, because of the symmetry of the cosine. This leads to the effective Hamiltonian

$$\hat{H}(t) \approx E_L\left(\frac{q^2}{2m} + \frac{m\tilde{\Omega}(t)^2\varphi^2}{2} - m\tilde{\Omega}(t)^2\varphi_p(t)\varphi\hat{Z}\right) \tag{3.36}$$

$$= E_L\left(\tilde{\Omega}(t)a^{\dagger}a - \tilde{\Omega}(t)\sqrt{\frac{m\tilde{\Omega}(t)}{2}}\varphi_p(t)(a^{\dagger} + a)\hat{Z}\right). \tag{3.37}$$

The last part implies a qubit dependent shift of the harmonic oscillator, such that we can diagonalize this Hamiltonian with the displacement operator

$$\tilde{\hat{H}}(t) = D^\dagger(\tilde{\varphi}_p(t)\hat{Z})HD(\tilde{\varphi}_p(t)\hat{Z}) \tag{3.38}$$

$$= E_L\tilde{\Omega}(t)a^\dagger a \tag{3.39}$$

where $\tilde{\varphi}_p(t) = \varphi_p(t)\sqrt{m\tilde{\Omega}(t)/2}$. The time dependence of the transformation induces an additional inertia term. As mentioned before, we choose time scales to be diabatic on the qubit and adiabatic on the coupler time scale. Hence in zeroth order we assume the SQUID state to follow the minimum adiabatically, so we ignore the term proportional to $\dot{\tilde{\varphi}}_p$ (inertia part) for now. Additionally we ignore the contribution arising from the zeroth order of the Taylor expansion, since it only acts as a correction of the bare qubit Hamiltonian (for more details see Sec. 10.6).

We can directly write down the solution to (3.39) in the position space which is a Gaussian distribution around the minimum of the potential

$$\varphi(t) = \left(2\pi\sigma(t)^2\right)^{-1/4}\mathrm{e}^{-\left(\frac{\varphi-\varphi_p\langle\hat{Z}\rangle(t)}{2\sigma(t)}\right)^2+ip_0\varphi}\left|\varphi\right\rangle, \tag{3.40}$$

with standard deviation $\sigma(t) = 1/\sqrt{2m\tilde{\Omega}(t)}$ and p_0 being the average momentum. Let us now assume the qubit starts in a superposition state and the cjj-SQUID in its ground state (centered around $\varphi = 0$). The time evolution reads

$$(\alpha\left|\circlearrowleft\right\rangle + \beta\left|\circlearrowright\right\rangle)\left|g\right\rangle \xrightarrow{\hat{U}} \alpha_{\text{eff}}\left|\circlearrowleft, \varphi_-(t)\right\rangle + \beta_{\text{eff}}\left|\circlearrowright, \varphi_+(t)\right\rangle, \tag{3.41}$$

with

$$\left|\varphi_\pm(t)\right\rangle = \left(2\pi\sigma(t)^2\right)^{-1/4}\mathrm{e}^{-\left(\frac{\varphi\mp\varphi_p}{2\sigma(t)}\right)^2+ip_0\varphi}\left|\varphi\right\rangle \tag{3.42}$$

and where α_{eff} and β_{eff} include the time evolution induced by the bare qubit Hamiltonian, i.e when the state is not an eigenstate (see [162] for more details). We are especially interested in the probabilities for the SQUID to be in the left or right persistent current state, depending on the qubit state. E.g. the probability to get the right measurement result if the qubit starts in the $\left|\circlearrowleft\right\rangle$ state (equivalent to $\mathcal{F}_\circlearrowleft$ of the main text) is given by

$$\mathcal{F}_\circlearrowleft(t) = \frac{1}{\sqrt{2\pi\sigma(t)^2}}\int_{-\infty}^0 \mathrm{e}^{-\frac{(\varphi+\varphi_p)^2}{2\sigma(t)^2}}\,\mathrm{d}\varphi \tag{3.43}$$

$$= \Phi\left(\frac{\varphi_p(T)}{\sigma(t)}\right), \tag{3.44}$$

with $\Phi(x) = \frac{1}{\sqrt{2\pi}}\int_{-\infty}^x \mathrm{e}^{-\frac{1}{2}t^2}\mathrm{d}t$ denoting the normal cumulative distribution function. In the same manner we can write down the probability to get the right measurement result when the qubit starts in state $\left|1\right\rangle$

$$\mathcal{F}_\circlearrowright(T) = -\Phi\left(-\frac{\varphi_p(T)}{\sigma(T)}\right). \tag{3.45}$$
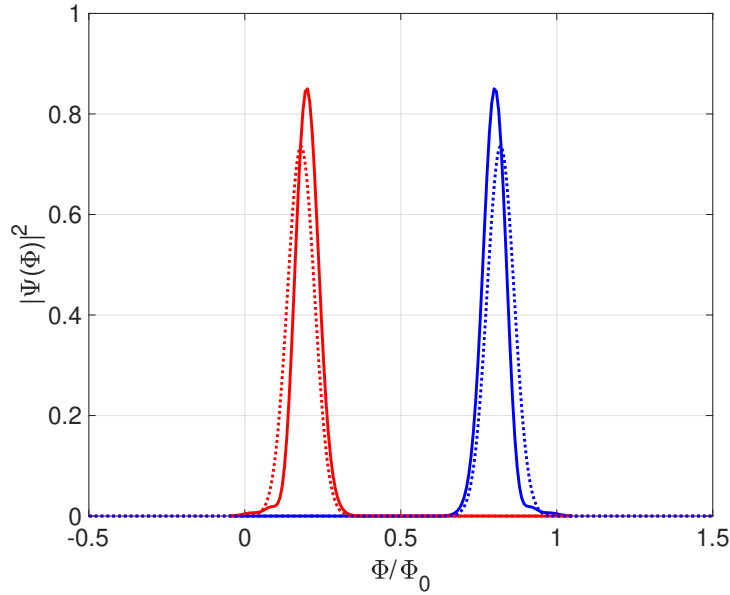
FIGURE 3.7: *Comparison of the numerical (solid) and analytical (dotted) results for the same parameters as in the main text.*

This expressions correspond to the two contributions that appear in the expression for the fidelity hence, in the Gaussian approximation, $\mathcal{F}$ can be written as

$$\mathcal{F}(T) = \Phi\left(\frac{\varphi_p(T)}{\sigma(T)}\right), \tag{3.46}$$

where we used the fact that $\Phi(t)$ is an odd function. Fortunately, Gaussians are among the simplest special functions and the expectation value is completely determined by the standard deviation $\sigma(T)$, hence the fidelity is fully determined by $\sigma(T)$ and φ_p. This fact can be used to e.g. put a lower bound on the measurement fidelity and determine the corresponding system parameter intervals to reach this fidelity. Here the main parameters that can be varied are g_{max} and β_{cjj}^{max}. One could also optimize the schedule, i.e. find an optimal pulse for the time dynamics of the coupling and the barrier to optimize both, measurement fidelity and backaction. However, this would yield an optimal control problem and can be tracked by future work. A lower bound for the respective system parameters is given by the distinguishability condition (Eq. (3.25) of Sec. 10.3). Since the distributions are symmetric, the condition has the simplified form

$$\varphi_p(T) \geq 2\sigma(T). \tag{3.47}$$

In Fig. 3.7 the distribution of the cjj-SQUID state (depending on the qubit state) is compared to the numerical results. We basically see what we expect. The two results coincide very well, but there are corrections coming from the higher order potential terms. Since we model the double well potential of the cjj-SQUID with two harmonic potentials, the two numerical expectation values are slightly shifted compared away from the barrier in the middle and they also do not show the slight asymmetric behavior on the left of the distributions.

All in all this section shows, that the intuitive picture of the system dynamics, we

gave when we described the measurement scheme in the main text can be quantified with the given analytical results assuming an adiabatic time evolution of the pointer states. Since the analytical results also give a good agreement with the numerics, the adiabatic approximation is satisfied for the chosen time scale, avoiding any induced transitions between different cjj-SQUID states.

10.6   Analytical Backaction

Here we will try to analytically approximate the backaction of the measurement on the qubit. For this we first transform the Hamiltonian into an interaction frame (i.e the displaced oscillator frame) such that we can write down the time dependent Hamiltonian as a tensor sum of two dimensional matrices (within the adiabatic approximation). Then we can study the time evolution of the qubit subspace density matrix and with this make statements about the backaction.

As shown in 10.5 we can diagonalize H_0 approximately by applying the displacement operator

$$\hat{D}(\tilde{\varphi}_p(t)\hat{Z}). \tag{3.48}$$

This leads to a diagonal Hamiltonian plus an additional inertia term coming from the time dependence of the transformation and a correction of the bare qubit Hamiltonian arising from the fact that the two minima of the tilted double well potential are not at the same potential level

$$\tilde{H}_0 = \tilde{\Omega}(t)\hat{a}^\dagger a - i\dot{\tilde{\varphi}}_p(t)(a^\dagger - a) - \lambda\varphi(t)\hat{Z} \tag{3.49}$$

$$= \tilde{\Omega}(t)\hat{a}^\dagger a - i\dot{\tilde{\varphi}}(t)p_0\left(\dot{\varphi}_p + \frac{1}{4}\frac{\dot{\tilde{\Omega}}(t)}{\tilde{\Omega}(t)}\varphi_p(t)\right) - \lambda\varphi(t)\hat{Z} \tag{3.50}$$

where $p_0(t)$ is the average momentum at time t, which can be rewritten using the correspondence principle $p_0(t) = m\dot{\varphi}_p(t)$. The last term arises from the zeroth order of the Taylor expansion. Hence we need to take into account two correction terms. We also have to check what is the effect of the transformation on the bare qubit Hamiltonian

$$\tilde{V} = \hat{D}^\dagger(\tilde{\varphi}_p(t)\hat{Z})\left[\epsilon\hat{Z} + \Delta\hat{X}\right]\hat{D}(\tilde{\varphi}_p(t)\hat{Z}) \tag{3.51}$$

$$\approx \epsilon\hat{Z} + \Delta\hat{X} + 2\tilde{\varphi}_p(t)p_0(t)\Delta\hat{\sigma}_y, \tag{3.52}$$

where we only kept the first order term of the Baker-Campbell-Hausdorff formula. Since we assume $\Delta \ll \Omega$, the σ_y correction is assumed to be rather small compared to the Z correction arising from $\hat{\tilde{H}}_0$, hence will be ignored in the following. With this we can write the Hamiltonian in the transformed basis as a tensor sum

$$\tilde{H}(t) = \oplus_{N=0}^\infty \tilde{H}_N(t), \tag{3.53}$$

where $H_N(t)$ is the Hamiltonian in the N excitation subspace $\{|0, N_-\rangle, |1, N_+\rangle\}$ and has the form

$$\tilde{H}_N(t) = \begin{pmatrix} N\tilde{\Omega}(t) - \gamma(t) & \frac{\Delta}{2}\langle N_+|N_-\rangle \\ \frac{\Delta}{2}\langle N_-|N_+\rangle & N\tilde{\Omega} + \gamma(t) \end{pmatrix}, \tag{3.54}$$

with

$$\gamma(t) = -m \left(\dot{\varphi}_p(t)^2 + \frac{1}{4} \frac{\dot{\tilde{\Omega}}(t)}{\tilde{\Omega}(t)} \varphi_p(t) + \lambda \varphi_p(t) \right) \tag{3.55}$$

$$\tilde{\Omega}_N(t) = N \tilde{\Omega}(t). \tag{3.56}$$

Here $|N_\pm\rangle$ refer to the N excitation states of a shifted harmonic oscillator, where the sign depends on the qubit state and the shift is given by (3.33) (for more details on the shifted harmonic oscillator we refer to [168]). Here we assumed an adiabatic time evolution of the cjj-SQUID dynsmics by setting $\langle N_\pm | M_\pm \rangle = \langle N_\pm | M_\mp \rangle = 0$ if $N \neq M$. Note that $\langle N_+ | N_- \rangle = \langle N_- | N_+ \rangle$, hence $\tilde{H}(t)$ is hermitian as demanded. The overlapp between the shifted oscillator vacuum states is given by [168]

$$\langle 0_- | 0_+ \rangle = \mathrm{e}^{-\varphi_p^2/2} \tag{3.57}$$

Because of the block diagonal structure of the Hamiltonian, we can also write down the time propagator $U(t)$ in a block diagonal structure. For this we need the following expressions

$$U_N(t) = \exp \left(i\mathcal{T} \int_0^t \mathrm{d}t' \tilde{H}_N(t') \right), \tag{3.58}$$

with the time ordering operator $\mathcal{T}$. Since we assume the time evolution to be diabatic on the qubit subspace and we are interested in the dominating backaction effects, we use first order Magnus expansion to calculate the time propagators $V_N(t)$

$$V_N(t) \approx \exp \left(i \int_0^t \mathrm{d}t' H(t') \right). \tag{3.59}$$

Defining the parameters $\Gamma(t) = \int_0^t \mathrm{d}t' \gamma(t')$ and $\tilde{\Delta}_N(t) = \Delta/2 \int_0^t \mathrm{d}t' \langle N_+ | N_- \rangle (t')$ the propagator of the N excitation subspace can be written as

$$V_N(t) = \mathrm{e}^{i \int_0^t \mathrm{d}t' \tilde{\Omega}_N(t')} \begin{pmatrix} \cos\left(\Theta(t)\right) - iK_N(t)\sin\left(\Theta(t)\right) & iK_N(t)\sin\left(\Theta(t)\right) \\ iK_N(t)\sin\left(\Theta(t)\right) & \cos\left(\Theta(t)\right) + iK_N(t)\sin\left(\Theta(t)\right) \end{pmatrix}. \tag{3.60}$$

with

$$\Theta(t) = \sqrt{\Gamma(t)^2 + \tilde{\Delta}(t)^2} \tag{3.61}$$

$$K_N(t) = \frac{\tilde{\Delta}_N(t)}{\sqrt{\Gamma(t)^2 + \tilde{\Delta}(t)^2}} \tag{3.62}$$

Since the backaction tends to be strongest at the degeneracy point, we choose $\epsilon = 0$ in the following, such that $H_{\mathrm{QB}} = \frac{\Delta}{2} X$. We want to study the time evolution of an arbitrary qubit state, when we prepare the SQUID in the ground state ($\langle N \rangle = 0$), leading to the following density matrix at $t = 0$

$$\hat{\rho}(0) = \begin{pmatrix} |\alpha|^2 & \alpha\beta^* \\ \alpha^*\beta & |\beta|^2 \end{pmatrix} \otimes |0\rangle \langle 0| \tag{3.63}$$

The time evolution of this state can then be calculated using $V(t)$. We are especially interested in the density matrix of the qubit at time t, so we trace out the cjj-SQUID

degrees of freedom

$$\rho^{\mathrm{QB}}(t) = \mathrm{Tr}_{\mathrm{cjj}}\{\rho(t)\} \tag{3.64}$$

$$\begin{aligned}
&= |\alpha(t)|^2 \left|\circlearrowleft\right\rangle \left\langle\circlearrowleft\right| + \alpha(t)\beta^*(t) \left|\circlearrowleft\right\rangle \left\langle\circlearrowleft\right| \mathrm{e}^{-\tilde{\varphi}_p(t)^2} \\
&\quad + \alpha^*(t)\beta(t) \left|\circlearrowright\right\rangle \left\langle\circlearrowleft\right| \mathrm{e}^{-\tilde{\varphi}_p(t)^2} + |\beta(t)|^2 \left|\circlearrowright\right\rangle \left\langle\circlearrowright\right|
\end{aligned} \tag{3.65}$$

Here we clearly see the measurement induced dephasing appearing as an exponential damping of the off diagonal elements, depending on the displacement between the two pointer states. The time evolution of the prefactors α and β can be calculated using the time propagator. For the initial state $|0\rangle$, it is $\alpha = 1/\sqrt{2}$ and $\beta = 1/\sqrt{2}$ leading to the density matrix entries

$$\rho_{00}^{\mathrm{QB}}(t) = \frac{1}{2}\left(1 - 2\frac{\tilde{\Delta}_0(t)\Gamma(t)}{\kappa(t)}\sin^2\kappa(t)\right) \tag{3.66}$$

$$\begin{aligned}
\rho_{01}^{\mathrm{QB}}(t) = \frac{1}{2}\Bigg(&1 - 2\frac{\Gamma(t)^2}{\kappa^2(t)}\sin^2\kappa(t) \\
&- 2i\frac{\Gamma(t)}{\kappa(t)}\sin\kappa(t)\cos\kappa(t)\Bigg)\exp\left(-\tilde{\varphi}_p(t)^2\right)
\end{aligned} \tag{3.67}$$

$$\rho_{10}^{\mathrm{QB}}(t) = \left(\rho_{01}^{\mathrm{QB}}(t)\right)^* \tag{3.68}$$

$$\rho_{11}^{\mathrm{QB}}(t) = 1 - \rho_{00}^{\mathrm{QB}}(t), \tag{3.69}$$

where we defined $\kappa(t) = \sqrt{\Delta_0(t)^2 + \Gamma(t)^2}$. In Fig. 3.8 we see the time evolution of the parameters $\Gamma(t)$ and $\tilde{\Delta}(t)$. We see that for $t \mapsto T$, Γ gets much larger than Δ leading the oscillating term of the diagonal elements to go to zero, such that at the end of the measurement process the population is the same as in the beginning, proving the measurement to be QND. The long time behavior of the off diagonal elements are dominated by the measurement induced dephasing, i.e. the exponential part. Therefore the offdiagonal elements completely decay for $t \mapsto T$, what we also see in the numerical results.

However, even though the analytical results predict the right qualitative behavior and the right long time behavior, there are deviations between the analytical and numerical results. E.g. the predicted damped oscillations of the diagonal elements around $1/2$ are not observed in Fig. 3.8. Two main factors limit the validity of the analytics. First we only included the first order of the Magnus expansion, but since T is in the order of the qubit time evolution for the parameters in Fig. 3.6, it is not completely reasonable to assume a diabatic time evolution on the qubit time scale. Hence to get more rigorous results one has to include higher orders of the Magnus expansion. Second, we ignored the contributions coming from the non-commuting character of the interaction and the qubit Hamiltonian. Even though the studied contributions are the leading backaction terms, for T comparable to the qubit time scale, the other contributions also start to matter.

10.7   Conclusion

In conclusion we have presented an indirect measurement protocol to perform fast read out a flux qubit at every bias point in the persistent current basis, with possible measurement fidelities closed to 100%. Further the measurement is also shown to be QND, which increases the possibility for applications in fundamental flux qubit experiments as well as in the perspective of quantum annealing even more. A special
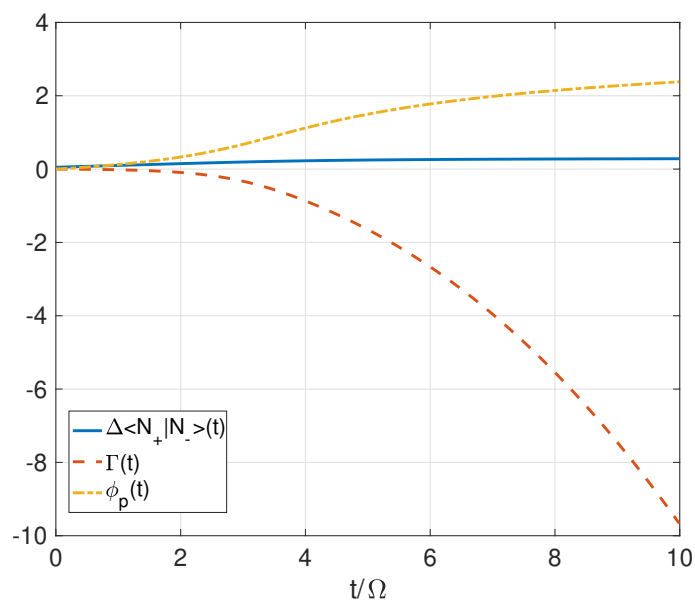
FIGURE 3.8: *Time evolution of the parameters $\tilde{\Delta}(t)$, $\Gamma(t)$ and $\varphi_p(t)$ for the same parameters as in the main text.*

feature is that the readout at the flux degeneracy point is performed in the persistent current basis, being potentially useful in terms of quantum annealing but also for other applications such as quantum state tomography.

11 Non-Pairwise Interactions Induced by Virtual Transitions

The field of quantum information has matured and various protocols implementing a quantum computer are being pursued. Most similar to a classical computer is the circuit model. In 2004 Aharonov et al. showed the equivalence between the circuit model and an AQC, and with this proofed the universality of the latter. However, equivalence with the circuit model requires multi-local interactions, i.e. interaction terms involving more than two subsystems. Natural interactions are only two-local, hence the construction or simulation of higher order couplers is indispensable for a universal AQC. Also four-local interactions serve as a tool for basic research. Here we show that in a specific flux qubit coupler design without ancilla qubits, strong four body interactions are induced by virtual coupler excitations. For specific parameter regimes they are even the leading effect and can be tuned up to the GHz range.

11.1 Introduction

Quantum computers have the potential to lead to an exponentially reduced computation time compared to classical computers for certain problems. One promising candidate for the realization of such a device is an adiabatic quantum computer (AQC), where the computation proceeds from an initial Hamiltonian whose ground state is easy to prepare to the ground state of a final Hamiltonian which encodes the solution of the computational problem, by avoiding excitations [108, 144, 169, 170]. It is now known that an AQC represents a universal quantum computer due to its equivalence with the circuit model [107]. Still, implementing an AQC with verifiable speedup is a difficult task. A big step is to overcome the locality of natural interactions. k local interactions with $k > 2$ are suitable for the effective implementation of various optimization algorithms without using perturbative gadget methods which create overhead [146] and can also be used for effective prime factoring on AQCs [171]. Furthermore, since conventional qubit designs are not feasible to implement non-stoquastic interactions [131, 133], the universality of AQCs is restricted by the condition $k > 2$ [7]. There are embedding schemes that simulate this type of coupling requiring overhead, making it desirable to implement them as natively as possible. On the other hand higher order local interactions are interesting from a fundamental physics point of view, since the only known and proven interaction between more than two particles is found in Efimov states [172, 173].

In this section we propose a specific coupler architecture using flux qubits [34] and prove the existence of non negligible antiferromagnetic four local interactions. There are many proposals to realize higher local interactions, using quantum embedding or ancilla qubits [174, 175, 176]. All of the currently existing ones for $k > 3$ need at least k additional qubits despite the computational ones, to realize k local interactions. Here we present a setup where these basic functions are put into a single coupling device.

11.2 Setup and Hamiltonian

In our setup four qubits are connected via a nonlinear coupler. Here the qubits as well as the nonlinear coupler are realized by an inductive loop with inductivity L_j interrupt
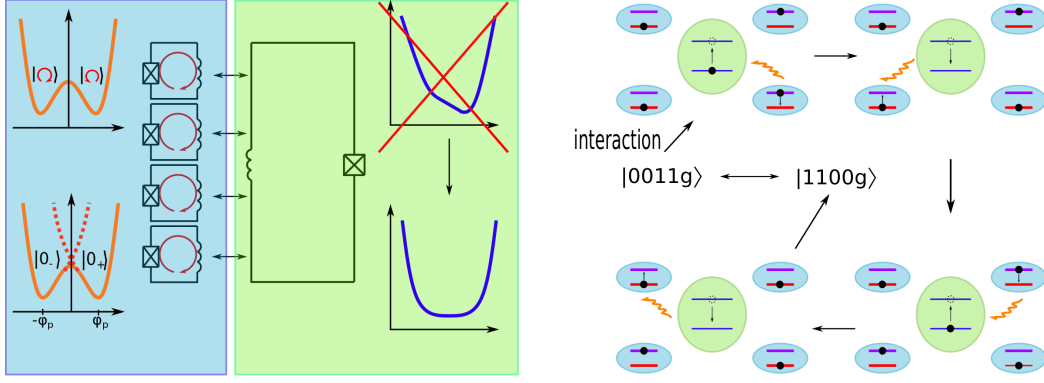

FIGURE 3.9: *Left: Setup of the coupler architecture. Four flux qubits are inductively coupled to an additional flux qubit with higher energy via mutual inductances M_j. This induces an effective coupling between the four qubits. On the left of the qubit we see the qubit double well potential which can be approximated by two shifted harmonic potentials with eigenstates $|0_-\rangle$ and $|0_+\rangle$ corresponding to the persistent current states $|\circlearrowright\rangle$ and $|\circlearrowleft\rangle$ of the qubits. This was done to obtain the projection into the qubit subspace for the analyitcal results. We choose a symmetric coupler potential, to reduce $\hat{Z}$ corrections arising from $\hat{H}_{\mathrm{int}}$ by biasing the coupler at the flux degeneracy point, as shown on the right of the coupler circuit. Right: Visualization of four local interaction induced by virtual coupler transitions. A virtual excitation and annihilation of the coupler leads to an energy transfer between two qubits, hence two such processes can induce effective four local interactions.*

by a Josephson junction with capacity C_j and critical current $I_j^{(c)}$, namely a flux qubit. The junction represents the nonlinear ingredient of the system. Our setup includes four qubits and the coupler (see Fig. 3.9), such that the $j \in \{1, 2, 3, 4, c\}$. A crucial point is that the couplers plasma frequency has to be chosen higher than the qubit ones to avoid transitions between coupler energy levels. The corresponding quantum variables are the respective quantized fluxes of the five loops $\hat{\Phi}_j$. The Hamiltonian describing Fig.3.9 can be obtained by standard circuit quantization. We split the Hamiltonian in three parts [177],

$$\hat{H} = \sum_{j=1}^{4} \hat{H}_j + \hat{H}_c + \hat{H}_{\mathrm{int}}, \tag{3.70}$$

the sum over the bare qubit Hamiltonians $\hat{H}_j$, the bare coupler Hamiltonian $\hat{H}_c$ and the interaction Hamiltonian H_{int}. The qubit and the coupler Hamiltonian include a quadratic potential coming from the LC part and a cosine contribution form the Josephson junction. The strength of the nonlinear term is determined by the ratio between the Josephson energy $E_J = \Phi_0 I_j^{(c)}/2\pi$ and the inductive energy $E_{L_j} = (\Phi_0/2\pi)^2/L_j$, where Φ_0 denotes the flux quantum. More interest should be paid into the interaction part, which arises from an induced external flux from qubit to the coupler and vice versa. Further we operate the coupler as well as the qubits at (or close to) the flux degeneracy point. The different parts of (3.70) can be written

in unitless parameters (for a detailed derivation see Supplement)

$$\hat{H}_j = E_{L_j}\left(4\xi_j^2\frac{\hat{q}_j^2}{2} + (1+\alpha_j^2)\frac{\hat{\varphi}_j^2}{2} + \beta_j\cos(\hat{\varphi}_j)\right) \tag{3.71}$$

$$\hat{H}_c = E_{\tilde{L}_c}\left(4\xi_c^2\frac{\hat{q}_c^2}{2} + \frac{\hat{\varphi}_c^2}{2} + \beta_c\cos(\hat{\varphi}_c)\right) \tag{3.72}$$

$$\hat{H}_{\text{int}} = E_{\tilde{L}_c}\left(\sum_{i<j}^{4}\alpha_i\alpha_j\hat{\varphi}_i\hat{\varphi}_j + \sum_{j=1}^{4}\alpha_j\hat{\varphi}_c\hat{\varphi}_j\right). \tag{3.73}$$

Here we rescaled the coupler impedance $\tilde{L}_c = L_c - \sum_{j=1}^{4}\alpha_j M_j$ to decouple equations, where M_j denotes the mutual inductances of the j-th qubit and $\alpha_j = M_j/L_j$ is the dimensionless mutual inductance. Additionally we defined the parameter $\xi_j = 4\pi Z_j/R_Q$ with characteristic impedance $Z_j = \sqrt{L_j/C_j}$ and the resistance quantum $R_Q = h/e^2$. The quantized phases are given by $\hat{\varphi}_j = (2\pi/\Phi_0)\hat{\Phi}_j + \pi$ and $\hat{q}_j$ is the conjugated quantum variable. Note that we shifted the appearing phases by π leading to the positive sign in front of the cosine part. For coupler and qubits the screening parameter is given by $\beta_c = 2\pi\tilde{L}_c I_c^{(c)}/\Phi_0$ and $\beta_j = 2\pi L_j I_j^{(c)}/\Phi_0$, respectively. Here $I_j^{(c)}$ denotes the critical current of the junctions.

To write down the Hamiltonian in a qubit representation we need to project it into the two-level subspaces with respect to the qubits. A standard way of doing this is to approximate the two wells of the flux qubit potential as shifted harmonic oscillators [168] and interpret the two persistent current states of the qubit as the lowest eigenstates of these symmetrically shifted oscillators [178]. This leads to

$$\hat{\varphi}_j \approx s_j\hat{Z}_j, \tag{3.74}$$

where $\hat{Z}_j$, denotes the Pauli spin operator in the persistent current basis. The factor $s_j \propto \sqrt{1 - \langle 0_+|0_-\rangle}/\sqrt{1 + \langle 0_+|0_-\rangle}$ accounts for the fact that the two shifted ground states are not orthogonal, meaning that s_j would be unity if the overlap of these states was zero (see App. 11.B). Using this notation, the interaction Hamiltonian can be written as

$$\hat{H}_{\text{int}} = E_{\tilde{L}_c}\left((\alpha s)^2\sum_{i,j=1}^{4}\hat{Z}_i\hat{Z}_j + \alpha s\sum_{i=1}^{4}\hat{Z}_i\hat{\varphi}_c\right), \tag{3.75}$$

where we assume identical qubits ($\alpha_i s_i = \alpha s\ \forall i$). The first part induces two body local interactions between the qubits, which we call the direct coupling part and the second part describes the interaction between the qubits and the coupler modes, here referred to as indirect coupling. In commonly used coupler architectures one chooses parameters such that the direct coupling dominates and the two local interactions become strong. Here we want to use a different strategy, where we choose parameters such that the direct interaction part is rather small compared to the indirect coupling part, which gives rise to two but also higher local interactions.

To see how these higher order local interactions are indicated by the indirect interaction part we use a prominent tool from many body physics, the Schrieffer-Wolff transformation (SWT) [179, 180]. We choose the SWT since it produces physically transparent analytical expressions for the induced interactions arising from the indirect coupling part of (3.75). Other than the simplest form of the Born-Oppenheimer approximation [109], it does not rely on the separation of classical frequencies and

effective potentials. It is thus applicable even if transitions are vertical in the coordinate and if in the deep nonlinear regime classical frequencies are ill-defined (worse results for symmetric coupler potential in [181]). The SWT assumes that there are no transitions between different coupler levels, but includes corrections of the low energy subspace due to the existence of higher levels. Hence with the SWT it is possible to perturbatively write down an effective Hamiltonian in this low energy subspace

$$\hat{H}_{\text{eff}} = \hat{P}_0 \hat{H}_0 \hat{P}_0 + \epsilon \hat{P}_0 \hat{V} \hat{P}_0 + \sum_{n=2}^{\infty} \epsilon^n \hat{H}_{\text{eff,n}}. \tag{3.76}$$

where $\hat{H}_0 = \hat{H}_c + \sum_j \hat{H}_j$ is the unperturbed Hamiltonian, $\hat{V} = \hat{H}_{\text{int}}$ is the perturbation, here the interaction, $\epsilon = \alpha s$ is a small parameter and $\hat{P}_0$ projects the Hamiltonian into the low energy subspace (coupler ground state). Every order of the effective Hamiltonian leads to higher order local interactions between the qubits, i.e. in general the k-th perturbative term contains induced interactions up to k-th order. Truncation at fourth order therefore includes fourth order local interactions, such that the effective Hamiltonian has the form

$$\hat{H} \approx \hat{P}_0 \hat{H}_0 \hat{P}_0 + J_2 \sum_{i<j} \hat{Z}_i \hat{Z}_j + J_4 \hat{Z}_1 \hat{Z}_2 \hat{Z}_3 \hat{Z}_4. \tag{3.77}$$

The coupling strengths J_j are given by the prefactors generated by the SWT. Note that J_2 additionally includes direct interactions arising from the second term in (3.76). In general the SW expansion also gives rise to single $\hat{Z}$-rotations and three body terms, but since we choose a symmetric coupler potential these terms are negligible, as we will argue in the following.

The physical principle behind these indirect interactions can be understand with the language of virtual excitations. E.g. the second order describes deexcitation of an excited qubit resulting in a virtual excitation of the coupler, which deexcites again and in turn excites the same or another qubit. Such processes leave the coupler in the ground state, but result in higher order qubit interactions. These virtual processes can be thought to occur only within the Heisenberg energy-time uncertainty. Fourth order processes in the same manner lead to four local interactions as illustrated in Fig. 3.9. For the first and third order, there are no such processes, where the coupler ends up in the ground state, hence they can be neglected in (3.77) (about 2-3 orders of magnitude smaller).

11.3   Analytical Calculation of the SWT

Here we will show how to get an analytical approximation for the SWT by expressing the harmonic part of the coupler using latter operators, and treating the cosine part as a perturbation. For this we truncate the coupler potential after $\mathcal{O}(\hat{\varphi}_c^4)$. The interaction part of the Hamiltonian then reads

$$\hat{H}_{\text{int}}/E_{\tilde{L}_c} = \frac{\beta_c}{24} \hat{\varphi}_c^4 + \alpha^2 \sum_{i<j}^4 \hat{\varphi}_i \hat{\varphi}_j + \alpha \sum_{i=1}^4 \hat{\varphi}_c \hat{\varphi}_i. \tag{3.78}$$

For simplicity we chose identical qubits here. Now we project the Hamiltonian into the qubit subspace (see App. 11.B)

$$\hat{H}_{\text{int}}/E_{\tilde{L}_c} = \frac{\beta_c}{24}\hat{\varphi}_c^4 + \alpha^2 s^2 \sum_{i<j}^{4} \hat{Z}_i \hat{Z}_j + \alpha s \sum_{i=1}^{4} \hat{\phi}_c \hat{Z}_i. \tag{3.79}$$

The harmonic part of the coupler potential

$$\hat{H}_c^{\text{harm}} = 4E_{\tilde{L}_c}\left(\xi_c^2 \frac{\hat{q}_c^2}{2} + \frac{1-\beta_c}{2}\hat{\varphi}_c^2\right) \tag{3.80}$$

can be interpreted as a quantum harmonic oscillator with effective mass $m_c = 1/4E_{\tilde{L}_c}\xi_c^2$ and frequency $\omega_c = 2E_{\tilde{L}_c}\xi_c\sqrt{1-\beta_c}$. Note that the coupler nonlinearity β_c is assumed to be smaller that one, since we want the coupler frequency to be higher than the qubit frequencies. With this we can define the position and momentum operator as

$$\hat{X}_c = \sqrt{m_c\omega_c}\hat{\varphi}_c \tag{3.81}$$

$$\hat{P}_c = \frac{1}{\sqrt{m_c\omega_c}}\hat{q}_c \tag{3.82}$$

and rewrite the harmonic part as $\hat{H}_c^{\text{harm}} = \frac{\omega_c}{2}(\hat{X}_c^2 + \hat{P}_c^2)$. In the same manner we can define the annihilation and creation operator

$$\hat{a}_c = \frac{1}{\sqrt{2}}\left(\hat{X}_c + i\hat{P}_c\right) \tag{3.83}$$

$$\hat{a}_c^\dagger = \frac{1}{\sqrt{2}}\left(\hat{X}_c - i\hat{P}_c\right) \tag{3.84}$$

and rewrite the quantized phase in terms of these operators

$$\hat{\varphi}_c = \frac{1}{\sqrt{2m_c\omega_c}}\left(\hat{a}_c^\dagger + \hat{a}_c\right). \tag{3.85}$$

Using equation (3.85) it is possible to rewrite the interaction Hamiltonian in terms of latter operators

$$\hat{V}_{\text{int}}/E_{\tilde{L}_c} = \frac{\beta_c}{24}\frac{1}{(2m_c\omega_c)^2}\left(\hat{a}_c^\dagger + \hat{a}_c\right)^4 + \alpha^2 s^2 \sum_{i<j}^{4} \hat{Z}_i \hat{Z}_j + \alpha s \sum_{i=1}^{4} \frac{1}{\sqrt{2m_c\omega_c}}\left(\hat{a}_c^\dagger + \hat{a}_c\right)\hat{Z}_i. \tag{3.86}$$

To get a better overview, we divide (3.86) into three parts, the direct qubit-qubit coupling

$$V_{\text{int}}^{QB,QB} = E_{\tilde{L}_c}\alpha^2 s^2 \sum_{i<j} \hat{Z}_i \hat{Z}_j \tag{3.87}$$

the indirect coupling part between qubits and coupler modes

$$V_{\text{int}}^{QB,c} = \frac{E_{\tilde{L}_c}}{\sqrt{2m_c\omega_c}}\alpha^2 s^2 \sum_{i=1}^{4}\left(\hat{a}_c^\dagger + \hat{a}_c\right)\hat{Z}_i, \tag{3.88}$$

and the corrections arising from the fourth order cosine part

$$V_{\mathrm{corr}} = \frac{E_{\tilde{L}_c}\beta_c}{96m_c^2\omega_c^2}\left(\hat{a}_c^\dagger + \hat{a}_c\right)^4. \tag{3.89}$$

To simplify notation even more in the following, we define the appearing prefactors as follows:

$$g^{\mathrm{QB,c}} = \frac{E_{\tilde{L}_c}\alpha s}{\sqrt{m_c\omega_c}} \tag{3.90}$$

$$g^{\mathrm{QB,QB}} = E_{\tilde{L}_c}\alpha^2 s^2 \tag{3.91}$$

$$K_{\mathrm{corr}} = \frac{E_{\tilde{L}_c}\beta_c}{96m_c^2\omega_c^2}. \tag{3.92}$$

As mentioned before, we want to perform the SWT under the assumption that the coupler frequency is higher than the respective qubit frequencies. Basically we have three different perturbative parts (3.87), (3.88) and (3.89), where $\hat{V}_{\mathrm{int}}^{QB,QB}$ just acts on the qubit subspace, hence simply gives a contribution in zeroth order.

In a first step we have to calculate the even and odd contributions of the perturbative parts. Let's define $P_0 = |0\rangle\langle0|$ and $Q_0 = 1 - P_0 = \sum_{n=1}^\infty |n\rangle\langle n|$ as the projection operator on the even and odd subspaces, respectively. Here $|n\rangle$ denotes the n-th Fock state of the harmonic coupler potential. The off-diagonal part of an operator $\hat{X}$ is then given by $\mathcal{O}(\hat{X}) = P_0\hat{X}Q_0 + Q_0\hat{X}P_0$ and the diagonal part by $\mathcal{D}(\hat{X}) = P_0\hat{X}P_0 + Q_0\hat{X}Q_0$. Since $\hat{H}_{\mathrm{int}}^{\mathrm{QB,QB}}$ acts as identity on the coupler subspace it is completely diagonal. The other parts read

$$\mathcal{O}(\hat{a}^\dagger + \hat{a}) = \eta_{01}^+ \tag{3.93}$$

$$\mathcal{O}\left((\hat{a}^\dagger + \hat{a})^4\right) = \sqrt{4!}\,\eta_{04}^+ + 5\sqrt{2!}\,\eta_{02}^+ \tag{3.94}$$

$$\mathcal{D}(\hat{a}^\dagger + \hat{a}) = \sum_{n=1}^\infty \eta_{n,n+1}^+ \tag{3.95}$$

$$\mathcal{D}\left((\hat{a}^\dagger + \hat{a})^4\right) = \sum_{n=1}^\infty\left(A_n^{(4)}\eta_{n,n+4}^+ + A_n^{(2)}\eta_{n,n+2}^+ + A_n^{(0)}\frac{\eta_{n,n}^+}{2}\right), \tag{3.96}$$

with $\eta_{k,l}^\pm = |k\rangle\langle l| \pm |l\rangle\langle k|$, $A_n^{(4)} = \sqrt{(n+4!/n!)}$, $A_n^{(2)} = \sqrt{n^2(n+1)(n+2)} + \sqrt{(n+1)^3(n+2)} + \sqrt{(n+1)(n+2)^3} + \sqrt{(n+1)(n+2)(n+3)^2}$ and $A_n^{(0)} = 6(n^2+n)$. Additionally we calculate some useful commutators

$$\left[\eta_{ij}^+, \eta_{kl}^+\right] = \delta_{jk}\eta_{il}^- + \delta_{jl}\eta_{ik}^- + \delta_{ik}\eta_{jl}^- + \delta_{il}\eta_{jk}^- \tag{3.97}$$

$$\left[\eta_{ij}^-, \eta_{kl}^-\right] = \delta_{jk}\eta_{il}^- - \delta_{jl}\eta_{ik}^- - \delta_{ik}\eta_{jl}^- + \delta_{il}\eta_{jk}^- \tag{3.98}$$

$$\left[\eta_{ij}^-, \eta_{kl}^+\right] = \delta_{jk}\eta_{il}^+ + \delta_{jl}\eta_{ik}^+ - \delta_{ik}\eta_{jl}^+ - \delta_{il}\eta_{jk}^+ \tag{3.99}$$

$$\left[\eta_{ij}^+, \eta_{kl}^-\right] = \delta_{jk}\eta_{il}^+ - \delta_{jl}\eta_{ik}^+ + \delta_{ik}\eta_{jl}^+ - \delta_{il}\eta_{jk}^+. \tag{3.100}$$

With this as a starting point we can calculate the different orders of the SW corrections to the effective Hamiltonian. The zeroth order of the effective Hamiltonian is just the unperturbed part projected into the coupler ground state subspace. The first order corrections are given by the diagonal projections of the perturbation, so in our case only the part $\hat{H}_{\mathrm{int}}^{\mathrm{QB,QB}}$ and the diagonal parts arising from $\hat{H}_{\mathrm{corr}}$, which are

zero because $A_n^0(0) = 0$. Hence a real calculation is first needed for the corrections of order higher than one. When calculated to a specific order the SWT finally gives an effective Hamiltonian acting only on the subspace of interest (here the coupler in ground state subspace), but including corrections coming from states not included in this subspace. The general form of the effective Hamiltonian under the SWT is given in Eq. (3.76). In the following we calculate the different orders of the SWT, up to fourth order analytically.

11.3.1 Second order effective Hamiltonian

First we calculate the first order of the generator S, that defines the SWT and is used to calculate the respective order of the effective Hamiltonian. The first order of S is given by

$$S_1 = \mathcal{L}(V_{\text{od}}), \tag{3.101}$$

where we used the notation of Bravyi et al. [180], such that V_{od} denotes all the off diagonal parts of the perturbation Hamiltonian and the linear map $\mathcal{L}$ is defined as

$$\mathcal{L}(X) = \sum_{i,j} \frac{\langle i|\mathcal{O}(X)|j\rangle}{E_i - E_j} |i\rangle \langle j|, \tag{3.102}$$

where $\{|i\rangle\}$ is an orthonormal eigenbasis of the unperturbed Hamiltonian. With this definition we can write down the expression for S_1

$$S_1 = \sum_{i,j} \frac{\langle i|V_{\text{od}}^{\text{QB,c}}|j\rangle}{E_i - E_j} |i\rangle \langle j| + \sum_{i,j} \frac{\langle i|V_{\text{od}}^{\text{corr}}|j\rangle}{E_i - E_j} |i\rangle \langle j|. \tag{3.103}$$

In our case the $|i\rangle$'s are the eigenstates of the bare coupler Hamiltonian (harmonic oscillator part). We need the following expressions to get S_1:

$$\langle i|\eta_{kl}^+|j\rangle = \delta_{ik}\delta_{jl} + \delta_{il}\delta_{kj} \tag{3.104}$$

$$\Rightarrow \langle i|\eta_{10}^+|j\rangle = \frac{1}{E_1 - E_0}\eta_{10}^- \tag{3.105}$$

$$\Rightarrow \langle i|\eta_{40}^+ + \eta_{20}^+|j\rangle = \frac{1}{E_4 - E_0}\eta_{40}^- + \frac{1}{E_2 - E_0}\eta_{20}^-, \tag{3.106}$$

such that we get

$$S_1 = \sum_{j=1}^{4} \frac{g_j^{\text{QB,c}}\hat{\sigma}_{x,j}}{E_1 - E_0}\eta_{10}^- + K_{\text{corr}}\left(\frac{\sqrt{4!}}{E_4 - E_0} + \frac{5\sqrt{2!}}{E_2 - E_0}\eta_{20}^-\right) \tag{3.107}$$

$$= \sum_{j=1}^{4} \gamma_j^{(1)}\hat{\sigma}_{x,j}\eta_{10}^- + \beta_1^{(1)}\eta_{40}^- + \beta_2^{(1)}, \tag{3.108}$$

where $\gamma_j^{(1)} = g_j^{\text{QB,c}}/(E_1 - E_0)$, $\beta_1^{(1)} = \sqrt{4!}K_{\text{corr}}/(E_4 - E_0)$ and $\beta_2^{(2)} = 6\sqrt{2}K_{\text{corr}}/(E_2 - E_0)$.

The second order of the effective Hamiltonian is then given by

$$H_{\text{eff},2} = b_1 P_0 \hat{S}_1(V_{\text{od}})P_0, \tag{3.109}$$

where we again adopt the notation of Barvyi et al. such that $\hat{S}_1(V_{od}) = [S_1, V_{od}]$. The prefactor b_1 is characterized by the equation

$$b_{2n-1} = \frac{2(2^{2n} - 1)B_{2n}}{(2n)!} \tag{3.110}$$

with Bernoulli numbers B_n. Using the commutation relations (3.97)-(3.100) and the fact that P_0 projects into the coupler ground state subspace - only terms proportional to η_{00} give a contribution - we get

$$\hat{H}_{\text{eff},2} = -\left[\sum_{i,j=1}^{4} \alpha_i^{(1)} g_j^{\text{QB,c}} \hat{Z}_i \hat{Z}_j + \beta_1^{(1)} \beta_1^{(0)} + \beta_2^{(1)} \beta_2^{(0)}\right], \tag{3.111}$$

with $\beta_1^{(0)} = \sqrt{4!}K_{\text{corr}}$ and $\beta_2^{(0)} = 6\sqrt{2}K_{\text{corr}}$.

11.3.2   Third order effective Hamiltonian

The second order of the generator S is given by

$$S_2 = -\mathcal{L}\hat{V}_d(S_1), \tag{3.112}$$

where V_d denotes the diagonal contributions of the perturbation Hamiltonian. In a first step we calculate $[V_d, S_1]$. Again with (3.97)-(3.100) we get

$$
\begin{aligned}
[V_d, S_1] = {} & \sqrt{2}\sum_{i,j=1}^{4} g_i^{\text{QB,c}}\gamma_j^{(1)}\hat{\sigma}_{x,i}\hat{\sigma}_{x,j}\eta_{20}^+ + \sum_{j=1}^{4} g_j^{\text{QB,c}}\beta_1^{(1)}\left(\sqrt{5}\eta_{50}^+ + 2\eta_{30}^+\right) \\
& + \sum_{j=1}^{4} g_j^{\text{QB,c}}\beta_2^{(1)}\hat{\sigma}_{x,j}\left(\sqrt{3}\eta_{30}^+ + \sqrt{2}\eta_{10}^+\right) \\
& + K_{\text{corr}}\left[\sum_{j=1}^{4}\gamma_j^{(1)}A_1^{(4)}\hat{\sigma}_{x,j}\eta_{50}^+ + \beta_1^{(1)}A_2^{(4)}\eta_{60}^+ + \beta_2^{(1)}A_4^{(4)}\eta_{80}^+\right. \\
& \left. + \sum_{j=1}^{4}\gamma_j^{(1)}A_1^{(2)}\eta_{30}^+\beta_1^{(1)}A_2^{(2)}\eta_{40}^+ + \beta_2^{(1)}A_4^{(2)}\eta_{60}^+\beta_2^{(1)}A_2^{(2)}\eta_{20}^+ + \sum_{j=1}^{4}\gamma_j^{(1)}A_1^{(0)}\hat{\sigma}_{x,j}\eta_{10}^+\right. \\
& \left. + \beta_1^{(1)}A_4^{(0)}\eta_{40}^+\beta_2^{(1)}A_2^{(0)}\eta_{20}^+\right]
\end{aligned}
\tag{3.113}
$$

The next order of the effective Hamiltonian is given by $H_{\text{eff},3} = b_1 P_0\hat{S}_2(V_{od})P_0$, so it is again sandwiched by projection operators onto the coupler ground state. S_2 is given by $-\mathcal{L}(V_d(S_1))$. $\mathcal{L}$ maps η_{ij}^+ to η_{ij}^- and adds the respective energy prefactor $1/(E_i - E_j)$. Only terms proportional to η_{00} will not be projected to zero by P_0. Looking at (3.97)-(3.100) we see that only commutators of ηs with identical indices will give a contribution. In V_{od} the only appearing operators of this sort are η_{10}, η_{20} and η_{40}. This means that we can ignore all other η operators in the commutator $\hat{V}_d(S_1)$, since they don't give a contribution to $H_{\text{eff},3}$. Using this simplification, we get

the following expression for the third order effective Hamiltonian

$$
\hat{H}_{\text{eff},3} = \left[\sum_{i,j=1}^{4} \left(\frac{\sqrt{2}\beta_2^{(0)}}{(E_2 - E_0)} \gamma_i^{(1)} g_j^{\text{QB,c}} + \frac{\sqrt{2}\beta_2^{(1)}}{E_1 - E_0} g_i^{\text{QB,c}} g_i^{\text{QB,c}} + \frac{K_{\text{corr}} A_1^{(0)}}{E_1 - E_0} \alpha_i^{(1)} g_j^{\text{QB,c}} \right) \hat{Z}_i \hat{Z}_j \right.
\tag{3.114}
$$

$$
\left. + K_{\text{corr}} \hat{H}_{\text{shift}}^{(3)} \right]
\tag{3.115}
$$

where $H_{\text{shift}}^{(3)}$ adds an overall energy shift to the coupler ground state energy given by

$$
H_{\text{shift}}^{(3)} = \sum_{j=1}^{4} \left(\frac{\beta_1^{(1)} \beta_1^{(0)} A_2^{(2)}}{E_4 - E_0} + \frac{\beta_2^{(1)} \beta_2^{(0)} A_2^{(2)}}{E_2 - E_0} + \frac{\beta_1^{(1)} \beta_1^{(0)} A_4^{(0)}}{E_4 - E_0} + \frac{\beta_2^{(1)} \beta_2^{(0)} A_2^{(0)}}{E_2 - E_0} \right).
\tag{3.116}
$$

Hence the third order effective Hamiltonian has two effects on the qubits. It leads to an overall energy shift given by $H_{\text{shift}}^{(3)}$ and like the second order effective Hamiltonian induces two body local interactions. Therefore we have to calculate the next higher order and see if local interactions $k > 2$ appear.

11.3.3 Fourth order effective Hamiltonian

The third part of the generator is given by

$$
S_3 = -\mathcal{L}\hat{V}_d(S_2) + a_2 \mathcal{L}\hat{S}_1^2(V_{\text{od}}).
\tag{3.117}
$$

with parameters

$$
a_n = \frac{2^n B_n}{n!}
\tag{3.118}
$$

We start with calculating $\hat{V}_d S_2$. In the expression for $H_{\text{eff},4}$ the commutator of S_3 with V_{od} appears. This expression is again sandwiched by P_0 operators. In the same manner as in the last section we therefore only have to include terms of S_3 proportional to η_{10}, η_{40} or η_{20}. This leads to twelve different terms. The effective Hamiltonian is given by

$$
H_{\text{eff},4} = b_1 P_0 \hat{S}_3(V_{\text{od}}) P_0 + b_3 P_0 \hat{S}_1^3(V_{\text{od}}).
\tag{3.119}
$$

We split this Hamiltonian into three different parts

$$
H_{\text{eff},4} = H_{\text{eff},4}^{(1)} + H_{\text{eff},4}^{(2)} + H_{\text{eff},4}^{(3)}
\tag{3.120}
$$

$$
= -b_1 P_0 \left[\mathcal{L}\hat{V}_d(S_2), V_{\text{od}} \right] P_0 + b_1 a_2 P_0 \left[\mathcal{L}\hat{S}_1^2(V\text{od}), V_{\text{od}} \right] + b_3 P_0 \hat{S}_1^3(V_{\text{od}}) P_0
\tag{3.121}
$$

For the first part we get:

$$
\begin{aligned}
H_{\text{eff},4}^{(1)} = -2b_1 K_{\text{corr}} \sum_{i,j=1}^{4} &\left(\frac{5\beta_1^{(1)} g_i^{\text{QB,c}} g_j^{\text{QB,c}}}{(E_5-E_0)(E_4-E_0)} + \frac{\sqrt{5} K_{\text{corr}} A_1^{(4)} \gamma_i^{(1)} g_i^{\text{QB,c}}}{(E_5-E_0)(E_4-E_0)} + \left(\frac{\sqrt{4}}{E_4-E_0} + \frac{\sqrt{3}}{E_3-E_0} \right) \frac{\sqrt{3}\beta_2^{(1)} g_i^{\text{Qb,c}} g_j^{\text{QB,c}}}{E_3-E_0} \right. \\
&+ \frac{K_{\text{corr}} A_1^{(2)} \gamma_i^{(1)} g_j^{\text{QB,c}}}{E_3-E_0} \left(\frac{\sqrt{4}}{E_4-E_0} + \frac{\sqrt{3}}{(E_3-E_0)} \right) + \frac{2\beta_1^{(1)} g_i^{\text{QB,c}} g_j^{\text{QB,c}}}{E_3-E_0} \left(\frac{\sqrt{4}}{E_4-E_0} + \frac{\sqrt{3}}{E_2-E_0} \right) \\
&\left. + \frac{2\beta_2^{(1)} \gamma_i^{1} g_j^{\text{QB,c}}}{(E_2-E_0)^2} + \frac{\sqrt{2} K_{\text{corr}} A_1^{(0)} \gamma_i^{(1)} \gamma_j^{(1)}}{E_2-E_0} + \frac{\sqrt{2} K_{\text{corr}} A_2^{(2)} \gamma_i^{(1)} g_j^{\text{QB,c}}}{(E_2-E_0)(E_4-E_0)} + \frac{\sqrt{2} K_{\text{corr}} A_2^{(0)} \gamma_i^{(1)} g_j^{\text{QB,c}}}{(E_2-E_0)^2} \right) \hat{Z}_i \hat{Z}_j \\
+ \sum_{j=1}^{4} &\left(\frac{\sqrt{2} K_{\text{corr}} \beta_2^{(1)} A_2^{(2)} g_j^{\text{QB,c}}}{(E_2-E_0)(E_1-E_0)} + \frac{\sqrt{2} K_{\text{corr}} \beta_2^{(1)} A_2^{(0)} g_j^{\text{QB,c}}}{(E_2-E_0)(E_1-E_0)} + \frac{\sqrt{5} K_{\text{corr}} \beta_1^{(1)} A_1^{(4)} g_j^{\text{QB,c}}}{(E_5-E_0)(E_1-E_0)} + \frac{K_{\text{corr}} A_1^{4} A_1^{(4)} \gamma_j^{(1)}}{(E_5-E_0)(E_1-E_0)} \right. \\
&+ \frac{2 K_{\text{corr}} \beta_1^{(1)} A_1^{(2)} g_j^{\text{QB,c}}}{(E_3-E_0)(E_2-E_0)} + \frac{\sqrt{3} K_{\text{corr}} \beta_2^{(1)} A_1^{(2)} g_j^{\text{QB,c}}}{(E_3-E_0)(E_1-E_0)} + \frac{K_{\text{corr}} A_1^{(2)} A_1^{(2)} \gamma_j^{(1)}}{(E_3-E_0)(E_1-E_0)} + \frac{\sqrt{2} A_1^{(0)} \beta_2^{(1)} g_j^{\text{QB,c}}}{(E_1-E_0)^2} \\
&\left. + \frac{K_{\text{corr}} A_1^{(0)} A_1^{(0)} \gamma_j^{(1)}}{(E_1-E_0)^2} \right) \hat{Z}_j \\
+ &\frac{K_{\text{corr}}^2 A_2^{(4)} \beta_2^{(1)} A_2^{(4)}}{(E_6-E_0)(E_2-E_0)} + \frac{K_{\text{corr}}^2 \beta_2^{(1)} A_4^{(2)} A_2^{(2)}}{(E_2-E_0)(E_4-E_0)} + \frac{K_{\text{corr}}^2 \beta_2^{(1)} A_2^{(0)} A_2^{(2)}}{(E_2-E_0)(E_4-E_0)} + \frac{K_{\text{corr}}^2 \beta_1^{(1)} A_2^{(2)} A_2^{(2)}}{(E_4-E_0)(E_2-E_0)} \\
+ &\frac{K_{\text{corr}}^2 \beta_1^{(1)} A_4^{(0)} A_2^{(2)}}{(E_4-E_0)(E_2-E_0)} + \frac{K_{\text{corr}}^2 \beta_1^{(1)} A_2^{(4)} A_4^{(2)}}{(E_6-E_0)(E_4-E_0)} + \frac{K_{\text{corr}}^2 \beta_2^{(1)} A_4^{(4)} A_4^{(2)}}{(E_6-E_0)(E_4-E_0)} + \frac{K_{\text{corr}}^2 A_2(0)\beta_2^{(1)} A_2^{(2)}}{(E_2-E_0)^2} \\
+ &\frac{K_{\text{corr}} \beta_2^{(1)} A_2^{(0)} A_2^{(0)}}{(E_2-E_0)^2} + \frac{K_{\text{corr}} \beta_1^{(1)} A_4^{(0)} A_2^{(2)}}{(E_4-E_0)^2} + \frac{K_{\text{corr}} \beta_1^{(1)} A_4^{(0)} A_4^{(0)}}{(E_4-E_0)^2} + \frac{K_{\text{corr}}^2 \beta_1^{(1)} A_2^{(4)} A_2^{(4)}}{(E_6-E_0)(E_2-E_0)} + \frac{K_{\text{corr}}^2 \beta_2^{(1)} A_4^{(4)} A_4^{(4)}}{(E_8-E_0)(E_4-E_0)} \\
+ &\sum_{i,j,k=1}^{4} \frac{2 K_{\text{corr}} \gamma_i^{(1)} g_j^{\text{QB,c}} g_k^{\text{QB,c}}}{(E_2-E_0)(E_1-E_0)} \hat{Z}_i \hat{Z}_j \hat{Z}_k
\end{aligned}
\tag{3.122}
$$

We see that a lot of two local coupling terms arise. Additionally we have single $\hat{Z}$ corrections, an overall energy shift and most important the last term leads to three local qubi-qubit interactions. Let's first calculate the other contributions to the effective Hamiltonian. The second part is given by

$$
\begin{aligned}
H_{\text{eff},4}^{(2)} = 2b_1 a_1 \left[4 \sum_{i,j,k,l=1}^{3} \frac{g_i^{\text{QB,c}} g_j^{\text{QB,c}} g_k^{\text{QB,c}} g_l^{\text{QB,c}}}{(E_1-E_0)^4} \hat{Z}_i \hat{Z}_j \hat{Z}_k \hat{Z}_l + \sum_{i,j=1}^{4} \left(\frac{\gamma_i^{(1)} \gamma_j^{(1)} \beta_1^{(0)} \beta_1^{(0)}}{E_4-E_0} + \frac{\gamma_i^{(1)} \gamma_j^{(1)} \beta_2^{(0)} \beta_2^{(0)}}{E_2-E_0} \right. \right. \\
+ \frac{\beta_1^{(0)} \beta_1^{(1)} \gamma_i^{(1)} g_j^{\text{QB,c}}}{E_4-E_0} + 2\beta_1^{(1)} \beta_1^{(0)} \gamma_i^{(1)} \gamma_j^{(1)} + \frac{\beta_2^{(0)} \beta_2^{(0)} \gamma_i^{(1)} g_j^{\text{QB,c}}}{E_2-E_0} + 2\beta_2^{(1)} \beta_2^{(0)} \gamma_i^{(1)} \gamma_j^{(1)} + \frac{2\beta_2^{(1)} \beta_2^{(0)} \gamma_i^{(1)} g_j^{\text{QB,c}}}{E_2-E_0} \\
\left. + \beta_2^{(1)} \beta_2^{(0)} \beta_2^{(0)} \gamma_i^{(1)} \gamma_j^{(1)} + \beta_2^{(1)} \beta_2^{(1)} \gamma_i^{(1)} g_j^{\text{QB,c}} + \frac{2\beta_1^{(1)} \beta_1^{0} \gamma_i^{(1)} g_j^{\text{QB,c}}}{E_4-E_0} + \beta_1^{(1)} \beta_1^{(1)} \gamma_i^{(1)} g_j^{\text{QB,c}} + \beta_1^{(1)} \beta_1^{(0)} \gamma_i^{(1)} \gamma_j^{(1)} \right) \hat{Z}_i \hat{Z}_j \\
+ \frac{\beta_2^{(1)} \beta_1^{(1)} \beta_2^{(0)} \beta_1^{(0)}}{E_4-E_0} + \frac{2\beta_1^{(1)} \beta_1^{(0)} \beta_2^{(1)} \beta_2^{(0)}}{E_2-E_0} + \frac{4\beta_1^{(1)} \beta_1^{(1)} \beta_1^{(0)} \beta_1^{(0)}}{E_4-E_0} + \frac{\beta_2^{(1)} \beta_2^{(1)} \beta_1^{(0)} \beta_1^{(0)}}{E_4-E_0} + \frac{\beta_1^{(1)} \beta_1^{(1)} \beta_2^{(0)} \beta_2^{(0)}}{E_2-E_0} \\
\left. + \frac{\beta_2^{(1)} \beta_1^{(0)} \beta_1^{1()} \beta_2^{(0)}}{E_2-E_0} + \frac{2\beta_1^{(1)} \beta_2^{(1)} \beta_2^{(0)} \beta_1^{(0)}}{E_4-E_0} \right]
\end{aligned}
\tag{3.123}
$$

and the last part reads

$$
\begin{aligned}
H_{\text{eff},4}^{(3)} = 2b_3 \left[4 \sum_{i,j,k,l=1}^{4} \gamma_i^{(1)} \gamma_j^{(1)} \gamma_k^{(1)} g_l^{\text{QB,c}} \hat{Z}_i \hat{Z}_j \hat{Z}_k \hat{Z}_l + \sum_{i,j=}^{4} \left(\beta_1^{(0)} \beta_1^{(1)} \gamma_i^{(1)} \gamma_j^{(1)} + \beta_2^{(0)} \beta_2^{(1)} \gamma_i^{(1)} \gamma_j^{(1)} \right. \right. \\
+ \beta_1^{(1)} \beta_1^{(1)} \gamma_i^{(1)} g_j^{\text{QB,c}} + 2\beta_1^{(0)} \beta_1^{(0)} \gamma_i^{(1)} \gamma_j^{(1)} + \beta_2^{(1)} \beta_2^{(1)} \gamma_i^{(1)} g_j^{\text{QB,c}} + 2\beta_2^{(0)} \beta_2^{(1)} \gamma_i^{(1)} \gamma_j^{(1)} + 2\beta_2^{(1)} \beta_2^{(1)} \gamma_i^{(1)} g_j^{\text{QB,c}} \\
\left. + \beta_2^{(0)} \beta_2^{(1)} \gamma_i^{(1)} \gamma_j^{(1)} + \beta_2^{(1)} \beta_2^{(1)} \gamma_i^{(1)} g_j^{\text{Qb,c}} \right) \hat{\sigma}_{x,i} \hat{\sigma}_{x,j} + 2\beta_1^{(1)} \beta_1^{(0)} \beta_2^{(1)} \beta_2^{(1)} + \beta_2^{(1)} \beta_1^{(1)} \beta_2^{(0)} \beta_1^{(1)} + \beta_2^{(1)} \beta_2^{(1)} \beta_1^{(0)} \beta_1^{(1)} \\
\left. 4\beta_2^{(1)} \beta_2^{(1)} \beta_2^{(0)} \beta_2^{(1)} + 4\beta_1^{(1)} \beta_1^{(1)} \beta_1^{(0)} \beta_1^{(1)} + \beta_1^{(1)} \beta_1^{(1)} \beta_2^{(0)} \beta_2^{(1)} + \beta_1^{(1)} \beta_2^{(1)} \beta_1^{(0)} \beta_2^{(1)} + 2\beta_1^{(1)} \beta_2^{(0)} \beta_2^{(0)} \beta_1^{(0)} \right].
\end{aligned}
\tag{3.124}
$$

Finally with all these results, the fourth order effective Hamiltonian acting only on the coupler ground state subspace can be written as

$$
H_{\text{eff}} = \hat{P}_0 \hat{H}_0 \hat{P}_0 + \hat{P}_0 \hat{V} \hat{P}_0 + \sum_{n=2}^{4} \hat{H}_{\text{eff},n}.
\tag{3.125}
$$

11.3.4 Coupling Strengths

All in all $H_{\text{eff},4}$ leads to 3 and 4 local qubit-qubit interactions. Anyways, there still are 2 local qubit interactions present and we want the higher ones, to give the leading effect. Therefore it is necessary to go to a regime where the 2 local interactions vanish or at least are smaller than the higher ones. Note that the sum $\sum_{i,j,k,l}$ also gives rise to 2 local interactions (e.g. if $i = j$ and $k = l$), so we have to take them into account.

To summarize the results, we want to give expressions for the different couplings. For simplification we assume that the qubit parameters are the same for all qubits. We define the different coupling strengths such that we can write the effective interaction Hamiltonian as:

$$H_{\text{int,eff}} = J_4 \hat{Z}_1 \hat{Z}_2 \hat{Z}_3 \hat{Z}_4 + J_3 \sum_{i<j<k} \hat{Z}_i \hat{Z}_j \hat{Z}_k + J_2 \sum_{i<k} \hat{Z}_i \hat{Z}_j + J_1 \sum_{i=1}^{4} \hat{Z}_i,$$

where the whole interaction Hamiltonian acts only on the $|0\rangle$ subspace of the coupler. The restriction of the sums comes from the fact that e.g $\hat{Z}_i \hat{Z}_j = \hat{Z}_j \hat{Z}_i$, hence we get an additional prefactor in front of the different coupling terms

$$\sum_{i \neq j \neq k \neq l} \hat{Z}_i \hat{Z}_j \hat{Z}_k \hat{Z}_l + \sum_{i \neq j \neq k} \hat{Z}_i \hat{Z}_j \hat{Z}_k + \sum_{i \neq k} \hat{Z}_i \hat{Z}_j + \sum_{i=1}^{4} \hat{Z}_i \tag{3.126}$$

$$= 4! \hat{Z}_i \hat{Z}_j \hat{Z}_k \hat{Z}_l + 3! \sum_{i<j<k} \hat{Z}_i \hat{Z}_j \hat{Z}_k + 2! \sum_{i<k} \hat{Z}_i \hat{Z}_j + \sum_{i=1}^{4} \hat{Z}_i. \tag{3.127}$$

The four body coupling strength is given by

$$J_4 = 24 \frac{g_{\text{QB,c}}^4}{\Delta_{10}^3}, \tag{3.128}$$

with $\Delta_{ij} = E_i - E_j$. The three body coupling strength is given by

$$J_3 = -\frac{12 K_{\text{corr}} g_{\text{QB,c}}^3}{\Delta_{20} \Delta_{10}^2}. \tag{3.129}$$

The expression for the two body interaction is a little more complicated

$$
\begin{aligned}
J_2/2 = g_{\text{QB,QB}}/2 &- \frac{g_{\text{QB,c}}^2}{\Delta_{10}} + \frac{12 K_{\text{corr}} g_{\text{QB,c}}^2}{\Delta_{20}\Delta_{10}} + \frac{12 K_{\text{corr}} g_{\text{QB,c}}^2}{\Delta_{10}\Delta_{20}} + \frac{12 K_{\text{corr}} g_{\text{QB,c}}^2}{\Delta_{10}^2} - \frac{10\sqrt{6} K_{\text{corr}}^2 g_{\text{QB,c}}^2}{\Delta_{50}\Delta_{40}} \\
&- \frac{10\sqrt{6} K_{\text{corr}}^2 g_{\text{QB,c}}^2}{\Delta_{50}\Delta_{40}\Delta_{10}} - \frac{12\sqrt{6} K_{\text{corr}}^2 g_{\text{QB,c}}^2}{\Delta_{40}\Delta_{30}\Delta_{20}} - \frac{18\sqrt{2} K_{\text{corr}}^2 g_{\text{QB,c}}^2}{\Delta_{30}^2\Delta_{20}} - \frac{20\sqrt{6} K_{\text{corr}}^2 g_{\text{QB,c}}^2}{\Delta_{40}\Delta_{30}\Delta_{10}} - \frac{30\sqrt{2} K_{\text{corr}}^2 g_{\text{QB,c}}^2}{\Delta_{30}^2\Delta_{10}} \\
&- \frac{8\sqrt{6} K_{\text{corr}}^2 g_{\text{QB,c}}^2}{\Delta_{40}\Delta_{20}\Delta_{10}} - \frac{12\sqrt{2} K_{\text{corr}}^2 g_{\text{QB,c}}^2}{\Delta_{20}^3} - \frac{12\sqrt{2} K_{\text{corr}}^2 g_{\text{QB,c}}}{\Delta_{20}\Delta_{10}^2} - \frac{28\sqrt{8} K_{\text{corr}}^2 g_{\text{QB,c}}}{\Delta_{40}\Delta_{20}\Delta_{10}} - \frac{36\sqrt{2} K_{\text{corr}}^2 g_{\text{QB,c}}^2}{\Delta_{20}^2\Delta_{10}} \\
&+ \frac{8 K_{\text{corr}}^2 g_{\text{QB,c}}^2}{\Delta_{40}\Delta_{10}^2} + \frac{24 K_{\text{corr}}^2 g_{\text{QB,c}}^2}{\Delta_{20}^3} + \frac{8 K_{\text{corr}}^2 g_{\text{QB,c}}^2}{\Delta_{40}^2\Delta_{10}} + \frac{16 K_{\text{corr}}^2 g_{\text{QB,c}}^2}{\Delta_{10}^3} + \frac{48 K_{\text{corr}}^2 g_{\text{QB,c}}}{\Delta_{20}^3} + \frac{48 K_{\text{corr}}^2 g_{\text{QB,c}}^2}{\Delta_{20}\Delta_{10}^2} \\
&+ \frac{48 K_{\text{corr}}^2 g_{\text{QB,c}}^2}{\Delta_{20}^2\Delta_{10}} + \frac{144\sqrt{2} K_{\text{corr}}^2 g_{\text{QB,c}}}{\Delta_{10}^2\Delta_{20}} + \frac{24 K_{\text{corr}}^2 g_{\text{QB,c}}^2}{\Delta_{10}\Delta_{20}^2} + \frac{48 K_{\text{corr}}^2 g_{\text{QB,c}}^2}{\Delta_{40}\Delta_{10}\Delta_{20}} + \frac{24 K_{\text{corr}}^2 g_{\text{QB,c}}}{\Delta_{10}\Delta_{20}^2} + \frac{24 K_{\text{corr}}^2 g_{\text{QB,c}}^2}{\Delta_{10}^2\Delta_{20}} \\
&- \frac{2 K_{\text{corr}}^2 g_{\text{QB,c}}^2}{\Delta_{40}\Delta_{10}^2} - \frac{6 K_{\text{corr}}^2 g_{\text{QB,c}}^2}{\Delta_{10}^2\Delta_{20}} - \frac{2 K_{\text{corr}}^2 g_{\text{QB,c}}^2}{\Delta_{10}\Delta_{40}^2} - \frac{4 K_{\text{corr}}^2 g_{\text{QB,c}}^2}{\Delta_{10}^2\Delta_{40}} - \frac{6 K_{\text{corr}}^2 g_{\text{QB,c}}^2}{\Delta_{10}\Delta_{20}^2} - \frac{12 K_{\text{corr}}^2 g_{\text{QB,c}}^2}{\Delta_{10}^2\Delta_{20}} \\
&- \frac{12 K_{\text{corr}}^2 g_{\text{QB,c}}^2}{\Delta_{10}^2\Delta_{20}} - \frac{6 K_{\text{corr}}^2 g_{\text{QB,c}}^2}{\Delta_{10}^2\Delta_{20}} - \frac{6 K_{\text{corr}}^2 g_{\text{QB,c}}^2}{\Delta_{10}\Delta_{20}^2} - \frac{2 K_{\text{corr}}^2 g_{\text{QB,c}}^2}{\Delta_{10}\Delta_{20}^2} + \frac{20 g_{\text{QB,c}}^4}{\Delta_{10}^3}
\end{aligned}
\tag{3.130}
$$

as well as the $\hat{Z}$ corrections

$$J_1 = -\frac{72\sqrt{3}K_{\text{corr}}^3 g_{\text{QB,c}}}{\Delta_{20}^2 \Delta_{10}} - \frac{432 K_{\text{corr}}^3 g_{\text{QB,c}}}{\Delta_{20}^2 \Delta_{10}} - \frac{120\sqrt{3}K_{\text{corr}}^3 g_{\text{QB,c}}}{\Delta_{50}\Delta_{40}\Delta_{10}} - \frac{120 K_{\text{corr}}^3 g_{\text{QB,c}}}{\Delta_{50}\Delta_{10}^2}$$
$$- \frac{240 K_{\text{corr}}^3 g_{\text{QB,c}}}{\Delta_{30}\Delta_{40}\Delta_{10}} - \frac{360 K_{\text{corr}}^3 g_{\text{QB,c}}}{\Delta_{30}\Delta_{20}\Delta_{10}} - \frac{600 K_{\text{corr}}^3 g_{\text{QB,c}}}{\Delta_{30}\Delta_{10}^2} - \frac{144 K_{\text{corr}}^3 g_{\text{QB,c}}}{\Delta_{20}\Delta_{10}^2}$$
$$- \frac{144 K_{\text{corr}}^3 g_{\text{QB,c}}}{\Delta_{10}^3} - 12\frac{K_{\text{corr}} g_{\text{QB,c}}^3}{\Delta_{10}^3}$$
$$\tag{3.131}$$

The bare coupler Hamiltonian is equivalent to a harmonic oscillator, such that the relation $\Delta_{n0} = (n-1)\Delta_{10}$ is satisfied. Therefore we can simplify the expressions for the coupling strengths

$$J_4 = 24\frac{g_{\text{QB,c}}^4}{\Delta_{10}^3} \tag{3.132}$$

$$J_3 = -6\frac{K_{\text{corr}} g_{\text{QB,c}}^3}{\Delta_{10}^3} \tag{3.133}$$

$$J_2 = g_{\text{QB,QB}} - 2\left(1 - \frac{1}{4}\frac{K_{\text{corr}}}{\Delta_{10}} - \underbrace{\frac{1689 + 1060\sqrt{2} - 82\sqrt{6} - 12\sqrt{30}}{24}}_{\approx 122}\frac{K_{\text{corr}}^2}{\Delta_{10}^2}\right)\frac{g_{\text{QB,c}}^2}{\Delta_{10}} \tag{3.134}$$

$$+ 40\frac{g_{\text{QB,c}}^4}{\Delta_{10}^3} \tag{3.135}$$

$$J_1 = -\underbrace{\left(628 + 24\sqrt{3}\right)}_{\approx 670}\frac{K_{\text{corr}}^3 g_{\text{QB,c}}}{\Delta_{10}^3} - 12\frac{K_{\text{corr}} g_{\text{QB,c}}^3}{\Delta_{10}^3} \tag{3.136}$$

Putting in the expressions for K_{corr}, $g_{\text{QB,c}}$ and Δ_{10}, we can write the different couplings in terms of system parameters

$$J_4 = 3E_{\tilde{L}_c}\frac{(\alpha s)^4}{\xi_c(1-\beta_c)^{5/2}} \tag{3.137}$$

$$J_3 = -E_{\tilde{L}_c}\frac{(\alpha s)^3\beta_c\sqrt{\xi_c}}{32(1-\beta_c)^3} \tag{3.138}$$

$$J_2 = E_{\tilde{L}_c}(\alpha s)^2\left(1 - \frac{1}{(1-\beta_c)} + \frac{1}{2}\frac{\beta_c\xi_c}{(1-\beta_c)^{5/2}} + c_1\frac{\beta_c^2\xi_c^2}{(1-\beta_c)^4} + 5\frac{(\alpha s)^2}{\xi_c(1-\beta_c)^{5/2}}\right), \tag{3.139}$$

with $c_1 = \frac{1689+1060\sqrt{2}-82\sqrt{6}-12\sqrt{30}}{55296}$ and where we assumed to have identical qubits, such that $\alpha_i = \alpha_j = \alpha$, $s_i = s_j = s$. Note that all these expressions diverge for $\beta_c \longrightarrow 1$. This is since the prefactors of H_{int} (especially $V_{\text{QB,c}}$) is in the order of 1 in this case, such that the convergence criteria for the SW expansion is no longer satisfied. Anyways we will observe really interesting effect in the regime $\beta_c < 1$. Note that J_1 and J_3 are two to three orders of magnitude smaller than the equal contributions hence they can be ignored (also observed in numerics).

11.4 Numerical Evaluation of the SWT

In the previous section, we presented an analytic solution for the SWT by truncation of the cosine part of the coupler potential. To get more accurate results, it is convenient to include the full coupler potential and solve for the eigenfunctions numerically. We will see that corrections from higher order cosine terms play an important role for larger nonlinearities. To do so, we numerically solve the bare coupler Hamiltonian

$$\hat{H}_c = E_{\tilde{L}_c} \left(\xi_c^2 \frac{q_c^2}{2} + \frac{\hat{\varphi}}{2} + \beta_c \cos(\hat{\varphi}_c) \right). \tag{3.140}$$

This Hamiltonian can be evolved in harmonic oscillator states. For the harmonic part we use the results of the previous section and the cosine part can be written down in this basis using the relation

$$\langle n | e^{ir(\hat{a}^\dagger + \hat{a})} | m \rangle = i^{3n+m} \sqrt{\frac{n!}{m!}} e^{-\frac{r^2}{2}} r^{n-k} L_n^{(n-m)}(r^2), \tag{3.141}$$

where $L_j^{(n-m)}$ refers to the generalized Laguerre polynomial. The cosine part of the potential can now be written in the polar representation and we can write down $\hat{H}_c$ in the harmonic oscillator basis

$$\hat{H}_c = \sum_{n,m=1}^{\infty} \langle n | \hat{H}_c | m \rangle | n \rangle \langle m |. \tag{3.142}$$

Solving for the eigenvectors, we find the unitary transformation $\hat{U}_c$ that diagonalizes $\hat{H}_c$. With $\hat{U}_c$ it is possible, to transform the interaction part of the Hamiltonian into the eigensystem of $\hat{H}_c$ (Note that the coupler parts of the interaction can easily be written down in the harmonic oscillator basis, using (3.141)). This makes it easy to numerically calculate the commutators arising during the SWT by simple matrix multiplications. We truncate the series (3.142) at $n = 50$ oscillator states, since higher truncation limits didn't lead to any notable changes of the results. With this we can calculate the prefactors of (3.127). We see that the results of the analytic and the numerical SWT show the same overall behavior, but the values of both are significantly different. Since the cosine part of the potential gives important contributions to the value of the energy gap, this is what we expect. For increasing β_c the value of ω_c, which denotes the gap in the analytical case decreases rapidly, pushing the calculation over the convergence limit of the SWT. By including the whole potential in the numerical case, the decrease of the gap with increasing β_c is much slower, shifts the convergence breakdown to higher values of β_c. The validity of the SWT will be discussed a little more in the following.

11.5 Comparison Between the Analytical and the Numerical SWT

The difference between the analytical method described in Sec. 11.3 and the numerical SW approach described in Sec. 11.4 is the cosine part of the coupler potential. In the analytical part, we truncate the cosine part after fourth order in $\hat{\varphi}_c$, whereas in the numerical SW approach, we treat the complete cosine part, by calculating the respective coupler eigenfunctions numerically. These parts become especially important for increasing β_c, since this part determines the weight of the cosine part. In Fig. 3.10 we compare the coupling strength given by the analytical and numerical SWT, for the same parameters as in Fig. 2 of the main part. We see that the analyitcal coupling
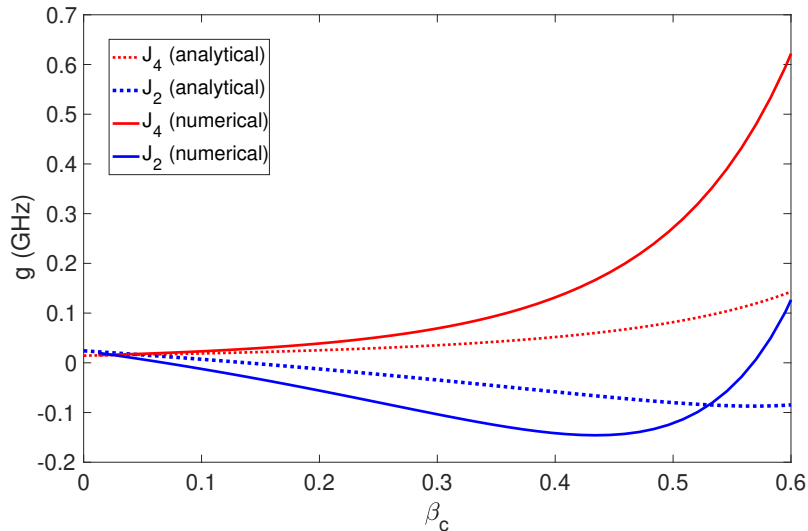
FIGURE 3.10: *Comparison between the coupling strengths for the analytical and the numerical SWT for the same prameters as in Fig. 2 of the main text.*

strengths show the same principle behavior as the numerical SW ones, but the values of J coincide only for very small β_c, whereas for increasing nonlinearities β_c, the numerical SW predicts higher couplings (hence are closer to the complete numerical solution).

11.6   Fully Numerical Results

Since our qubit modeling using (3.74) is not very accurate for qubit nonlinearities only slightly larger than unity, we solve the system numerically and study the resulting spectrum. Here we evolve the bare qubit and coupler Hamiltonian in harmonic oscillator modes using about 50 oscillator states, then project the interaction parts into the low energy subspace and determine the resulting spectrum numerically. The corresponding coupling strengths can be extracted out of the spectrum by the distance of certain energy levels. In more detail we looked at the two-excitation subspace of the spectrum, which is also zoomed in on the right of Fig 2.12. Within this subspace, the distance between the different lines at the point where all frequencies are equal $(\frac{\omega_{1/2}}{\omega_{2/3}} = 1)$ can be calculated analytically. These distances depend on J_2 and J_4, hence it is possible to translate the resulting spectrum into coupling strengths.

The results for a device with realizable qubit and coupler parameters are shown in Fig. 3.11. All the contributions from the indirect coupling term increase with the coupler nonlinearity β_c. We see that for $\beta_c \approx 0$ the two local interactions are dominated by the antiferromagnetic direct coupling part and with increasing nonlinearity get more and more dominated by the ferromagnetic contribution from the indirect part. This results in a change of the nature of the interactions from antiferromagnetic to ferromagnetic at around $\beta_c = 0.2$. The four local interactions on the other hand are antiferromagnetic for all nonlinearities, since they only arise from the indirect coupling. Also we observe that J_2 and J_4 have a crossing point at around $\beta_c = 0.05$. For higher nonlinearites $|J_4|$ is larger than $|J_2|$. Both coupling strenghts increase with increasing β_c, but for the chosen parameters, at β_c around 0.7 the energy levels of the
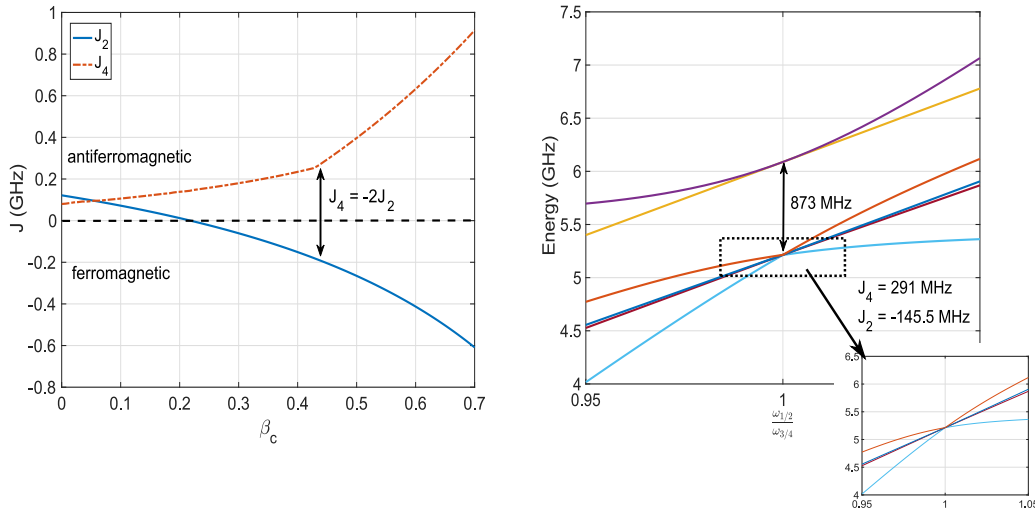
FIGURE 3.11: *Left: Coupling strength depending on the nonlinearity of the coupler for $E_{\tilde{L}_c} = 1$ THz, $\xi_c = 0.01$, $\xi_j = 0.05$, $\alpha_j = 0.05$ and $\beta_j = 1.1$. This corresponds to the physical parameters $L_j = 817$ pH, $C_j = 77$ fF, $L_c = 170$ pH, $C_c = 407$ fF, $I_c^j = 443$ μA, respectively with a mutual inductance of $M = 40$ pH. The corrections arising from the virtual transitions lead to an enhancement of the four local interactions and a discrimination of the two local interactions. For $\beta_c = 0.43$ the results predict antiferromagnetic four local interactions which are twice as large as the ferromagnetic two local interactions. Right: Numerically determined spectrum of the two excitation subspace for $E_j/E_{\tilde{L}_c} = 0.2$. One sees exactly the spectrum theoretically expected at this specific point and the corresponding coupling strengths are $J_4 = 291$ MHz, and $J_2 = -145.5$ MHz for $E_{\text{tildeL}_c} = 1$ THz.*

coupler ground and coupler excited subspace start to mix, such that we can no longer use the setup to mimic the spectrum of the general Ising Hamiltonian including four local interactions. This is the reason why the results in Fig. 3.11 are restricted to $\beta_c < 0.7$ (a more detailed study on this can be found in Sec 11.7). Another remarkable result is, that due to the present virtual transitions, which are not restricted to a nonlinear coupler, there are non-zero four local interactions of about 90 MHz for $\beta_c = 0$.

Note that our parameter choice assumes very high coupler capacitances of about half a pH, but that such values can be realized (e.g. in [156] for a tunable rf-SQUID), and one could also decrease this value accepting smaller coupling strengths. E.g. reducing the coupler capacitance by the factor $1/4$, results in a reduction of the two and four local interactions from 1.6 GHz to 0.6 GHz, when changing only the capacitance.

A well distinguishable point in the spectrum is $J_4 = -2J_2$. In the two excitation subspace of the generalized four qubit Ising Hamiltonian including fourth order interactions, one observes three different energy levels, a non-degenerated, a twice degenerated and a three times degenerated one. At the specific point $J_4 = -2J_2$ this behavior changes and only two different energies are left over, a twice and a four times degenerated. Our results indicate that this point is at $\beta_c = 0.43$ and the numerically calculated spectrum for this specific nonlinearity is shown in Fig 3.11 (right). We see exactly the theoretically expected behavior of the spectrum. For equal qubit

frequencies the spectrum only shows two different energy levels, one twice and one four times degenerate. The distance between these two energy levels is $4J_4$. For the chosen parameters and a realistic $E_{\tilde{L}_c}$ of about 1 THz, we observe a coupling strength of $J_4 = 291$ MHz and $J_2 = -145.5$ MHz. By increasing the nonlinearity β_c the four local interactions can be increased to almost 1 GHz. This is the largest predicted four local interaction strength in a superconducting qubit architecture without ancilla qubits, to the best of our knowledge. The coupling could also be made to be tunable by using a flux qubit architecture with tunable nonlinearity, i.e. a tunable rf-SQUID [156] instead of the rf-SQUID coupler.

Although the analytial results of Sec 11.3 and 11.4 qualitatively give the right behavior of the different coupling strengths, the actual values found by analytics differ from the numerical ones. As mentioned before the reason is the rather small qubit nonlinearity $\beta_j = 1.1$, where the validity of the shifted harmonic oscillator approximation we used to model the qubits is not reliable. Also the larger β_c gets the more important higher orders of the SWT become. E.g. for the specific point $\beta_c = 0.51$ chosen in Fig. 3.11, analytics predict $J_4 = 0.3$ GHz and $J_2 = -0.18$ GHz.

11.7 Discussion of the SWT

As mentioned, there are rather large deviations between the coupling strengths of the effective Hamiltonian obtained by the SWT and the completely numerically determined coupling strengths. The SWT gives the right principle behavior of the coupling, meaning a change of J_2 from antiferromagnetic to ferromagnetic due to the indirect coupling part of the Hamiltonian and a continuous increase of J_4. There are two main problems why the SWT does not quantitatively model the effective system Hamiltonian. The first one is as mentioned above the way we model the qubit. As shown in Sec. 11.B we model the qubit potential with two shifted harmonic potentials. The smaller the qubit nonlinearity β_j the farer away the actual potential is from two shifted harmonic potentials. To get more quantitative results we would have to include higher order corrections to the potential, but then it is no longer possible to get nice analytical results. On the other hand the more we increase the nonlinearity of the coupler β_c, the more higher orders of the SWT matter. This is because the energy distance between the coupler ground and coupler excited subspace decrease with increasing coupler nonlinearity, hence prefactors of e.g. sixth order terms increase. This is the reason for the turnover of the coupling strengths at around $\beta_c = 0.45$ (see Fig. 3.10), which we do not see in the full numerical results of Fig. 3.11. Also for to strong nonlinearities when the two subspaces start to mix, the SWT will diverge when we do not include the coupler excited subspace as well. But as soon as these subspaces start to mix, the system can no longer mimic the spectrum of the Ising spin Hamiltonian including four local interactions, hence we are not interested in this regime. Here with mix we mean that the gap between the two coupler subspaces becomes comparable to the gaps of the spectral lines in the coupler ground state subspace. Then it is likely that interactions between the two subspaces happen. In Fig. 3.12 we compare the gap between the lowest state in the coupler excited and the highest state in the coupler ground subspace and the largest distance between two spectral lines in the coupler ground state subspace depending on the coupler nonlinearity β_c. For consistency reasons we chose the same qubit and coupler parameters as in Fig. 3.11. One sees that for small β_c the gap is much larger than the intersubspace energy differences, but for increasing β_c the gap starts to decrease whereas the intersubspace energy difference increases. In between the region $0.7 < \beta_c < 0.9$ the two values of $\Delta_{\max}$ and Δ_{gap}
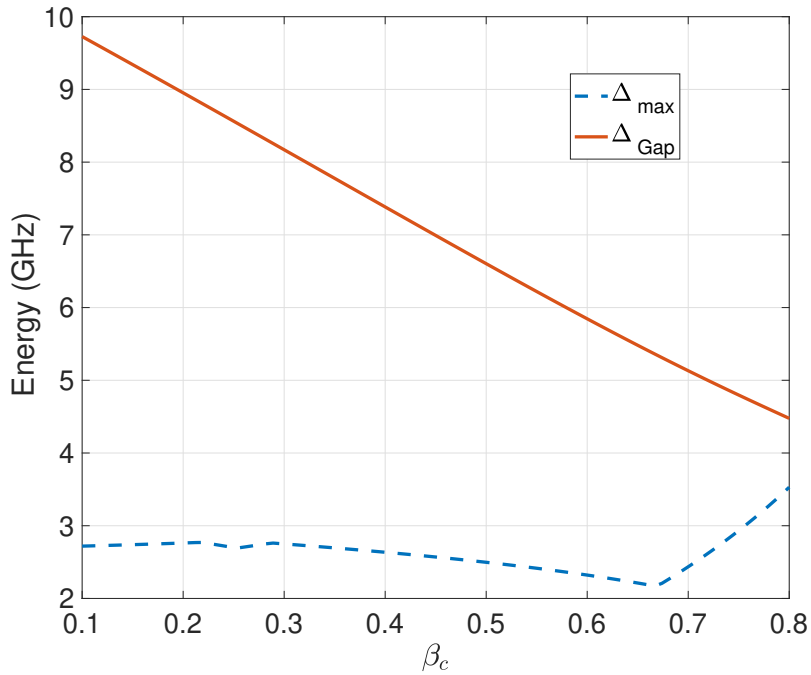
FIGURE 3.12: *Gap between coupler ground and coupler excited sub-space Δ_{Gap} and maximum spectral distance in coupler ground state subspace $\Delta_{\max}$ depending on the coupler nonlinearity β_c.*

become comparable and the two subspaces are no longer well separated. This is the reason why we only show coupling strenghts up to $\beta_c = 0.7$ in Fig. 3.11.

11.8 Susceptibilites to Flux Noise and Fabrication Errors

So far we assumed a perfect coupler with four identical qubits and no external noise. However, in a real experiment there are uncertainties in the system parameters due to fabrication errors as well as external noise sources (especially $1/f$ noise [167]).

11.8.1 Flux noise

Usually the most crucial effect is flux noise. In the Hamiltonian (3.71) and (3.72) flux noise can be described as an additional external flux Φ_{jx} on the qubit and coupler loops, respectively. An external flux on the qubit loops induces a small tilt of the double well potential driving it slightly away from the flux degeneracy point. However, this effect just adds a small $\hat{Z}_j$ contribution on the qubit Hamiltonians. The most important influence of flux noise is the external noise applied to the coupler loop. This can significantly change the respective coupling strength, hence we will focus on this effect. In Fig. 3.13 we show J_2 and J_4 under the influence of a small external current on the coupler loop. We see that small flux variations do not change the four local interaction strength, indicating a magic point for flux noise at $\Phi_{cx} = \Phi_0/2$. Such a point arises when first order corrections of flux fluctuations vanish due to symmetry properties [182] .Only the two local interactions are affected. However, the two local interactions become smaller when we add a small external flux. This brings a huge benefit, since these results indicate that we can apply an external flux to discriminate the two local interactions leading to J_4 of a few hundreds of MHz and J_2 one order
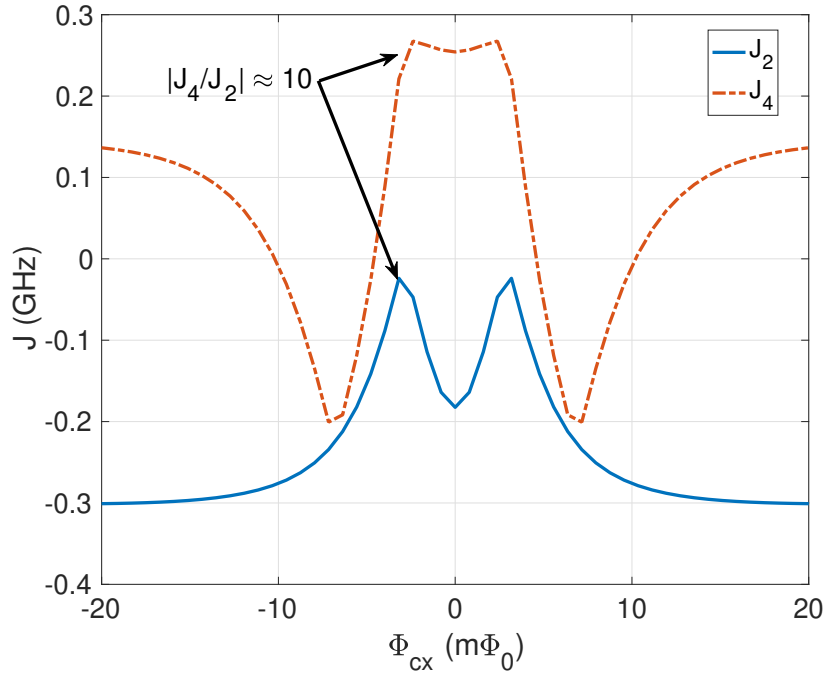
FIGURE 3.13: *Variation of the coupling strengths for a small external flux applied to the coupler loop. System parameters are the same as in Fig. 3.11.*

of magnitude smaller for the chosen parameters. Driving the system slightly away from the degeneracy point also adds $\hat{X}_j$ corrections to the qubit. However, for the chosen parameters the $\hat{Z}_j$ corrections can be estimated from the Hamiltonian to be approximately $10\,\text{GHz/m}\Phi_0$, which results in $J_1 \approx 10\,\text{MHz}$ for the sweet spot shown in Fig. 3.13.

11.8.2 fabrication errors

To study errors in fabrication (e.g. wrong junction parameters), we calculate several susceptibilities that describe the influence of these on the coupling parameters.

For every system parameter that arises in the four and two local interaction strength, we can define a corresponding susceptibility

$$\chi_{4J,j} = \frac{1}{J_4} \sum_{\text{junctions}} \left| \frac{\partial J_4}{\partial P_j} \right|_{J_4=\text{max}} \tag{3.143}$$

$$\chi_{2J,j} = \frac{1}{J_2} \sum_{\text{junctions}} \left| \frac{\partial J_2}{\partial P_j} \right|_{J_2=\text{max}}, \tag{3.144}$$

where the 2 and 4 denote the two and four local interaction strength and P_j represents the system parameter that varies due to fabrication issues. Note that all our analytical results seem to only qualitatively coincide with the numerical found solution. Therefore we will calculate the susceptibilities in this section numerically. The two and four local interaction strengths can be extracted out of the spectrum and then be used to calculate the derivatives appearing in the susceptibilities. Here we assume that the optimal point is the one where the four local interaction strength
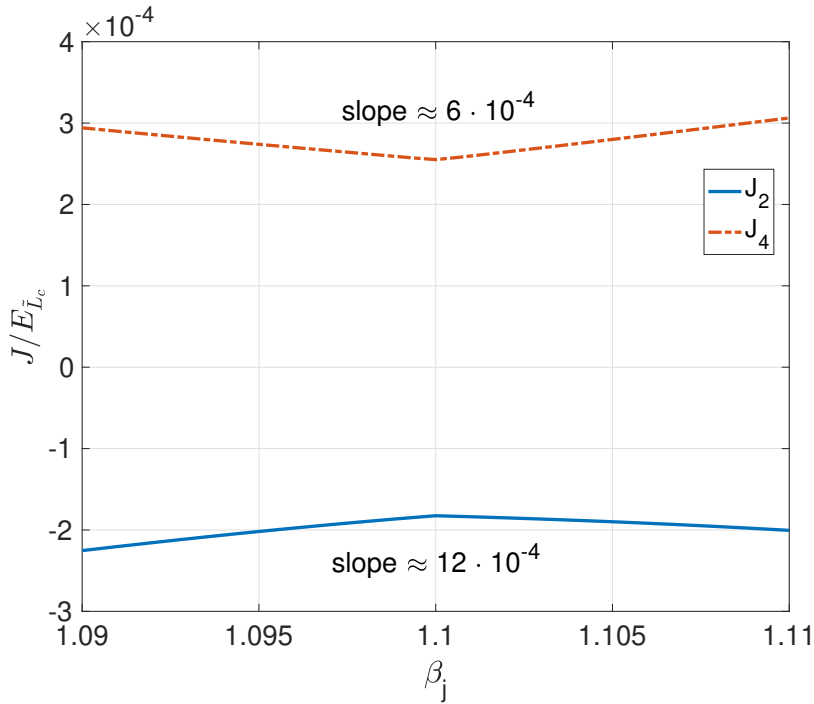
FIGURE 3.14: *Variation of the two and four local interactions for varying nonlinearity of the qubits. The slope can be extracted out of the plots. We choose the same parameters as before, $\chi_c = 0.01$, $\chi_j = 0.05$ and $\beta_c = 0.43$*

is twice the two local one, so we vary the respective parameters around this optimal point.

Error in Josephson energy A typical fabrication error is an impurity in the junctions included in the system. This leads to variations of the Josephson energy. First we study a variation of the Josephson energy of the qubit junctions

$$\chi_{4, E_{J_j}} = \frac{4}{J_4} \left| \frac{\partial J_4}{\partial E_{J_j}} \right| \tag{3.145}$$

$$= \frac{4}{J_4} \left| \frac{\partial J_4}{\partial \beta_j} \right| \left| \frac{\partial \beta_j}{\partial E_{J_j}} \right| \tag{3.146}$$

$$= \frac{4}{J_4} \left| \frac{\partial J_4}{\partial \beta_j} \right| \frac{1}{E_{\tilde{L}_c}}, \tag{3.147}$$

where we used the fact that only β_j changes if we change E_{J_j} and that we assume equal parameters for all four qubits (factor 4). The derivative appearing in the expression can be calculated numerically and $E_{\tilde{L}_c}$ will be a normalization parameter. In Fig. 3.14 we show the variation of the four local and two local interactions for a small variation of E_{J_j}. The susceptibility for the two local interactions $\chi_{J_2, E_{J_j}}$ can be calculated analog to $\chi_{J_4, E_{J_j}}$, but we additionally have to include a factor three which arises from the fact that every qubit can interact with three others. Here we show the variation of the coupling strength with the nonlinearity β_j and using Fig. 3.14 we can extract the derivatives $\frac{\partial J}{\partial E_{J_j}}$ we need to calculate the susceptibilities. This gives the following
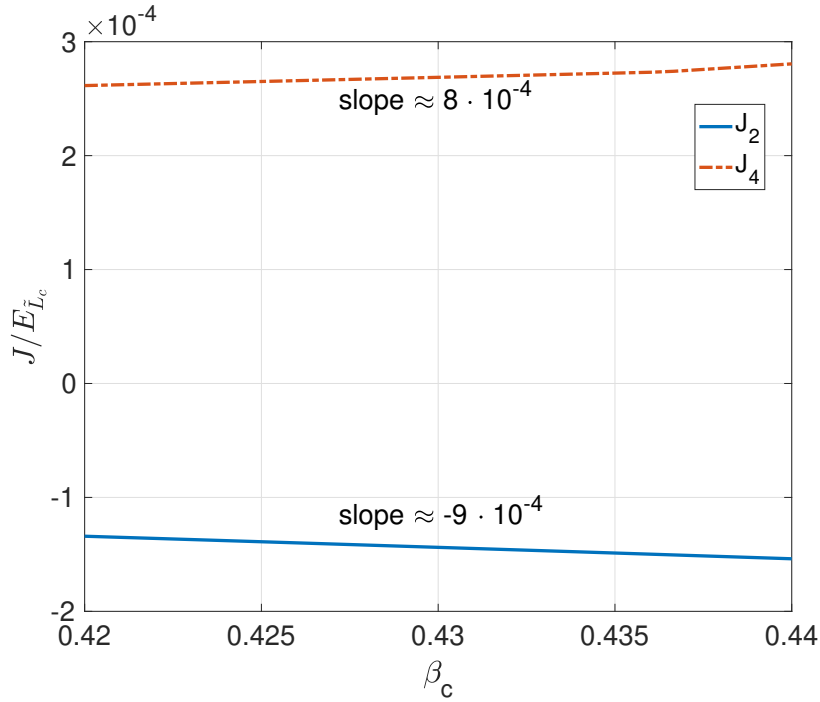
FIGURE 3.15: *Variation of the two and four local interactions for varying nonlinearity of the coupler. The slope can be extracted out of the plots. We choose the same parameters as before, $\chi_c = 0.01$, $\chi_j = 0.05$ and $\beta_c = 0.43$*

values for the used system parameters

$$E_{\tilde{L}_c}\chi_{4J,E_{J_j}} \approx \frac{4}{J_4}6 \cdot 10^{-4} \approx 2.1 \tag{3.148}$$

$$E_{\tilde{L}_c}\chi_{2J,E_{J_j}} \approx \frac{12}{J_2}12 \cdot 10^{-4} \approx 33.1. \tag{3.149}$$

We see that the two local interactions are more affected by variations of the Jospehson energies. However, $E_{\tilde{L}_c}$ is in the THz range for typical system parameters. This means that even for the two local interactions changing E_{J_j} about 1 GHz only results in a change of the order $10^{-2} - 10^{-3}$ GHz of the coupling strength. Typical fabrication errors are assumed to be much smaller than 1 GHz, such that small variations do not crucially affect the two coupling strengths and susceptibilities are rather small.

The same study can be done for a variation of the couplers Josephson energy. The results are shown in Fig. 3.15 and again we can extract the needed derivative from Fig. 3.15 to get an approximate value for the susceptibilities

$$E_{\tilde{L}_c}\chi_{4J,E_{J_c}} \approx \frac{1}{J_4}8 \cdot 10^{-3} \approx 2.7 \tag{3.150}$$

$$E_{\tilde{L}_c}\chi_{2J,E_{J_c}} \approx \frac{1}{J_2}9 \cdot 10^{-3} \approx 6.2. \tag{3.151}$$

As in the previous case for typical values of $E_{\tilde{L}_c}$ these values of the susceptibilities lead to extremely small changes of the coupling strengths when E_{J_c} does not vary too much.
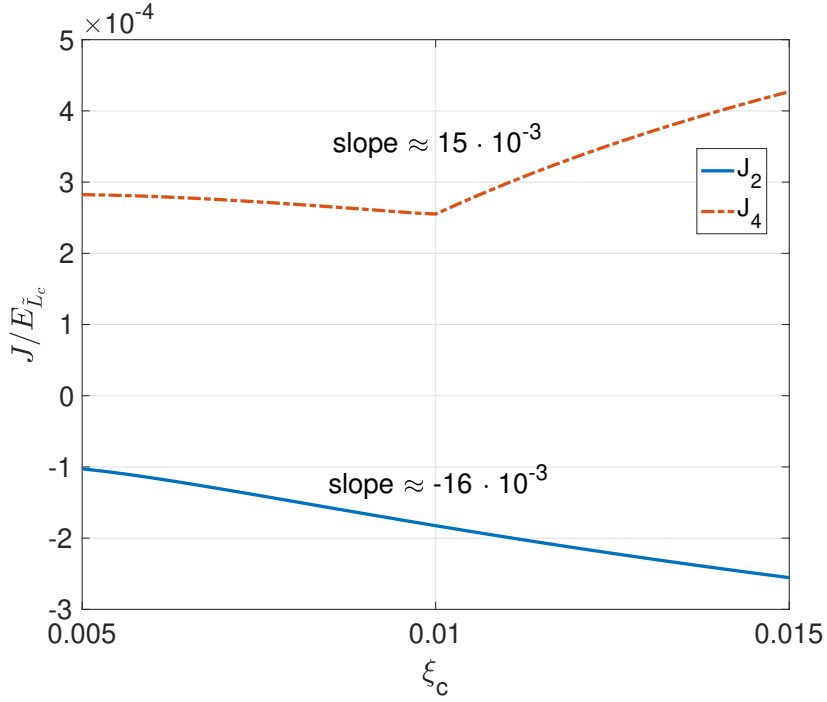
FIGURE 3.16: *Variation of the two and four local interactions for varying ξ_c. The slope can be extracted out of the plots. We choose the same parameters as before, $\chi_c = 0.01$, $\chi_j = 0.05$ and $\beta_c = 0.43$*

Error in inductive Energy Another typical fabrication error is a deviation of inductances between theoretical predicted and actual values in the experiment. In this case it is a little more difficult to calculate the corresponding susceptibilities, since more than one parameter appearing in the coupling strength depend on the impedances of the qubits L_j and the coupler L_c, respectively. First we assume fabrication error in the coupler impedance, which means we have a change in $E_{\tilde{L}_c}$. The susceptibility can be written as

$$\chi_{4J,E_{L_c}} = \frac{1}{J_4} \left(\left| \frac{\partial J_4}{\partial E_{\tilde{L}_c}} \right| \left| \frac{\partial E_{\tilde{L}_c}}{\partial \tilde{L}_c} \right| \left| \frac{\partial \tilde{L}_c}{\partial L_c} \right| + \left| \frac{\partial J_4}{\partial \xi_c} \right| \left| \frac{\xi_c}{\partial \tilde{L}_c} \right| \left| \frac{\partial \tilde{L}_c}{\partial L_c} \right| + \left| \frac{\partial J_4}{\partial \beta_c} \right| \left| \frac{\partial \beta_c}{\partial \tilde{L}_c} \right| \left| \frac{\partial \tilde{L}_c}{\partial L_c} \right| \right) \tag{3.152}$$

$$= \frac{1}{\tilde{L}_c} \left(1 + \chi_c \frac{1}{J_4} \left| \frac{\partial J_4}{\partial \xi_c} \right| + \beta_c \left| \frac{\partial J_4}{\partial \beta_c} \right| \right) \tag{3.153}$$

$$\Rightarrow \tilde{L}_c \chi_{4J,L_c} = 1 + \chi_c \frac{1}{J_4} \left| \frac{\partial J_4}{\partial \xi_c} \right| + \beta_c \left| \frac{\partial J_4}{\partial \beta_c} \right| \tag{3.154}$$

Again we can plot the variation of the coupling strength around the optimal point, to numerically determine the two derivatives appearing in the expression for χ. The susceptibility for the two local interactions is analog, we just have to replace J_4 with J_2. The variation with β_c is already shown in Fig. 3.15 and in Fig. 3.16 we see the variation of the coupling strengths with ξ_c. For the two susceptibilities we get the

approximate values

$$\tilde{L}_c \chi_{4J,L_c} \approx 1.5 \tag{3.155}$$

$$\tilde{L}_c \chi_{2J,L_c} \approx 2.1. \tag{3.156}$$

However, these susceptibilities are given with respect to $\tilde{L}_c$. It is more convenient to look at the susceptibilites with respect to the inductive energies $E_{\tilde{L}_c}$ and E_{L_j}, respectively. We start with the first one to see how a change in $E_{\tilde{L}_c}$ affects the coupling strength. The corresponding susceptibility is just given by (note that we chose units such that $J_i = E_{\tilde{L}_c} \tilde{J}_i$)

$$E_{\tilde{L}_c} \chi_{4J,E_{\tilde{L}_c}} = 1 \tag{3.157}$$

$$E_{\tilde{L}_c} \chi_{2J,E_{\tilde{L}_c}} = 4, \tag{3.158}$$

where again the factor 4 in J_2 arises from the fact that four qubits interact with the coupler. A change in the inductive energy of the qubits leads to a change of β_j, such that

$$\chi_{4J,E_{L_j}} = \frac{4}{J_4} \left(\left| \frac{\partial J_4}{\partial \beta_j} \right| \left| \frac{\partial \beta_j}{\partial E_{L_j}} \right| \right) \tag{3.159}$$

$$= \frac{4}{J_4} \frac{\beta_j}{E_{L_j}} \left| \frac{\partial J_4}{\beta_j} \right|, \tag{3.160}$$

hence we get (using Fig. 3.14)

$$E_{L_j} \chi_{4J,E_{L_j}} \approx 9 \tag{3.161}$$

$$E_{L_j} \chi_{2J,E_{L_j}} \approx 36. \tag{3.162}$$

We see that these two susceptibilities are the most critical ones, since E_{L_j} is one to two orders of magnitude smaller than $E_{\tilde{L}_c}$. Anyways, the fabrication error of inductivities is usually much smaller than the corresponding errors in the junctions and we still need a huge discrepancy here to get a mentionable change of the coupling strengths (since E_{L_j} still is in the order of $10 - 100$ GHz).

To summarize the susceptibility results, we have shown that only huge fabrication errors of the junctions as well as the inductances lead to significant changes of the coupling strengths. Hence our coupler setup is assumed to be robust against fabrication errors.

11.9 Conclusion

In conclusion we have shown that the coupling architecture presented in Fig. 3.9 can exhibit large effective four body local interactions in the deep nonlinear regime. With suitable realistic parameters they are even larger than the two body local interactions and can be in the GHz range. To our knowledge these are the strongest four body local interactions ever predicted in an architecture without additional ancilla qubits. Building such a device could yield a strong improvement of the applicability of AQC. We are also optimistic that this idea can be adapted by other fields, e.g. quantum optics, to build up tools with high four body local interactions using nonlinear couplers.

Appendices

11.A   Derivation of the Circuit Hamiltonian

In this section we show how to get from Kirchhoff's laws to the Hamiltonian (3.170) of the circuit shown in Fig. (1) of the main text using circuit quantization. The section mostly recaps calculations that can be found in [181], but for the sense of completeness we also show them here. In our setup we inductively couple four superconducting flux qubits using a coupling loop, realized by an additional flux qubit with higher plasma frequency as the four qubits. Kirchhoff's laws and Josephson's equations give the current equations of the system

$$C\ddot{\Phi}_c + I_c^{(c)}\sin(2\pi\Phi_c/\Phi_0) - I_{L,c} = 0 \tag{3.163}$$

$$I_j - I_j^* = 0 \qquad (1 \leq j \leq k). \tag{3.164}$$

For the first equation, Φ_c denotes the flux across the coupler's Josephson junction (and capacitor), $I_{L,c}$ denotes the current through the couplers inductor, and $\Phi_0 = h/(2e)$ is the flux quantum. The second equation simply states that the current I_j through j-th inductor is equal to the current I_j^* flowing through the rest of the qubit circuit. We just leave the factors I_j^* like this, since we will see that they do not give a contribution to the interaction part and later lead to the usual flux qubit Hamiltonian [177]. The inductive and flux quantization relationships can be combined into

$$L_c I_{L,c} + \sum_{j=1}^{k} M_j I_j = \Phi_{L,c} \tag{3.165}$$

$$L_j I_j + M_j I_{L,c} = \Phi_j \tag{3.166}$$

$$\Phi_{L,c} = \Phi_{cx} - \Phi_c, \tag{3.167}$$

where Φ_{cx} is the external flux applied to the coupler loop, Φ_j is the flux across the j-th junction, L_j is the j-th qubit self inductance and M_j is the mutual inductance between the jth qubit and the coupler. With equations (3.165)-(3.167) it is possible to rewrite equations (3.163) and (3.164) in flux variables

$$C\ddot{\Phi}_c I_c^{(c)}\sin(2\pi\Phi_c/\phi_0) + \frac{\Phi_c - \Phi_{cx} + \sum_{i=j}^{4}\alpha_i\Phi_j}{\tilde{L}_c} = 0 \tag{3.168}$$

$$\frac{\Phi_j}{L_j} + \alpha_j\left(\Phi_c - \Phi_{cx} + \sum_{k=1}^{4}\alpha_k\Phi_k\right) - I_j^* = 0, \tag{3.169}$$

with dimensionless mutual inductance $\alpha_j = M_j/L_j$ and rescaled coupler impedance $\tilde{L}_c = L_c - \sum_{j=1}^{4}\alpha_j M_j$. These equations of motion represent the Euler-Lagrange equation, resulting from the Lagrange function of the system. Now one can apply circuit quantization to find the corresponding Hamiltonian. From (3.168) and (3.169) we know the Lagrangian, which can be used to define the adjoint variable to the flux and write down a quantized version of the system Hamiltonian using the Legendre transformation. This leads to the Hamiltonian

$$\hat{H} = \frac{\hat{Q}^2}{2C} - E_{J_c}\cos(2\pi\hat{\Phi}_c/\Phi_0) + \frac{\left(\hat{\Phi}_c - \Phi_{cx} + \sum_{j=1}^{k}\alpha_j\hat{\Phi}_j\right)^2}{2\tilde{L}_c} + \sum_{j=1}^{k}\hat{H}_j. \tag{3.170}$$

Here $\hat{H}_j$ denotes the Hamiltonian for qubit j in the absence of the coupler (i.e in the limit $\alpha_j \longrightarrow 0$). Here $\hat{Q}_c$ is the canonical conjugate to $\hat{\Phi}_c$ satisfying $\left[\hat{\Phi}_c, \hat{Q}_c\right] = i\hbar$, and the coupler's Josephson energy is $E_{J_c} = \Phi_0 I_c^{(c)}/2\pi$.

The Hamiltonian can be rewritten in unitless parameters

$$\hat{H} = E_{\tilde{L}_c}\left(4\xi_c^2 \frac{\hat{q}_c^2}{2} + \frac{(\hat{\varphi}_c - \varphi_x)^2}{2} + \beta_c \cos(\hat{\varphi}_c)\right) + \sum_{i=1}^{4} \hat{H}_j \qquad (3.171)$$

$$\hat{H}_j = E_{\tilde{L}_j}\left(4\xi_j^2 \frac{\hat{q}_j^2}{2} + \frac{(\hat{\varphi}_j - \varphi_x)^2}{2} + \beta_j \cos(\hat{\varphi}_j)\right), \qquad (3.172)$$

with the following definitions:

$$E_{\tilde{L}_c} = \frac{(\Phi_0/2\pi)^2}{\tilde{L}_c} \qquad\qquad \zeta_c = \frac{2\pi e}{\Phi_0}\sqrt{\frac{\tilde{L}_c}{C}}$$

$$\beta_c = 2\pi\tilde{L}_c I_c^{(c)}/\Phi_0 = E_{J_c}/E_{\tilde{L}_c} \qquad\qquad \hat{q}_c = \frac{\hat{Q}}{2e}$$

$$\hat{\varphi}_c = \frac{2\pi}{\Phi_0}\hat{\Phi}_c + \pi \qquad\qquad \varphi_{cx} = \frac{2\pi}{\Phi_0}\Phi_{cx} + \pi$$

$$\hat{\varphi}_j = \frac{2\pi}{\Phi_0}\hat{\Phi}_j \qquad\qquad \hat{\varphi}_x = \varphi_{cx} - \sum_{j=1}^{k}\alpha_j\hat{\varphi}_j$$

$$[\hat{\varphi}_c, \hat{q}_j] = i.$$

Note that the phases $\hat{\varphi}$ is shifted by a factor π, such that the flux degeneracy point corresponds to $\varphi_{cx} = 0$.

11.B   Projection into the Qubit Subspace

Since we are interested in qubit interactions, we want to project the qubit part of the Hamiltonian into the subspace of the two lowest eigenstates of every included qubit (computational states). To do so we take a look at the qubit potential

$$\hat{U}_j(\varphi_j) = \frac{1 + \alpha_j^2}{2}\varphi_j^2 + \beta_j \cos(\varphi_j). \qquad (3.173)$$

In case of a flux qubit, the nonlinearity β_j should be larger than one. This leads to a double well potential. The local maximum is located at $\varphi = 0$ and the two symmetric minima at $\varphi = \pm\varphi_p$. Now we approximate the two wells of the potential with two harmonic potentials, shifted by $\pm\varphi_p$ respectively . The equation that determines φ_p reads

$$0 = (1 + \alpha_j)\varphi - \beta_c \sin(\varphi_p), \qquad (3.174)$$

which can easily be solved numerically. To get a harmonic approximation, we evolve the respective potential well around $\pm\varphi_p$ up to second order

$$U^+(\varphi) = c + U'(\varphi_p)(\varphi - \varphi_p) + U''(\varphi_p)(\varphi - \varphi_p)^2 \qquad (3.175)$$

$$U^-(\varphi) = c + U'(-\varphi_p)(\varphi + \varphi_p) + U''(-\varphi_p)(\varphi + \varphi_p)^2. \qquad (3.176)$$

The constant part can be ignored, and the first derivative vanishes, since φ_p satisfies equation (3.174). Hence we get

$$U(\varphi) \approx U^+(\varphi) + U^-(\varphi) \tag{3.177}$$

$$= \frac{1 + \alpha_j - \beta_j \cos(\varphi_p)}{2}(\varphi - \varphi_p)^2 + \frac{1 + \alpha_j - \beta_j \cos(\varphi_p)}{2}(\varphi + \varphi_p)^2. \tag{3.178}$$

To quantize the system we introduce the raising and lowering operator of the two shifted quadratic potentials

$$\hat{a}_\pm^\dagger |N_\pm\rangle = \sqrt{N_\pm + 1} |N_\pm + 1\rangle \tag{3.179}$$

$$\hat{a}_\pm |N_\pm\rangle = \sqrt{N_\pm} |N_\pm - 1\rangle, \tag{3.180}$$

where $|N_\pm\rangle$ are the Fock states of the respective shifted harmonic oscillator. For more details on the displaced harmonic oscillator basis we refer the reader to [168]. We want to restrict the basis to the two lowest energy levels (qubit basis). In the flux basis, which are the superpositions of the ground states $|0_\pm\rangle$ of the two wells

$$|\tilde{0}\rangle = \frac{1}{\sqrt{2}} (|0_+\rangle + |0_-\rangle) \tag{3.181}$$

$$|\tilde{1}\rangle = \frac{1}{\sqrt{2}} (|0_+\rangle - |0_-\rangle). \tag{3.182}$$

Here the two ground states $|0_\pm\rangle$ correspond to the persistent current states of the respective flux qubit. The two states are othorgonal, but since $\langle 0_+|0_-\rangle \neq 0$, we need to redefine an orthonormal qubit basis

$$|0\rangle = \frac{1}{\sqrt{2(1 + \langle 0_+|0_-\rangle)}} (|0_+\rangle + |0_-\rangle) \tag{3.183}$$

$$|1\rangle = \frac{1}{\sqrt{2(1 - \langle 0_+|0_-\rangle)}} (|0_+\rangle - |0_-\rangle). \tag{3.184}$$

Using all the properties we wrote down in this section, we can translate the quantized phase into an operator only acting in the new defined qubit subspace

$$\hat{\varphi}_j \longmapsto \frac{1}{\sqrt{2m_j\omega_j}} \frac{\varphi_p (1 - \langle 0_-|0_+\rangle)}{\sqrt{1 - \langle 0_-|0_+\rangle^2}} \hat{X}_j, \tag{3.185}$$

where the $m_j = 1/4\xi_j^2$ and $\omega_j = 2\xi_j\sqrt{1 + \alpha_j^2 - \beta_c \cos\varphi_p}$ are the effective mass and frequency of the quadratic potential and $\hat{X}_j$ is the Pauli spin operator in the qubit basis. For simplification we additionally define the factor

$$s_j = \frac{1}{\sqrt{2m_j\omega_j}} \frac{\varphi_p (1 - \langle 0_-|0_+\rangle)}{\sqrt{1 - \langle 0_-|0_+\rangle^2}},$$

which also appears in the main text. The overlap between the states in the displaced wells can be calculated by the formula [168]

$$\langle M_-|N_+\rangle = \begin{cases} e^{-\frac{\varphi_p^2}{2}}(-\varphi_p)^{M-N}\sqrt{N!/M!}L_N^{M-N}[\varphi_p^2] & M \geq N \\ e^{-\frac{\varphi_p^2}{2}}(-\varphi_p)^{N-M}\sqrt{M!/N!}L_M^{N-M}[\varphi_p^2] & M < N \end{cases}, \tag{3.186}$$

where L_n^k are the generalized Laguerre polynomials. In the flux qubit literature it is more common to write down the Hamiltonian in the persistent current basis rather than the qubit basis, hence the flux is proportional to $\hat{Z}_j$ instead of $\hat{X}_j$ ($\hat{X}_j \mapsto \hat{Z}_j$) in the following and in the main text.

Conclusion

Since first proposed, the field of quantum computing has progressed rapidly and a real world quantum computer beating classical computers in some specific applications does not seem far away. Circuit model based quantum computers breaking the magic number of 50 qubits with potentially high fidelities are already built, but are not yet running with high fidelity. However, to build a functional universal quantum computer with hundreds or thousands of qubits, not only suitable for specific limited problems, one still needs a lot of improvements within the individual concepts. In this thesis two of the main building blocks of quantum computing where optimized, the measurement of qubits and their interaction. This was achieved by developing new strategies to perform both of these challenges more effectively.

Chapter II of the thesis presents a method to measure the parity of multi-qubit states with high contrast and high fidelity, which is even shown to be potentially quantum non-demolition. This is achieved by coupling multiple qubits to a microwave cavity and driving the cavity into the strongly non-dispersive regime. Here the nonlinearity provided by the qubits causes bifurcations leading to a strong enhancement of the cavity occupation for specific drive strengths. The bifurcation points itself depend on the qubit state, such that, by choosing the right drive frequency, it is shown that different parity states can be distinguished using a microwave photon counter. Contrasts of about 10^5 photons were predicted, exceeding the contrast of typical linear dispersive measurements by several orders of magnitude, making it more suitable for currently available microwave photon counters. In principle the presented protocol can be used for all existing superconducting qubits, but it was especially intended for Transmon based qubits with low anharmonicities.

In Chapter III of the thesis the focus changed from Transmon based to flux based qubits, which are broadly used in the area of adiabatic quantum computing. In Sec. 10 a novel flux qubit measurement scheme is presented, that is able to measure in the persistent current basis at arbitrary bias points, even at the flux degeneracy point. At this point the qubit energy eigenbasis is perpendicular to the persistent current basis. To accomplish that, the flux qubit is coupled to a quantum probe, realizing an indirect measurement with tunable coupling between system and meter. With this strategy and strong coupling it is possible to map the qubit states to pointer states of the quantum probe, and by an additional control, force them into a persistent current direction resolving the qubit state. Such a measurement could yield a variety of applications especially in the area of adiabatic quantum computing, e.g. readout during the anneal and avoid quenches in the annealing schedule, but could also be used for effective quantum state tomography. The quantum non-demolition property of the protocol even extends its possible relevance.

In Sec. 11 the thesis provides a way to overcome the natural limitations to pairwise interactions in most physical systems, by using a nonlinear coupler to control the interaction of four flux qubits. The main idea is to go to a system parameter regime where direct qubit-qubit coupling, leading to the usual pairwise interactions, is rather small and the indirect qubit coupler interaction tends to be the main effect. Within this regime the virtual coupler excitations and deexcitations that result in higher local

interactions are no longer negligible and strong four local interactions are observed in the system. For the right system parameters these four local interactions even exceed the two local ones, making it the leading effect in the system. Such four local interactions are, besides from a fundamental physics point of view, very interesting for the field of adiabatic quantum computing. Here higher order interactions can be used to embed general algorithms on the provided graph structure of the adiabatic quantum computer with much less overhead. Additionally since non-stoquastic interactions are hard to realize in conventional flux qubit realizations, higher local interactions exceeding pairwise also paves the way to a universal adiabatic quantum computer.

All in all quantum computing is evolving more and more from a fundamental physical concept to actual real world applications in fields like quantum chemistry or optimization. Over the last years it was possible to roughly double the number of qubits every year and quantum machines with hundreds of qubits already seems feasible in near future. Building a universal fault tolerant quantum computer on the other hand is a whole other challenge, since there is a huge gap in system size as soon as one needs to include error correction. To achieve such an error corrected quantum computer it needs much further fundamental research to understand the nature of error channels, as well as engineering expertise to scale up and control huge quantum systems.

Bibliography

[1] A. M. Turing, Proceedings of the London mathematical society **2**, 230 (1937).

[2] S. Kilby Kack, in *Nobel Prize* (2010).

[3] G. E. Moore, IEEE Solid-State Circuits Society Newsletter **11**, 33 (2006).

[4] M. M. Waldrop, Nature News **530**, 144 (2016).

[5] R. P. Feynman, International journal of theoretical physics **21**, 467 (1982).

[6] M. A. Nielsen and I. L. Chuang, *Quantum computation and quantum information* (Cambridge university press, 2010).

[7] D. Aharonov, W. van Dam, J. Kempe, Z. Landau, S. Lloyd, and O. Regev, SIAM Review **50**, 755 (2008).

[8] L. K. Grover, arXiv preprint quant-ph/9605043 (1996).

[9] P. Kaye, R. Laflamme, and M. Mosca, *An Introduction to Quantum Computing* (Oxford University press, 2010).

[10] P. Shor, SIAM Review **41**, 303 (1999).

[11] M. Reiher, N. Wiebe, K. M. Svore, D. Wecker, and M. Troyer, Proceedings of the National Academy of Sciences **114**, 7555 (2017).

[12] R. Babbush, C. Gidney, D. W. Berry, N. Wiebe, J. McClean, A. Paler, A. Fowler, and H. Neven, Phys. Rev. X **8**, 041015 (2018).

[13] D. Wecker, B. Bauer, B. K. Clark, M. B. Hastings, and M. Troyer, Phys. Rev. A **90**, 022305 (2014).

[14] V. B. Braginsky and F. Y. Khalili, *Quantum measurement* (Cambridge University Press, 1992).

[15] H. G. Katzgraber, H. Bombin, and M. A. Martin-Delgado, Phys. Rev. Lett. **103**, 090501 (2009).

[16] A. G. Fowler, M. Mariantoni, J. M. Martinis, and A. N. Cleland, Phys. Rev. A **86**, 032324 (2012).

[17] J. M. Chow, J. M. Gambetta, E. Magesan, D. W. Abraham, A. W. Cross, B. Johnson, N. A. Masluk, C. A. Ryan, J. A. Smolin, S. J. Srinivasan, *et al.*, Nature communications **5**, 4015 (2014).

[18] D. Riste, M. Dukalski, C. Watson, G. De Lange, M. Tiggelman, Y. M. Blanter, K. W. Lehnert, R. Schouten, and L. DiCarlo, Nature **502**, 350 (2013).

[19] V. B. Braginsky and F. Y. Khalili, Rev. Mod. Phys. **68**, 1 (1996).

[20] A. Blais, R.-S. Huang, A. Wallraff, S. M. Girvin, and R. J. Schoelkopf, Phys. Rev. A **69**, 062320 (2004).

[21] L. C. G. Govia, E. J. Pritchett, C. Xu, B. L. T. Plourde, M. G. Vavilov, F. K. Wilhelm, and R. McDermott, Phys. Rev. A **90**, 062307 (2014).

[22] D. P. DiVincenzo, Fortschritte der Physik: Progress of Physics **48**, 771 (2000).

[23] F. K. Wilhelm, R. Steinwandt, B. Langenberg, P. J. Liebermann, A. Messinger, and P. K. Schumacher, BSI Project Number 283 (2018).

[24] J. Bardeen, L. N. Cooper, and J. R. Schrieffer, Phys. Rev. **108**, 1175 (1957).

[25] G. Wendin and V. Shumeiko, arXiv preprint cond-mat/0508729 (2005).

[26] J. Clarke and F. K. Wilhelm, Nature **453**, 1031 (2008).

[27] W. D. Oliver and P. B. Welander, MRS bulletin **38**, 816 (2013).

[28] B. D. Josephson, Physics letters **1**, 251 (1962).

[29] J. M. Martinis and K. Osborne, arXiv preprint cond-mat/0402415 (2004).

[30] A. Shnirman, G. Schön, and Z. Hermon, Phys. Rev. Lett. **79**, 2371 (1997).

[31] V. Bouchiat, D. Vion, P. Joyez, D. Esteve, and M. Devoret, Physica Scripta **1998**, 165 (1998).

[32] Y. Nakamura, Y. A. Pashkin, and J. Tsai, nature **398**, 786 (1999).

[33] J. Koch, T. M. Yu, J. Gambetta, A. A. Houck, D. I. Schuster, J. Majer, A. Blais, M. H. Devoret, S. M. Girvin, and R. J. Schoelkopf, Phys. Rev. A **76**, 042319 (2007).

[34] J. Mooij, T. Orlando, L. Levitov, L. Tian, C. H. Van der Wal, and S. Lloyd, Science **285**, 1036 (1999).

[35] C. H. Van Der Wal, A. Ter Haar, F. Wilhelm, R. Schouten, C. Harmans, T. Orlando, S. Lloyd, and J. Mooij, Science **290**, 773 (2000).

[36] I. Chiorescu, Y. Nakamura, C. J. P. M. Harmans, and J. E. Mooij, Science **299**, 1869 (2003).

[37] A. C. J. Ter Haar, *Single and coupled Josephson junction quantum bits*, Ph.D. thesis, TU Delft, Delft University of Technology (2005).

[38] S. Novikov, R. Hinkey, S. Disseler, J. I. Basham, T. Albash, A. Risinger, D. Ferguson, D. A. Lidar, and K. M. Zick, arXiv preprint arXiv:1809.04485 (2018).

[39] S. Haroche and J. Raimond, *Cavity quantum electrodynamics* (US Academic Press, 1994).

[40] H. Walther, B. T. H. Varcoe, B.-G. Englert, and T. Becker, Reports on Progress in Physics **69**, 1325 (2006).

[41] D. I. Schuster, *Circuit quantum electrodynamics* (Yale University, 2007).

[42] T. Niemczyk, F. Deppe, H. Huebl, E. Menzel, F. Hocke, M. Schwarz, J. Garcia-Ripoll, D. Zueco, T. Hümmer, E. Solano, *et al.*, Nature Physics **6**, 772 (2010).

[43] Y. Chen, D. Sank, P. O'Malley, T. White, R. Barends, B. Chiaro, J. Kelly, E. Lucero, M. Mariantoni, A. Megrant, *et al.*, Applied Physics Letters **101**, 182601 (2012).

[44] L. Yu, N. Tong, Z. Xue, Z. Wang, and S. Zhu, Science China Physics, Mechanics and Astronomy **55**, 1557 (2012).

[45] H. Paik, D. I. Schuster, L. S. Bishop, G. Kirchmair, G. Catelani, A. P. Sears, B. R. Johnson, M. J. Reagor, L. Frunzio, L. I. Glazman, S. M. Girvin, M. H. Devoret, and R. J. Schoelkopf, Phys. Rev. Lett. **107**, 240501 (2011).

[46] L. Frunzio, A. Wallraff, D. Schuster, J. Majer, and R. Schoelkopf, IEEE transactions on applied superconductivity **15**, 860 (2005).

[47] M. Göppl, A. Fragner, M. Baur, R. Bianchetti, S. Filipp, J. Fink, P. Leek, G. Puebla, L. Steffen, and A. Wallraff, Journal of Applied Physics **104**, 113904 (2008).

[48] A. Wallraff, D. I. Schuster, A. Blais, L. Frunzio, R.-S. Huang, J. Majer, S. Kumar, S. M. Girvin, and R. J. Schoelkopf, Nature **431**, 162 (2004).

[49] G. Burkard, R. H. Koch, and D. P. DiVincenzo, Phys. Rev. B **69**, 064503 (2004).

[50] J. R. Johansson, G. Johansson, C. M. Wilson, and F. Nori, Phys. Rev. A **82**, 052509 (2010).

[51] M. Fox, *Quantum Optics: An Introdution* (Oxford university press, 2006).

[52] M. Boissonneault, J. M. Gambetta, and A. Blais, Phys. Rev. A **79**, 013819 (2009).

[53] J. Gambetta, W. A. Braff, A. Wallraff, S. M. Girvin, and R. J. Schoelkopf, Phys. Rev. A **76**, 012325 (2007).

[54] L. C. G. Govia, E. J. Pritchett, B. L. T. Plourde, M. G. Vavilov, R. McDermott, and F. K. Wilhelm, Phys. Rev. A **92**, 022335 (2015).

[55] J. Gambetta and I. Sheldon, *Cramming More Power Into a Quantum Device* (IBM Research Blog, 2019).

[56] D. Finke, *Quantum Computing Report* (Stand 06.05.2019).

[57] J. Kelly, in *APS Meeting Abstracts* (2018).

[58] R. Barends, J. Kelly, A. Megrant, D. Sank, E. Jeffrey, Y. Chen, Y. Yin, B. Chiaro, J. Mutus, C. Neill, P. O'Malley, P. Roushan, J. Wenner, T. C. White, A. N. Cleland, and J. M. Martinis, Phys. Rev. Lett. **111**, 080502 (2013).

[59] J. Kelly, R. Barends, A. G. Fowler, A. Megrant, E. Jeffrey, T. C. White, D. Sank, J. Y. Mutus, B. Campbell, Y. Chen, *et al.*, Nature **519**, 66 (2015).

[60] P. V. Klimov, J. Kelly, Z. Chen, M. Neeley, A. Megrant, B. Burkett, R. Barends, K. Arya, B. Chiaro, Y. Chen, A. Dunsworth, A. Fowler, B. Foxen, C. Gidney, M. Giustina, R. Graff, T. Huang, E. Jeffrey, E. Lucero, J. Y. Mutus, O. Naaman, C. Neill, C. Quintana, P. Roushan, D. Sank, A. Vainsencher, J. Wenner, T. C. White, S. Boixo, R. Babbush, V. N. Smelyanskiy, H. Neven, and J. M. Martinis, Phys. Rev. Lett. **121**, 090502 (2018).

[61] M. John, *The Quantum Space Race* (2018).

[62] J. Kelly, Z. Chen, B. Chiaro, B. Foxen, and J. M. Martinis, in *APS Meeting Abstracts* (2019).

[63] Z. Chen, J. Kelly, B. Chiaro, B. Foxen, and J. M. Martinis, in *APS Meeting Abstracts* (2019).

[64] S. Boixo, S. V. Isakov, V. N. Smelyanskiy, R. Babbush, N. Ding, Z. Jiang, M. J. Bremner, J. M. Martinis, and H. Neven, Nature Physics **14**, 595 (2018).

[65] E. Pednault, J. A. Gunnels, G. Nannicini, L. Horesh, T. Magerlein, E. Solomonik, and R. Wisnieff, arXiv preprint arXiv:1710.05867 (2017).

[66] J. Preskill, Quantum **2**, 79 (2018).

[67] A. W. Harrow and A. Montanaro, Nature **549**, 203 (2017).

[68] H.-P. Breuer and F. Petruccione, *The Theory of Open Quantum Systems* (Oxford University Press, 2010).

[69] L. C. G. Govia, E. J. Pritchett, S. T. Merkel, D. Pineau, and F. K. Wilhelm, Phys. Rev. A **86**, 032311 (2012).

[70] M. Schöndorf, L. C. G. Govia, M. G. Vavilov, R. McDermott, and F. K. Wilhelm, Quantum Science and Technology **3**, 024009 (2018).

[71] Y.-F. Chen, D. Hover, S. Sendelbach, L. Maurer, S. T. Merkel, E. J. Pritchett, F. K. Wilhelm, and R. McDermott, Phys. Rev. Lett. **107**, 217401 (2011).

[72] A. Opremcak, I. V. Pechenezhskiy, C. Howington, B. G. Christensen, M. A. Beck, E. Leonard, J. Suttle, C. Wilen, K. N. Nesterov, G. J. Ribeill, T. Thorbeck, F. Schlenker, M. G. Vavilov, B. L. T. Plourde, and R. McDermott, Science **361**, 1239 (2018).

[73] A. Blais, J. Gambetta, A. Wallraff, D. I. Schuster, S. M. Girvin, M. H. Devoret, and R. J. Schoelkopf, Phys. Rev. A **75**, 032329 (2007).

[74] J. M. Chow, J. M. Gambetta, A. D. Córcoles, S. T. Merkel, J. A. Smolin, C. Rigetti, S. Poletto, G. A. Keefe, M. B. Rothwell, J. R. Rozen, M. B. Ketchen, and M. Steffen, Phys. Rev. Lett. **109**, 060501 (2012).

[75] J. You and F. Nori, Nature **474**, 589 (2011).

[76] T. Brecht, W. Pfaff, C. Wang, Y. Chu, L. Frunzio, M. H. Devoret, and R. J. Schoelkopf, npj Quantum Information **2**, 16002 (2016).

[77] M. Hofheinz, H. Wang, M. Ansmann, R. C. Bialczak, E. Lucero, M. Neeley, A. O'connell, D. Sank, J. Wenner, J. M. Martinis, *et al.*, Nature **459**, 546 (2009).

[78] D. A. Lidar and T. A. Brun, *Quantum error correction* (Cambridge University Press, 2013).

[79] D. S. Wang, A. G. Fowler, and L. C. L. Hollenberg, Phys. Rev. A **83**, 020302 (2011).

[80] D. Ristè, S. Poletto, M.-Z. Huang, A. Bruno, V. Vesterinen, O.-P. Saira, and L. DiCarlo, Nature communications **6**, 6983 (2015).

[81] J. Joo, Y.-J. Park, S. Oh, and J. Kim, New Journal of Physics **5**, 136 (2003).

[82] S.-Y. Huang, H.-S. Goan, X.-Q. Li, and G. J. Milburn, Phys. Rev. A **88**, 062311 (2013).

[83] S. Shankar, M. Hatridge, Z. Leghtas, K. Sliwa, A. Narla, U. Vool, S. M. Girvin, L. Frunzio, M. Mirrahimi, and M. H. Devoret, Nature **504**, 419 (2013).

[84] F. Armata, G. Calajo, T. Jaako, M. S. Kim, and P. Rabl, Phys. Rev. Lett. **119**, 183602 (2017).

[85] C. Eichler, D. Bozyigit, and A. Wallraff, Phys. Rev. A **86**, 032106 (2012).

[86] R. Vijay, C. Macklin, D. H. Slichter, S. J. Weber, K. Murch, R. Naik, A. N. Korotkov, and I. Siddiqi, Nature **490**, 77 (2012).

[87] J. Majer, J. Chow, J. Gambetta, J. Koch, B. Johnson, J. Schreier, L. Frunzio, D. Schuster, A. Houck, A. Wallraff, *et al.*, Nature **449**, 443 (2007).

[88] R. Vijay, D. H. Slichter, and I. Siddiqi, Phys. Rev. Lett. **106**, 110502 (2011).

[89] D. M. Pozar, *Microwave Engineering* (Wiley, New Jersey, 2012).

[90] V. Peano and M. Thorwart, EPL (Europhysics Letters) **89**, 17008 (2010).

[91] M. Boissonneault, J. M. Gambetta, and A. Blais, Phys. Rev. Lett. **105**, 100504 (2010).

[92] L. S. Bishop, E. Ginossar, and S. M. Girvin, Phys. Rev. Lett. **105**, 100505 (2010).

[93] P. Carbonaro, G. Compagno, and F. Persico, Physics Letters A **73**, 97 (1979).

[94] P. Bertet, F. Ong, M. Boissonneault, A. Bolduc, F. Mallet, A. Doherty, A. Blais, D. Vion, and D. Esteve, *Circuit quantum electrodynamics with a nonlinear resonator* (Oxford University Press, 2012).

[95] D. P. DiVincenzo, Physica Scripta **2009**, 014020 (2009).

[96] E. T. Jaynes and F. W. Cummings, Proceedings of the IEEE **51**, 89 (1963).

[97] D. Walls and G. J. Milburn, *Quantum Optics* (Springer, Heidelberg, 2008).

[98] N. J. Vilenkin and A. Klimyk, *Representation of Lie groups and special functions: recent advances* (2013).

[99] M. I. Dykman, *Fluctuating nonlinear oscillators* (Oxford University Press on Demand, 2012).

[100] P. Drummond and D. Walls, Journal of Physics A: Mathematical and General **13**, 725 (1980).

[101] F. Mallet, F. R. Ong, A. Palacios-Laloy, F. Nguyen, P. Bertet, D. Vion, and D. Esteve, Nature Physics **5**, 791 (2009).

[102] M. Boissonneault, J. M. Gambetta, and A. Blais, Phys. Rev. A **77**, 060305 (2008).

[103] J. Gambetta, A. Blais, M. Boissonneault, A. A. Houck, D. I. Schuster, and S. M. Girvin, Phys. Rev. A **77**, 012112 (2008).

[104] M. Boissonneault, A. C. Doherty, F. R. Ong, P. Bertet, D. Vion, D. Esteve, and A. Blais, Phys. Rev. A **85**, 022305 (2012).

[105] J. Gambetta, A. Blais, D. I. Schuster, A. Wallraff, L. Frunzio, J. Majer, M. H. Devoret, S. M. Girvin, and R. J. Schoelkopf, Phys. Rev. A **74**, 042318 (2006).

[106] C. W. Gardiner and P. Zoller, *Quantum Noise* (Springer Complexity, Heidelberg, 2004).

[107] D. Aharonov, W. Van Dam, J. Kempe, Z. Lamda, S. Lloyd, and O. Regev, in Proceedings of the 45th IEEE Symposium on Foundations of Computer Science, Rome, Italy , 42 (2004).

[108] T. Albash and D. A. Lidar, Rev. Mod. Phys. **90**, 015002 (2018).

[109] M. Born and R. Oppenheimer, Annalen der Physik **389**, 457 (1927).

[110] T. Kato, Journal of the Physical Society of Japan **5**, 435 (1950).

[111] K.-P. Marzlin and B. C. Sanders, Phys. Rev. Lett. **93**, 160408 (2004).

[112] M. Amin, Physical review letters **102**, 220401 (2009).

[113] A. Ambainis and O. Regev, arXiv preprint quant-ph/0411152 (2004).

[114] G. Nenciu, Communications in mathematical physics **152**, 479 (1993).

[115] J. E. Avron and A. Elgart, Communications in mathematical physics **203**, 445 (1999).

[116] D. Cheung, P. Høyer, and N. Wiebe, Journal of Physics A: Mathematical and Theoretical **44**, 415302 (2011).

[117] A. Elgart and G. A. Hagedorn, Journal of Mathematical Physics **53**, 102202 (2012).

[118] G. A. Hagedorn and A. Joye, Journal of mathematical analysis and applications **267**, 235 (2002).

[119] V. S. Denchev, S. Boixo, S. V. Isakov, N. Ding, R. Babbush, V. Smelyanskiy, J. Martinis, and H. Neven, Phys. Rev. X **6**, 031015 (2016).

[120] L. Theis, P. K. Schuhmacher, M. Marthaler, and F. Wilhelm, arXiv preprint arXiv:1808.09873 (2018).

[121] N. Chancellor, New Journal of Physics **19**, 023024 (2017).

[122] D.-W. S. Inc., D-Wave whitepaper (2017).

[123] M. Ohkuwa, H. Nishimori, and D. A. Lidar, Phys. Rev. A **98**, 022314 (2018).

[124] R. Harris, Y. Sato, A. J. Berkley, M. Reis, F. Altomare, M. H. Amin, K. Boothby, P. Bunyk, C. Deng, C. Enderud, S. Huang, E. Hoskinson, M. W. Johnson, E. Ladizinsky, N. Ladizinsky, T. Lanting, R. Li, T. Medina, R. Molavi, R. Neufeld, T. Oh, I. Pavlov, I. Perminov, G. Poulin-Lamarre, C. Rich, A. Smirnov, L. Swenson, N. Tsai, M. Volkmann, J. Whittaker, and J. Yao, Science **361**, 162 (2018).

[125] A. D. King, J. Carrasquilla, J. Raymond, I. Ozfidan, E. Andriyash, A. Berkley, M. Reis, T. Lanting, R. Harris, F. Altomare, *et al.*, Nature **560**, 456 (2018).

[126] D. Venturelli and A. Kondratyev, arXiv preprint arXiv:1810.08584 (2018).

[127] E. Ising, Zeitschrift für Physik **31**, 253 (1925).

[128] S. Istrail, in *Proceedings of the thirty-second annual ACM symposium on Theory of computing* (ACM, 2000) pp. 87–96.

[129] L. Hormozi, E. W. Brown, G. Carleo, and M. Troyer, Phys. Rev. B **95**, 184416 (2017).

[130] H. Nishimori and K. Takada, Frontiers in ICT **4**, 2 (2017).

[131] W. Vinci and D. A. Lidar, npj Quantum Information **3**, 38 (2017).

[132] I. Ozfidan, C. Deng, A. Smirnov, T. Lanting, R. Harris, L. Swenson, J. Whittaker, F. Altomare, M. Babcock, C. Baron, *et al.*, arXiv preprint arXiv:1903.06139 (2019).

[133] A. J. Kerman, arXiv preprint arXiv:1810.01352 (2018).

[134] S. B. Bravyi and A. Y. Kitaev, arXiv preprint quant-ph/9811052 (1998).

[135] R. Ruskov and A. N. Korotkov, Phys. Rev. B **67**, 241305 (2003).

[136] R. Raussendorf and H. J. Briegel, Phys. Rev. Lett. **86**, 5188 (2001).

[137] A. Lupaşcu, C. J. M. Verwijs, R. N. Schouten, C. J. P. M. Harmans, and J. E. Mooij, Phys. Rev. Lett. **93**, 177006 (2004).

[138] A. Lupaşcu, C. J. P. M. Harmans, and J. E. Mooij, Phys. Rev. B **71**, 184506 (2005).

[139] A. Lupaşcu, E. F. C. Driessen, L. Roschier, C. J. P. M. Harmans, and J. E. Mooij, Phys. Rev. Lett. **96**, 127003 (2006).

[140] A. Lupaşcu, S. Saito, T. Picot, P. De Groot, C. Harmans, and J. Mooij, nature physics **3**, 119 (2007).

[141] N. Boulant, G. Ithier, P. Meeson, F. Nguyen, D. Vion, D. Esteve, I. Siddiqi, R. Vijay, C. Rigetti, F. Pierre, and M. Devoret, Phys. Rev. B **76**, 014525 (2007).

[142] D. Ristè, C. C. Bultink, K. W. Lehnert, and L. DiCarlo, Phys. Rev. Lett. **109**, 240502 (2012).

[143] M. Schöndorf and F. K. Wilhelm, Phys. Rev. A **97**, 043849 (2018).

[144] E. Farhi, J. Goldstone, S. Gutmann, J. Lapan, A. Lundgren, and D. Preda, Science **292**, 472 (2001).

[145] S. Jansen, M.-B. Ruskai, and R. Seiler, Journal of Mathematical Physics **48**, 102111 (2007).

[146] S. Bravyi, D. P. DiVincenzo, D. Loss, and B. M. Terhal, Phys. Rev. Lett. **101**, 070503 (2008).

[147] J.-L. Orgiazzi, C. Deng, D. Layden, R. Marchildon, F. Kitapli, F. Shen, M. Bal, F. Ong, and A. Lupascu, Physical Review B **93**, 104518 (2016).

[148] K. Inomata, T. Yamamoto, P.-M. Billangeon, Y. Nakamura, and J. Tsai, Physical Review B **86**, 140508 (2012).

[149] R. Rifkin and B. S. Deaver, Phys. Rev. B **13**, 3894 (1976).

[150] Y. S. Greenberg, A. Izmalkov, M. Grajcar, E. Il'ichev, W. Krech, H.-G. Meyer, M. H. S. Amin, and A. M. van den Brink, Phys. Rev. B **66**, 214525 (2002).

[151] Y.-D. Wang, X. Zhu, and C. Bruder, Phys. Rev. B **83**, 134504 (2011).

[152] A. I. Lvovsky and M. G. Raymer, Rev. Mod. Phys. **81**, 299 (2009).

[153] S. Filipp, P. Maurer, P. J. Leek, M. Baur, R. Bianchetti, J. M. Fink, M. Göppl, L. Steffen, J. M. Gambetta, A. Blais, and A. Wallraff, Phys. Rev. Lett. **102**, 200402 (2009).

[154] R. Harris, T. Lanting, A. J. Berkley, J. Johansson, M. W. Johnson, P. Bunyk, E. Ladizinsky, N. Ladizinsky, T. Oh, and S. Han, Phys. Rev. B **80**, 052506 (2009).

[155] S. Poletto, F. Chiarello, M. Castellano, J. Lisenfeld, A. Lukashenko, P. Carelli, and A. Ustinov, Physica Scripta **2009**, 014011 (2009).

[156] M. Castellano, F. Chiarello, P. Carelli, C. Cosmelli, F. Mattioli, and G. Torrioli, New Journal of Physics **12**, 043047 (2010).

[157] A. J. Berkley, M. W. Johnson, P. Bunyk, R. Harris, J. Johansson, T. Lanting, E. Ladizinsky, E. Tolkacheva, M. H. S. Amin, and G. Rose, Superconductor Science and Technology **23**, 105014 (2010).

[158] J. Whittaker, L. Swenson, M. Volkmann, P. Spear, F. Altomare, A. Berkley, B. Bumble, P. Bunyk, P. Day, B. Eom, *et al.*, Journal of Applied Physics **119**, 014506 (2016).

[159] A. Y. Smirnov and M. H. Amin, Low Temperature Physics **43**, 772 (2017).

[160] T. Picot, R. Schouten, C. Harmans, and J. Mooij, Physical review letters **105**, 040506 (2010).

[161] T. Picot, *On the Quantum Measurement of Superconducting Flux Qubits*, Ph.D. thesis, Delft University of Technology (2010).

[162] F. K. Wilhelm, Phys. Rev. B **68**, 060503 (2003).

[163] A. A. Clerk, S. M. Girvin, and A. D. Stone, Phys. Rev. B **67**, 165324 (2003).

[164] A. Baust, E. Hoffmann, M. Haeberlein, M. J. Schwarz, P. Eder, J. Goetz, F. Wulschner, E. Xie, L. Zhong, F. Quijandría, D. Zueco, J.-J. G. Ripoll, L. García-Álvarez, G. Romero, E. Solano, K. G. Fedorov, E. P. Menzel, F. Deppe, A. Marx, and R. Gross, Phys. Rev. B **93**, 214501 (2016).

[165] P. Forn-Díaz, J. J. García-Ripoll, B. Peropadre, J.-L. Orgiazzi, M. Yurtalan, R. Belyansky, C. M. Wilson, and A. Lupascu, Nature Physics **13**, 39 (2017).

[166] M. B. Weissman, Rev. Mod. Phys. **60**, 537 (1988).

[167] F. Yoshihara, K. Harrabi, A. O. Niskanen, Y. Nakamura, and J. S. Tsai, Phys. Rev. Lett. **97**, 167001 (2006).

[168] E. K. Irish, J. Gea-Banacloche, I. Martin, and K. C. Schwab, Phys. Rev. B **72**, 195410 (2005).

[169] E. Farhi, J. Goldstone, S. Gutmann, and M. Sipser, arXiv preprint quant-ph/0001106 (2000).

[170] W. Van Dam, M. Mosca, and U. Vazirani, in *Proceedings 2001 IEEE International Conference on Cluster Computing* (IEEE, 2001) pp. 279–287.

[171] N. S. Dattani and N. Bryans, arXiv preprint arXiv:1411.6758 (2014).

[172] V. Efimov, Sov. J. Nucl. Phys **12**, 101 (1971).

[173] T. Kraemer, M. Mark, P. Waldburger, J. Danzl, C. Chin, B. Engeser, A. Lange, K. Pilch, A. Jaakkola, H.-C. Nägerl, *et al.*, Nature **440**, 315 (2006).

[174] S. P. Jordan and E. Farhi, Phys. Rev. A **77**, 062329 (2008).

[175] N. Chancellor, S. Zohren, and P. A. Warburton, npj Quantum Information **3**, 21 (2017).

[176] M. Leib, P. Zoller, and W. Lechner, Quantum Science and Technology **1**, 015008 (2016).

[177] M. H. Devoret *et al.*, Les Houches, Session LXIII **7** (1995).

[178] P.-Q. Jin, M. Marthaler, A. Shnirman, and G. Schön, Phys. Rev. Lett. **108**, 190506 (2012).

[179] J. R. Schrieffer and P. A. Wolff, Phys. Rev. **149**, 491 (1966).

[180] S. Bravyi, D. P. DiVincenzo, and D. Loss, Annals of physics **326**, 2793 (2011).

[181] D. Kafri, C. Quintana, Y. Chen, A. Shabani, J. M. Martinis, and H. Neven, Phys. Rev. A **95**, 052333 (2017).

[182] M. H. S. Amin, Phys. Rev. B **71**, 024504 (2005).